Computational Investigations of Flow and Heat Transfer in Gas-Liquid Slug Flow in Millimeter-Size Channels

Sadhana Kumari

TH-2207_146107023

Computational Investigations of Flow and Heat Transfer in Gas-Liquid Slug Flow in Millimeter-Size Channels

Thesis submitted in partial fulfillment of the requirement for the degree of

Doctor of Philosophy

By

Sadhana Kumari

Roll No.: 146107023

Department of Chemical Engineering

Indian Institute of Technology Guwahati, Assam 781039

May 2019

TH-2207_146107023

Dedicated to my Family and the Almighty. Their Uncountable Blessings and Support has Helped Me to be the Better Person that I am Today.

TH-2207_146107023

Department of Chemical Engineering

Indian Institute of Technology Guwahati

Guwahati 781039, India

CERTIFICATE

It is certified that the work contained in the thesis entitled "**Computational Investigations of Flow and Heat Transfer in Gas-Liquid Slug Flow in Millimeter-Size Channels**", by **Ms. Sadhana Kumari**, has been carried out under my supervision. The work documented in this thesis has not been submitted to any other University or Institute for the award of any degree or diploma.

Dr. Raghvendra Gupta

Assistant Professor

Department of Chemical Engineering

Indian Institute of Technology Guwahati

Guwahati 781039, India

Date

TH-2207_146107023

Acknowledgements

I owe a debt of gratitude to many people who have helped me in completing this research work directly or indirectly throughout my stay in IITG. To begin with, I wish to express my sincere acknowledgement and respect to my supervisor, Dr. Raghvendra Gupta for being a source of my inspiration and guidance all throughout my research work. I am thankful to him for his useful suggestions and constant encouragement throughout my entire work period and feel fortunate enough to have worked under him all these years. The calm demeanour, dedication towards work and ease of handling the toughest of situations are the traits that I hope to inculcate from my supervisor. He has been a moral support throughout my bad times and has always provided me with the freedom to carry out my work without any pressure in the most amicable manner. For this I shall forever be indebted to him.

I would like to thank my doctoral committee members, Dr. Anugrah Singh, Dr. Rajesh Kumar Upadhayay (Department of Chemical Engineering), and Dr. Manmohan Panday (Department of Mechanical Engineering) for their valuable suggestions and constructive criticism during the project evaluations, which helped me to make necessary improvements in various stages of my research work. I would specially like to thank Dr. Anugrah Singh and Dr. Rajesh Kumar Upadhayay for the rigorous and remarkable questions that they raised during the seminar presentations which had helped me a lot in understanding many facts related to my work as well as in improving my presentation and writing skills.

I am also thankful to all the faculty members of the Chemical Engineering Department for their encouragement and help at various stages during my stay in this Department. In this regard, I would specially like to mention the names of Dr. Singh

I would also like to extend my sincere gratitude to the technical officers of my Department, senior technical superintendents, technical superintendent Mr. Jayanta K. Mout, junior technical superintendents Mr. Ariful Hoque and Mr. Debajit Borah and the office staff,

TH-2207_146107023

Mr. Sailen Das, Mr. Deep J. Sinha and Mr. Bhagya Boro. The Computational works presented in this thesis as well as all the official paper work would never have been possible without the help of these proficient technicians.

I extend my sincere thanks to the lab juniors Mr. Neiladri S. Ray, Mr. Ritesh Prakash and Mr. Deepak Kumar Mishra were constant supports in all my work and helped me in having a pleasant work environment in the lab with their untimely help, support and valuable cooperation.

I would like to express my deep gratitude to Mr. Siddarth Khadiya for his help in implementing the k-means clustering algorithm for the bubble coalescence problem. Thanks are also due to Mr. Nilay Sahi who has been of immense help towards my work. I would like to take the opportunity to thank the research scholars in the AR-2B lab for helping me out whenever I approached them with any queries or requirements. I would also like to extend my heartfelt thanks to all of my Ph.D. batch mates and the other research scholars at Chemical engineering department, my IITG friends and my childhood friends who have shared their thoughts and views with me.

I have no words to thank Lord Krishna, Lord Shiva and Lord Ganesha who are my strength and wisdom.

Last but not the least; I would like to thank my father Mr. Ramvilash Chowrasiya, my mother Mrs. Sheela Devi and my elder sibling Mr. Prince Kumar for supporting me to do my Ph.D. My father and mother have always believed in me and moulded me into the strong and independent woman that I am today. My brother has been a moral support during my emotional breakdowns and I could not thank God enough for bestowing me with such a supportive family. Their love, affection, blessings and sacrifices made me stronger to overcome my huddles and achieve my target.

TH-2207_146107023

Acknowledgements

I am indebted to my husband Mr. Saurabh Raj whose constant encouragement, suggestion, patience, and motivation, made me achieve this endeavour in a peaceful and cheerful manner. He transformed all the odds into reality.

Sadhana Kumari

TH-2207_146107023

Abstract

The slug flow regime, generally defined as the periodic flow of alternate channel spanning gas bubbles and liquid slugs, is the most important flow regime during gas-liquid flow in mini and microchannels. In addition to the forward motion of the bubbles and the slugs, there is also internal recirculations within them which render the flow regime very useful for heat and mass transfer applications. Due to its unique hydrodynamic characteristics such as internal recirculation in the slugs as well as bubbles and regular and periodic nature of the flow, slug flow is the preferred flow regime in most of the gas-liquid applications in microchannels. Some examples include membrane fouling prevention, catalyst coating, pulmonary physiology, electronics cooling, heat pipes and microreactors to perform mass transfer limited and exothermic gas-liquid reactions.

The hydrodynamics and heat transfer of long Taylor bubbles in circular capillaries having uniform channel crosss-section for steady gas and liquid flow rates have been studied extensively in the last few decades. There are several other flow conditions which occur during gas-liquid slug flow in micro-structured devices that need to be studied to develop a comprehensive understanding of the physical mechanisms during adiabatic and diabatic two-phase flow and heat transfer in microchannels. In this thesis, the flow and heat transfer in slug flow regime in small diameter channels under different conditions have been studied using computational fluid dynamics (CFD). The CFD simulations have been performed using volume of fluid (VOF) method to capture the gas-liquid interface.

While the hydrodynamics for long Taylor bubbles having volume more than that of a sphere that can fit in the channel has been studied extensively, very little attention has been paid to the bubbles having smaller volume but almost spanning the channel. The bubble volume can be represented

TH-2207_146107023

by the equivalent sphere radius $\left(R_{eqv} = \left(\frac{3V_{Bubble}}{4\pi}\right)^{1/3}/R\right)$, the ratio of the radius of a sphere having the same volume as that of the bubble and channel radius. The hydrodynamics of slug flow for a range of bubble volumes for equivalent sphere radius close to 1, between 0.72-1.55, keeping all other parameters constant has been studied. CFD simulations have been performed in a periodic unit cell consisting of a gas bubble and two halves of adjacent liquid slugs in a frame of reference moving with the bubble. The bubble shape, pressure distribution, bubble velocity, flow field and wall shear stress have been investigated. The hydrodynamic parameters such as bubble shape and wall shear stress has been compared with the experimental data available in the literature and have been found to be in good agreement. The effect of Reynolds and Capillary numbers on the bubble shape for short as well as Taylor bubbles has been investigated. A simple mechanistic model for the wall shear stress for slug flow has been developed.

Further, the effect of change in bubble volume and shape (spherical and Taylor) has been investigated on the heat transfer without phase change. The results show the Nusselt number to be highest for the equivalent sphere diameter close to one. The effect of Reynolds number on the heat transfer has been studied for two cases of R_{eqv} : one having value less than one (0.91) and another having value more than one (1.31). The heat transfer enhancement in gas-liquid slug flow is caused by the internal recirculation in the liquid slug and the slug parameters such as slug length can have a profound effect on the heat transfer. Therefore, the effect of slug length on heat transfer has also been investigated. The heat transfer results have been compared with an extensively validated phenomenological model available in the literature for Nusselt number in gas-liquid and liquid-liquid slug flow.

TH-2207_146107023

The simulations have shown that the velocity of a small spherical bubble is greater than that of a long capsular bubble. Therefore, when a long bubble is followed by a shorter one, it is expected that they would coalesce and form a longer capsular bubble. The coalescence process can be divided in three stages: bubble approach, drainage of the submicron size liquid film between the bubbles leading the contact of bubbles and growth of the bubble. The hydrodynamics during the bubble approach and growth of the bubble after merger has been studied in a frame of reference moving with the longer bubble.

In micro-devices, sudden contractions and expansions of the channel are encountered frequently. With a sudden change in the channel dimension, significant changes in the hydrodynamics of two-phase flow passing through such a system are expected. Two-phase flow of ethylene glycol and air has been simulated for the cases of sudden expansion and contraction of the channel. The simulations have been performed in a laboratory frame of reference and the bubble dynamics at the area change has been studied. Bubble velocity, shape, change in pressure drop through the channel with the change in bubble location has been studied.

In several gas-liquid applications, the flow is not steady and subjected to oscillatory behaviour. Flow and heat transfer in the slug flow regime subjected to a pulsatile flow has been studied for different frequencies ranging between 1-100 rad s^{-1}. The effect of oscillations on the bubble velocity, wall shear stress, pressure drop and Nusselt number has been studied. The simulations have been performed in a frame of reference moving with the bubble with a sinusoidally varying flow at the domain inlet. While there is no appreciable change in the bubble shape, the film thickness oscillates continuously with time. The bubble velocity oscillates sinusoidally in phase with the two-phase velocity specified at the inlet. The Nusselt number is observed to increase more

TH-2207_146107023

than that for steady flow at low frequencies but at higher frequencies, the Nusselt number decreases.

TH-2207_146107023

Research Publications

Published

- **S. Kumari,** N. Kumar, R. Gupta**, "Effect of Gas-Liquid Ratio on the Wall Shear Stress in Slug Flow in Capillary Membranes "** Asia-Pacific Journal of Chemical Engineering, 13 (2018), 2258.
- **S. Kumari,** N. Kumar, R. Gupta, **"Flow and Heat Transfer in Slug Flow in Microchannels: Effect of Bubble Volume"** International Journal of Heat and Mass Transfer, 129 (2019), 812–826.

Submitted

- S. Khadia, **S. Kumari,** R. Gupta, **"Hydrodynamics of Coalescence of Short and Long Bubbles in Microchannels: A CFD Study"** International Journal of Heat and Mass Transfer, (Submitted)

Conferences

Paper

- **S. Kumari,** R. Gupta, **"Effect of Sudden Change in Channel Diameter on Bubble Dynamics in Millimeter-size Channels"** FMFP 2018

Oral

- **S. Kumari,** N. R. Shekher, R. Gupta, "Hydrodynamics of annular flow in microchannels" **7th International conference on Chemical, Agriculture, Environment and Natural Sciences (CAENS-2017)**, 20-21 November 2017, **Kuala Lumpur, Malaysia.**
- **S. Kumari,** N. Kumar, R. Gupta, "A computational study on the effect of gas-liquid ratio on the wall shear stress in slug flow in capillary membranes" **Emerging trends**

TH-2207_146107023

in separation science and technology-SESTEC 2016, 17-20 May, 2016, **Indian Institute of Technology Guwahati**.

Poster

- **S. Kumari,** S. Khadia, R. Gupta, "Flow and heat transfer during coalescence of short and long bubbles in a microchannel" **Research Conclave"** 16-19 March, 2017, **Indian Institute of Technology Guwahati**.
- **S. Kumari,** R. Gupta, "Coalescence of Short and Long Bubbles in Microchannels" **CompFlu-2016,** 12-14 December, 2016, **International Indian Institute of Information Technology Hyderabad**.
- **S. Kumari,** R. Gupta, "CFD modelling of gas-liquid slug-annular flow in microchannels" **CHEMCON-2015**, 27-30 December, 2015, **Indian Institute of Technology Guwahati.**
- **S. Kumari,** R. Gupta, Multiphase Microfluidics, **REFLUX 2015**, 27-29 March, 2015, **Indian Institute of Technology Guwahati.**

Short Term Course

- Course by **Indian Institute of Technology Guwahati** on "Multiphase Flow reactors insights through Experimental and CFD Techniques", 16-20 December 2014.

TH-2207_146107023

CONTENTS

TH-2207_146107023

TH-2207_146107023

CONTENTS

TH-2207_146107023

TH-2207_146107023

LIST OF FIGURES

TH-2207_146107023

TH-2207_146107023

TH-2207_146107023

TH-2207_146107023

TH-2207_146107023

TH-2207_146107023

TH-2207_146107023

TH-2207_146107023

LIST OF TABLES

TH-2207_146107023

Nomenclature

List of Symbols

Greek Letters

α	Volume fraction of one of the phases
β	Homogeneous void fraction i.e. ratio of volumetric gas flow rate to the total volumetric flow rate
δ_F	Film thickness (m)
δ_{min}	Minimum film thickness i.e. minimum distance between the bubble and the wall (m)
$\delta(\mathbf{r})$	Dirac delta function
ε_G	Void fraction
κ	Curvature (m^{-1})
μ	Dynamic viscosity (kg m^{-1} s^{-1})
ρ	Density (kg m^{-3})
σ	Surface tension (N m^{-1})
τ_w	Wall shear stress (Pa)
ω	Angular Frequency (rad s^{-1})
Δt	Time step (s)
Δx	Spacing of the grid (m)

Roman Letters

A	Area (m^2)
a_1,a_2	Constants
A_{ch}	Channel cross sectional area (m^2)
A_F	Cross section area of the film (m^2)
Bo	Bond Number
C_1	Constant
Ca	Capillary Number $\mu U_{TP} / \sigma$
C_p	Specific heat capacity (J kg^{-1} K^{-1})
D_{Hyd}	Hydraulic diameter (m)

TH-2207_146107023

d	Channel diameter (m)
F_{SV}	Surface Tension Force per unit volume (N m^{-3})
g	Acceleration due to gravity (m s^{-2})
h	Enthalpy (J kg^{-1})
k	Thermal conductivity (W m^{-1} K^{-1})
L	Length (m)
L_{UC}	Length of unit cell (m)
L_B	Length of bubble (m)
Ls	Length of slug (m)
L_S^*	Inverse Graetz number ($Ls/RePrd$)
Pr	Prandtl number $\left(\frac{C_P \mu}{k}\right)$
Nu	Nusselt number
Nu*	Nusselt number normalized by that for single phase, fully-developed flow for the same thermal boundary condition on the wall
$\hat{n}$	Unit vector normal to the interface
P	Pressure (Pa)
$\dot{Q}$	Volumetric flow rate (m^3 s^{-1})
q	Heat flux (W m^{-2})
R	Channel radius (m)
RMS	Root mean square
R_{eqv}	Ratio of the diameter of a sphere having same volume as that of the bubble to the channel diameter
Re	Channel Reynolds number $dU_{TP}\rho_L/\mu_L$
$\boldsymbol{r}_{int}$	Position vector of the interface (m)
$\boldsymbol{r}$	Position vector (m)
T	Temperature (K)
t	Time (s)
U_{Mean}	Mean two phase velocity over a cycle (m s^{-1})
U_{Amp}	Amplitude velocity (m s^{-1})
U_F	Average film velocity (m s^{-1})
U_{TP}	Mixture or two-phase velocity (m s^{-1})

TH-2207_146107023

U_{TP1}	Mixture or two-phase velocity for smaller diameter (m s^{-1})
U_{TP2}	Mixture or two-phase velocity for larger diameter (m s^{-1})
U_B	Bubble velocity (m s^{-1})
U_{LS}	Liquid superficial velocity (m s^{-1})
V_{Bubble}	Bubble volume (m^3)
$\boldsymbol{v}$	Velocity vector (m s^{-1})
x	Axial coordinate (m)
W	Womersley number
We	Weber Number

Subscript

avg	Average
B	Bulk
C	Centre of liquid slug
Ci	i^{th} bubble end from inlet
eqv	Equivalent
G	Gas
J	Cost function
int	Interface
l	Large bubble
L	Liquid
LO	Liquid only
out	Outer
m	Bulk mean
S	Slug
s	Small bubble
Slug	Liquid slug
TP	Two phase
UC	Unit cell
W	Wall
r	Radial coordinate

TH-2207_146107023

x	Axial coordinate
w	Wall

TH-2207_146107023

Chapter 1
Introduction

TH-2207_146107023

CHAPTER 1

Introduction

This chapter highlights the motivation of this work. The objectives of the thesis and its organization are presented.

1.1 Motivation

Advances in manufacutring technology in the past few decades have brought the trend towards miniaturisation in a range of industries including electronics (Karayiannis and Mahmoud, 2017, Marcinichen *et al.*, 2013), automotive, aerospace (Raghu, 2012), pharamaceutical, biomedical and healthcare (Prothero and Burton, 1961, Gaver *et al*., 1996; Suresh and Grotberg, 2005; Zheng *et al*., 2007), energy and chemical processing (Kolb and Cerro, 1991, Kreutzer *et al*., 2005, Khan *et al*., 2004, Günther *et al*., 2004, Kumar *et al*., 2007, Rajesh and Buwa, 2018). Efficient heat removal is a primary requirement in a number of applications of microstructured devices such as cooling of electronics equipment, compact heat exchangers (Bao *et al*., 1994), refrigeration and airconditioning (Zhao and Bi, 2001) and microreactors performing exothermic reactions (de Mas *et al*., 2003).

While the correlations developed for single phase flow and heat transfer in conventional (macro) channels can be successfully used to predict flow and heat transfer in microchannels with due consideration for the channel roughness (Park and Punch, 2008, Kumar *et al.*, 2011), the same is not true for flow and heat transfer in gas-liquid flow and boiling. Consequently, continuous efforts are being made to develop a thorough understanding of the flow and heat transport with and without phase change in gas-liquid flow in microchannels.

TH-2207_146107023

During gas-liquid flow in microchannels, a number of geometric arrangement of the two phases, commonly referred as flow patterns or flow regimes can occur depending on the gas and liquid flow rates. These flow patterns can be categorised in five groups namely: bubbly, slug, slug-annular, annular and churn (Dessimoz *et al*., 2010, Zhao and Bi, 2001, Revellin *et al.*, 2006). Similarly, during flow boiling in microchannels, the flow regime changes from bubbly to slug to slug-annular and then annular with an increase in the vapour quality (Harirchian and Garimella, 2009, Baldassari *et al.*, 2012, Kumar *et al.*, 2017). During the flow regime transition from bubbly to slug flow, first spherical, channel-size bubbles appear which further grow to Taylor bubble shape with an increase in the bubble volume (Ali *et al.*, 2013). The rate of heat transfer strongly depends on the flow regime (Bao *et al.*, 2000; Thome *et al.*, 2013).

Amongst these flow regimes, slug flow occurs over a wide range of gas and liquid flow rates. The area occupied by slug flow on the flow regime map increases with a decrease in the channel dimension because of the increased importance of capillary forces at small scale (Thome *et al.*, 2013). In gas-liquid flow in microchannels, slug flow is very regular and periodic. The slug flow regime is generally defined as the periodic flow of alternate gas bubbles and liquid slugs. The bubbles are of the size of the channel and occupy almost the entire channel cross-section. A thin liquid film surrounds the gas bubble and also joins the two slugs on the two sides of the bubble. In addition to the forward motion of bubbles and slugs, there is also internal recirculations within them which render the flow regime very useful for heat and mass transfer applications. This flow regime is also known as segmented flow as the segmentation of the continuous phase fluid can be achieved by channel-size bubbles.

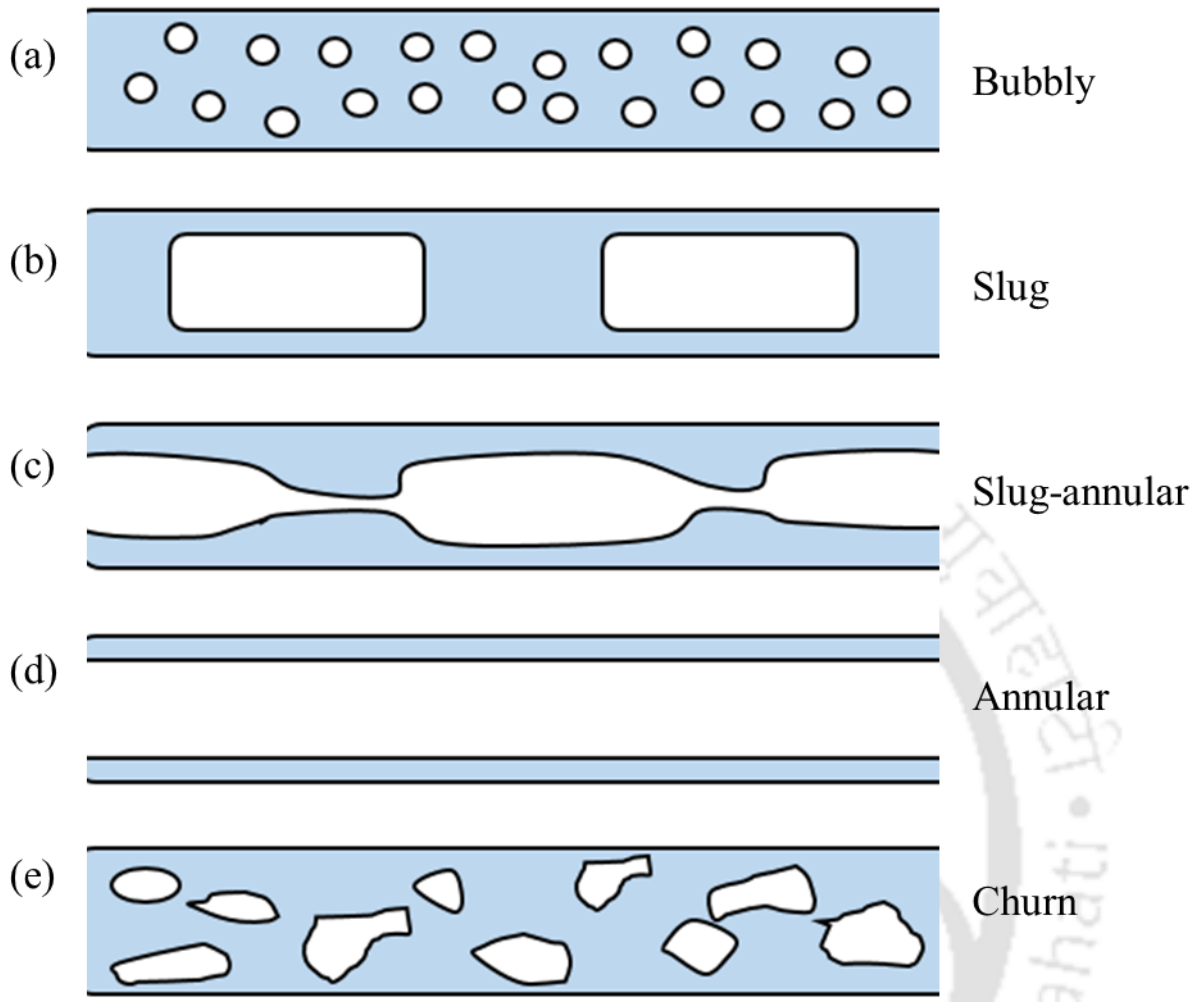

Figure 1.1. Systematically the flow regime for air-water flow in a millimeter-size channel.

Due to its unique hydrodynamic characteristics such as internal recirculation in the slugs as well as bubbles / droplets and regular and periodic nature of the flow, slug flow is the preferred flow regime in most of the gas-liquid applications in microchannels. Some examples include membrane fouling prevention (Laborie and Cabassud, 1995), catalyst coating (Kolb and Cerro 1991), microcirculation (Prothero and Burton, 1996), pulmonary physiology (Gaver *et al.*, 1996; Suresh and Grotberg, 2005; Zheng *et al.*, 2007) and microreactors to perform mass transfer limited gas-liquid reactions (Günther *et al.*, 2006). The applications for heat transfer specifically include

electronics cooling (Marcinichen *et al.*, 2013), heat pipes (Mehta and Khandekar, 2014) and exothermic gas-liquid reactions (de Mas *et al.*, 2003).

The hydrodynamics and heat transfer of long Taylor bubbles in circular and rectangular microchannels having uniform channel crosss section for steady gas and liquid flow rates have been studied extensively in last few decades. There are several other flow conditions which occur during gas-liquid slug flow in micro-structured devices that need to be understood to develop a comprehensive understanding of the physical mechanisms during adiabatic and diabatic two-phase flow in microchannels. In this thesis, the flow and heat transfer in slug flow regime in small diameter channels under different conditions, discussed in the following section, have been studied using computational fluid dynamics (CFD).

1.2 Thesis Objectives:

This thesis aim to understand the dynamics of channel-size bubbles and their effect on heat transfer during gas-liquid slug flow in millimeter-size channels using computational fluid dynamics (CFD). The main objectives can be outlined as:

- The smallest channel occupying bubbles are spherical in shape and an increase in the bubble volume causes a transition to a capsular shape. The first objective of this thesis is to investigate the transition in the bubble shape and velocity caused by an increase in the bubble volume. The effect of an increase in the Reynolds number on the shape and velocity of both spherical and capsular bubble is also studied. The effect of the gas bubble on the shear stress on the channel wall, an important parameter in many engineering applications, is investigated.
- Convective heat transfer in the slug flow regime can be significantly higher than that for liquid-only flow and strongly depends on the bubble and slug volumes. The second objective of the

thesis is to understand the effect of bubble volume and slug length on the heat transfer in gas-liquid slug flow.

- The low-volume spherical bubble and the Taylor-shaped bubbles move with different velocities. The spherical bubble moves toward, and under certain circumstancs coalesces with, the Taylor bubble. The hydrodynamics of the bubble approach and growth after contact has been studied.
- A sudden change in the channel cross-sectional area, expansion as well as contraction, is a common occurrence in micro-structured devices. A change in the channel cross-sectional area is expected to cause change in the bubble velocity, pressure drop. The next objective of this thesis is to understand the bubble dynamics and associated hydrodynamics during sudden expansion and contraction of the channel.
- Under many circumstances, the gas-liquid flow may be subjected to oscillations. The next objective of the thesis is to investigate the effect of oscillations on the hydrodynamics and heat transfer over a range of oscillation frequencies.

1.3 Thesis Organization

Chapter 2 presents the basic terminology and definitions relevant to this work. The background and literature relevant to the work are presented and the research gaps in the literature are identified.

Chapter 3 presents a mathematical framework to model slug flow in capillaries. The governing equations for the Volume of Fluid (VOF) method used to model slug flow in this work are presented. Further, two different approaches to model fully-developed gas-liquid slug flow are also discussed.

Chapter 4 presents the methodology to model isothermal slug flow in a periodic computational domain. The hydrodynamics of the slug flow is studied to understand the effects of bubble volume ranging from channel encompassing near-spherical bubble to long Taylor bubble, Reynolds numbers and capillary numbers. A simple mechanistic model for wall shear stress in slug flow is also presented.

In **Chapter 5** the methodology to model heat transfer without phase change for constant wall heat flux boundary condition in a periodic computational domain is presented. The effect of bubble volume, Reynolds number and slug length on Nusselt number is studied. The results obtained are compared with a simple phenomenological model for Nusselt number in slug flow regime available in literature.

In **Chapter 6** the coalescence of two bubbles having different volumes, a long Taylor bubble followed by a short, near spherical bubble is studied. The approach of the bubbles and the evolution of the bubble after the merger is studied.

In **Chapter 7** the bubble dynamics in a channel having sudden change in channel diameter is studied. The cases of sudden increase as well as sudden decrease in channel diameter downstream of the flow are considered.

In **Chapter 8** the flow and heat transfer in Taylor flow under oscillatory conditions are studied. The oscillations to the flow are caused by specifying a time-dependent sinusoidal velocity boundary condition at the inlet. The effect of the frequency on the bubble shape and velocity, pressure drop over a unit cell and Nusselt number are studied.

Finally, **Chapter 9** presents the conclusions obtained from this work. The suggestions for the future work are also made.

Chapter 2
Literature Review

TH-2207_146107023

CHAPTER 2

Literature Review

In this chapter, a brief overview of gas-liquid flow in small diameter channels is given. The important definitions used in this thesis, typical flow regime map for gas-liquid flow in small diameter channels are presented. A comprehensive review of the hydrodynamics and heat transfer without phase change in the slug flow regime is presented. Finally, the knowledge gaps in the literature are identified.

2.1 Important Definitions and Terminology

2.1.1 Microchannel: The term 'microchannel', in a literal sense, refers to a channel of the size of few microns. However, the term is often used for the channels having size ranging from few microns to the channels of size ~1 mm. Several definitions of 'microchannel' exist in the literature (Baldassari *et al.,* 2012, Kandlikar *et al.,* 2003).

Many researchers have formulated the transition criteria from a purely geometric standpoint while others considered the relative important of buoyancy and capillarity effect as a criterion to define the microchannel. For example, Mehendale *et al.* (2000) classified channels having diameter in the range of 1 μm to 100 μm as microchannels. Kandlikar *et al.* (2006) proposed a detailed classification of the small diameter channels. They classified the channels having hydraulic diameter in the range of 200 μm to 3 mm as minichannels and those having diameters between 10 and 200 μm as microchannels. Triplett *et al.* (1999) proposed the capillary length ($d = \sqrt{\sigma / g\Delta\rho}$) as the criteria for the channel be 'micro'. For air-water flow at room temperature, the capillary

TH-2207_146107023

length comes out to be ~2.7 mm. At this length, the buoyancy force, a volume effect and capillary effect, a surface effect are of same order of magnitude and the capillary effect starts to dominate at channel dimension below capillary length.

2.1.2 Superficial Velocity: Superficial velocity of a phase is defined as the ratio of the phase flow rate and the channel cross-sectional area.

2.1.3 Mixture or Two-Phase Velocity (U_{TP}): Two-phase or the mixture velocity is the sum the gas and liquid superficial velocities in gas-liquid flow. Alternatively, it is the total volumetric flow rate per unit channel cross-sectional area.

2.1.4 Equivalent Sphere Radius (R_{eqv}): The equivalent sphere radius is defined as the ratio of the diameter of a sphere having same volume as that of the bubble and the channel radius.

$$R_{Eqv} = \left(\frac{3V_{Bubble}}{4\pi}\right)^{1/3} / R \tag{2.1}$$

2.1.5 Homogeneous Void Fraction (β): Homogeneous volume fraction is the volume fraction of a phase if both the phases are mixed homogeneously and move with the same velocity. It can be defined as the ratio of volumetric flow rate of a phase to the total volumetric flow rate. The homogeneous void fraction often refers to the homogeneous volume fraction of the gas phase.

$$\beta = \text{Volume of gas/ Total volume}$$

2.1.6 Void Fraction (ε_G): In most of the cases encountered in gas-liquid flows, the two phases are not homogeneously mixed and the phases redistribute themselves downstream in the channel. Void fraction is the volume fraction of the gas phase once the phase has redistributed themselves. In a slug flow it can be defined as the gas volume fraction in a unit cell consisting of a gas bubble and a liquid slug.

TH-2207_146107023

2.1.7 Reynolds Number (*Re*): Reynolds numbers for two-phase slug flow has been defined based on the two-phase velocity (U_{TP}), channel diameter (d) and physical properties (ρ_L, μ_L) of the continuous liquid phase.

$$Re = \frac{d\rho_L U_{TP}}{\mu_L} \tag{2.2}$$

2.1.8 Bond Number (*Bo*): Bond or Eötvös number is the ratio of the buoyancy and capillary forces. It is an important indicator of the relative importance of the body and surface forces and the channel dimension at which small size effects start dominating.

$$Bo = \frac{\Delta\rho g d^2}{\sigma} \tag{2.3}$$

2.1.9 Capillary Number (*Ca*): Capillary number, the ratio of viscous force and surface tension, has been defined based on the two-phase velocity (U_{TP}) and physical properties (μ_L, σ) of the liquid phase. Ideally, the capillary number should be defined based on the bubble velocity (U_B), however as the bubble velocity is not known a priori and differ only by few percent from the two-phase velocity for low viscosity fluids, two-phase velocity is a good approximation under most conditions.

$$Ca = \frac{\mu_L U_{TP}}{\sigma} \tag{2.4}$$

2.1.10 Nusselt Number (*Nu*): Nusselt number is the ratio of the convective and conductive rates of heat transfer and is defined as

$$Nu = \frac{hd}{k_L} \; where \; h = \frac{q_w}{(T_W - T_B)} \tag{2.5}$$

The thermal conductivity of the liquid phase has been used in the definition as for all the cases simulated in this work, the liquid phase alone is in contact with the wall. While definition of the wall and bulk mean temperature is obvious in single phase flow, it can be defined in a number of

TH-2207_146107023

ways for two-phase flows. The definition of the Nusselt number used in this work is presented in Chapter 5.

2.1.11 Womersley Number (α): Womersley number is used to characterise the pulsatile or oscillatory behaviour of the flow and is used in biological flows frequently (Mazumdar, 1992). It compares the oscillatory inertial and the viscous forces.

$$\alpha^2 = \frac{\rho\omega R^2}{\mu} \tag{2.6}$$

2.2 Gas-liquid Flow in Microchannels: Flow Regimes

Depending upon the gas and liquid flow rates, channel size and fluid properties, the two fluids rearrange themselves in a number of different geometric patterns, often known as flow regimes or flow patterns. While the channel orientation has a major effect on the flow regime in large diameter channels, such is not the case in small diameter channel. As shown in Fig. 2.1, the major flow regimes observed are bubbly, slug/plug, churn, slug-annular and annular. At low gas superficial velocities and intermediate to high liquid superficial velocity, the bubbly flow regime occurs, in which finely dispersed bubbles in a continuous stream of liquid are observed. As the gas superficial velocity is increased, numerous small bubbles coalesce to form elongated channel-size bubbles separated by slugs of liquid slugs to give rise to the 'slug' flow regime. At high gas flow rates, the 'Annular' flow regime characterised by a continuous gas core at the centre of the channel and a thin liquid film towards the channel wall appears. The transition regime between slug and annular flow in which a continuous gas core having large waves on the interface or merging of long bubbles is known as the slug annular flow regime. At high gas and liquid flow rates, churn flow regime is observed.

TH-2207_146107023

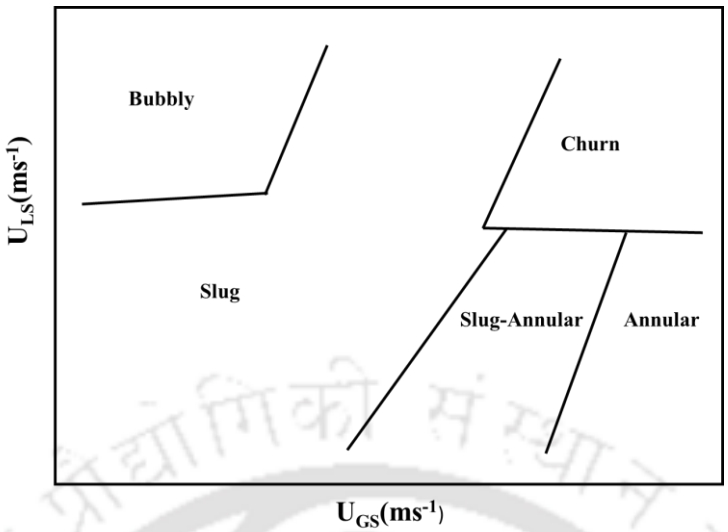

Figure 2.1. A representative flow regime map for air-water flow in a millimeter-size channel.

2.3 Slug Flow

In past two decades, a lot of attention has been paid to understand the momentum, heat and mass transfer in slug flow in microchannels. As shown in Fig. 2.2, slug flow is characterised by a train of capsular gas bubbles of almost of the size of the channel. The bubbles are separated by a thin liquid film from the wall. Two consecutive bubbles have slugs of liquid between them which move with the same velocity as that of the bubbles. The flow is periodic and regular. The flow pattern is also named as Taylor flow, plug flow and segmented flow. The liquid slugs as well as gas bubbles have internal recirculations inside them which can be seen in a frame of reference moving with the bubble.

Slug flow regime has been studied extensively using experimental as well as computational techniques due to its importance in a number of applications such as compact heat exchangers, electronics cooling, heat pipes, gas-liquid reactions, airway opening, catalyst coating over monoliths and membrane fouling removal (Gupta *et al.,* 2010). For detailed review of slug or

TH-2207_146107023

Taylor flow regime, the readers are suggested to refer to some of the recent reviews (Gupta *et al.*, 2010, Bandara *et al.*, 2015, Haase *et al.*, 2016). Recently, in a series of articles, Abiev presented simple mechanistic models to predict void fraction (2010), pressure drop (2011, 2015), bubble velocity, recirculation time and mass transfer (2013), bubble shape (2017) in Taylor flow regime.

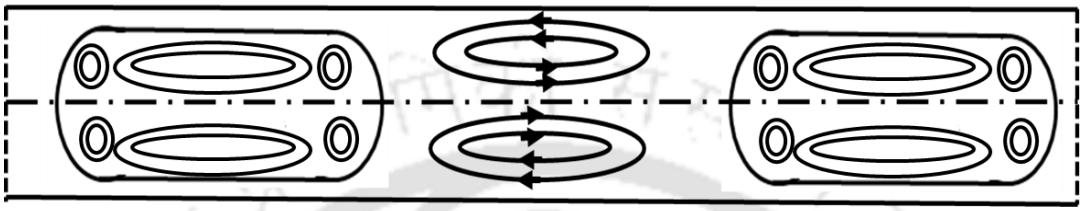

Figure 2.2: A Schematic of the slug flow regime.

2.3.1 Hydrodynamics

2.3.1.1 Film Thickness and Bubble Shape

The thickness of the liquid film surrounding the bubble plays an important role in the hydrodynamics of Taylor flow as the film thickness is directly related to bubble velocity. Moreover, film thickness is an important parameter in several applications e.g. catalyst coating in monolith reactors (Kolb and Cerro, 1991), heat and mass transfer from wall to liquid (van Baten and Krishna, 2004; Kreutzer *et al.*, 2005a).

Two different methods are found in the literature for measuring the film thickness experimentally: (i) direct methods: in the direct method, the film thickness is directly measured using high quality images either free from the optical distortion caused by curved channel wall (Aussillous and Quéré, 2000) or corrected for the optical distortion (Han and Shikazono, 2009) (ii) indirect methods: in the indirect method the bubble velocity is determined experimentally and then the film thickness is calculated using continuity. This requires information of the velocity profile in the liquid film. While some researchers have treated the film as being immobile (Suo and Griffith, 1964; Warnier *et al.*, 2008),

TH-2207_146107023

Table 2.1: Film Thickness

Author	Range of Validity	Formula
Bretherton (1961)	below $10^{-4}$and above 10^{-2}	$\frac{\delta_F}{R} = 1.34Ca^{2/3} (2\times10^{-4} < \text{Ca} < 2\times10^{-3})$
Aussillous and Quéré (2000)	0.001-1.25	$\frac{\delta_F}{R} = \frac{1.34Ca^{2/3}}{1+3.34Ca^{2/3}}$
Klaseboer *et. al.*, (2014)	Ca upto 2	$\frac{\delta_F}{R} = \frac{0.643(3Ca)^{2/3}}{1+1.79(3Ca)^{2/3}}$
Han and Shikazono (2009)	Re < 2000	$\frac{\delta_F}{R} = \frac{1.34\,Ca^{2/3}}{1+3.13Ca^{2/3}+0.54Ca^{0.672}Re^{0.589}-0.352We^{0.629}}$
Fairbrother and Stubbs (1935)	0.013 < Ca < 0.09	$\frac{\delta_F}{R} = 0.5Ca^{1/2}$
Marchessault and Mason (1960)		$\frac{\delta_F}{R} = -0.05\left(\frac{\mu_c}{\sigma}\right)^{1/2} + 0.89Ca^{1/2}$
Irandoust & Andersson (1989)	0.001-1.25	$\frac{\delta_F}{R} = 0.36(1-e^{-3.08Ca^{0.54}})$
Kreutzer *et. al.*, (2001)	0.001-3	$\frac{\delta_F}{R} = 0.36(1-e^{-2.18Ca^{0.52}})$
Thulasidas *et. al.*, (1995)	0.001-3	$\frac{\delta_F}{R} = 2(0.357-0.25e^{-2.25Ca^{0.445}})$
Han *et. al.*, (2009)	0-0.38	$\frac{\delta_F}{R} = \frac{0.67Ca^{2/3}}{1+a_1+a_2-a_3}$ $a_1 = 3.13Ca^{2/3}, a_2 = 0.504Ca^{0.672}\,\text{Re}^{0.589}, a_3 = 0.352We^{0.629}$

TH-2207_146107023

others assumed a fully-developed annular flow velocity profile or fully-developed velocity profile in the liquid film with a no shear boundary condition at the interface (Thulasidas *et al.,* 1995). Researchers have developed several expressions for film thickness calculation as given in Table 2.1. The ranges of validity of the expressions have also been given. Some of these e.g. Bretherton' expression (1961), Klaseboer *et al.,* (2014) have been derived analytically while some are semi-empirical e.g. Aussillous and Quéré (2000) and several others are empirical in nature. While Aussillous and Quéré expression (2000) is semi-empirical, Klaseboer *et al.,* (2014) showed that it can be derived from first principles.

Bubble Shape:

The gas bubble can be approximated as a cylinder with hemispherical caps at the ends. For low-viscosity fluids (high value of $\frac{Re}{Ca}$), the aspect ratio of the nose increases, i.e. the length of the nose increases and the radius of the bubble decreases (de Ryck, 2002). For highly viscous liquids (low value of $\frac{Re}{Ca}$), this effect is small and there is little change in aspect ratio. With increasing capillary number, the bubble tail becomes flatter and at still higher values of the capillary number, the bubble tail takes a concave shape (Feng, 2009). This deformation of bubble shape is more prominent at higher Reynolds number (Walsh *et al.,* 2009). Near the tail of the bubble, some twists are observed in the gas-liquid interface and the amplitude of these twists increases with an increase in the Reynolds number (Edvinsson and Irandoust, 1996).

2.3.1.2 Bubble velocity

The bubble velocity is obtained from the simulations and is used to calculate homogeneous void fraction (β) i.e. gas volume fraction if the two phases are homogeneously mixed. When the two phases are homogeneously mixed, there is no slip between the two phases and both the phases

TH-2207_146107023

move with the same velocity. Researchers have given some correlations for bubble velocity calculations in Table 2.2.

Table 2.2: Bubble Velocity

Author	Range of Validity	Formula
Armand Correlation (Clift, Grace and Weber, 1978)		$\frac{U_B}{U_{TP}} = 1.2$
Liu *et al.*, (2005)	$0.0002 < Ca < 0.39$	$\frac{U_B}{U_{TP}} = \frac{1}{1-0.61Ca^{0.33}}$
Suo and Griffith, 1964	For all	$\frac{U_B}{U_{TP}} = \frac{\beta}{\varepsilon_G}$
Abiev and Lavretsov *et al.*, (2012)	For all	$\frac{U_B}{U_{TP}} = \frac{1}{\left(1-\frac{\delta_F}{R}\right)^2}$

2.3.1.3 Velocity Field

The motion in the liquid slug can be decomposed into two components: a forward moving bubble velocity and a recirculating velocity. The liquid slug is always seen as forward moving. Thulasidas *et al.*, (1997) calculated the location of the centre and the size of the recirculating portion of the liquid slug and also observed that for liquid slugs longer than 1.5 channel diameters, the flow in the liquid slug becomes fully-developed and a parabolic velocity profile is obtained.

2.3.1.4 Shear Stress

The shear stress is an important parameter during the application of gas-liquid slug flow in membrane fouling prevention. For example, Cabassud and co-workers studied experimentally the

TH-2207_146107023

effect of slug flow in improving filtration flux. Cabassud *et al.*, (1997) studied the use of gas-liquid flow in hollow fibre membranes to mitigate membrane fouling for flow of water containing clay suspension. They attributed the fouling removal capacity of slug flow to the high wall shear stress induced by the air bubbles. They observed the permeate flux to increase up to two fold because of continuous air injection compared with the case when air was not injected. To characterise the wall shear stress on the membrane, Laborie and Cabassud (2005) measured the local wall shear stress over a range of gas and liquid flow rates in a capillary tube of internal diameter 1 mm during gas-liquid slug flow employing an electrochemical method.

Cui and co-workers studied the hydrodynamics and shear stress distribution during slug flow using experimental and computational techniques for application in membrane fouling removal (Taha and Cui, 2002a,b; 2006). Taha and Cui (2002a) modelled slug flow in ultrafiltration membranes using volume of fluid (VOF) method and calculated bubble shape, slug velocity, wall shear stress distribution on the membrane tube. The calculated shear stress was then used to predict the permeate flux which was compared with the experimentally obtained values and found to be in good agreement.

Ratkovich *et al.,* (2009) measured the shear stress in vertically upward gas-liquid slug flow using electrochemical shear probe in Plexiglas tube of diameter 9.9 mm, having diameter similar to those of tubular membranes used in membrane bioreactors. They also developed a CFD model employing volume of fluid method to model the slug flow in an axisymmetric computational domain and validated the model by comparing the bubble velocity and wall shear stress with that obtained experimentally. They noted that the bubble length and hence the shearing duration varied significantly even in a single experiment because of the coalescence of bubbles, especially at high gas and low liquid flow rates, as the bubble travelled up in the channel. To quantify the shear stress

TH-2207_146107023

on the tube, they used shear stress histograms showing the relative frequency of a given magnitude and direction and observed a positive surface shear peak in the liquid slug. They also highlighted that the change in the sign of the shear stress can be correlated with the fouling control. Further, they developed empirical models to predict the shear stress histograms, pressure drop and energy consumption in the tubular membranes (Ratkovich *et al.*, 2011).

The experiments as well as CFD simulations in the literature show the peaks in the shear stress magnitude on the wall to be higher at the bubble ends i.e. at the nose and tail of the bubble with little contribution of the middle region of the bubble in the wall shear stress. It can therefore be advantageous to have short bubbles which occupy the channel but has very short or no cylindrical region in the middle.

2.3.2 Heat Transfer in Slug Flow

The rate of heat transfer in Taylor flow regime has been observed to be significantly higher than that in fully-developed, liquid-only flow experimentally (Mehta and Khandekar, 2014, Babin *et al.*, 2015, Scammell and Kim, 2015) as well as numerically (Gupta *et al.*, 2010, Asadolahi *et al.*,, 2012, Zhang *et al.*,, 2016). Gupta *et al.* (2010), Talimi *et al.* (2012) and Bandara *et al.* (2015) have reviewed heat transfer without phase change in the Taylor flow regime in gas-liquid flow in microchannels.

Asadolahi *et al.* (2011, 2012) studied heat transfer in Taylor flow regime in gas-liquid flow in microchannel usig CFD and validated the results extensively with the experimental data and the simulation results showed excellent agreement with the bubble shape, film thickness, bubble velocity obtained from experiments. Heat transfer simulations also reproduce the data well with a maximum difference of 15% except for high Reynolds number cases ($Re_{TP} \geq 951$), for which it is

TH-2207_146107023

no longer valid to assume two-dimensional, axisymmetric flow. Also, studies on mass transfer in the Taylor flow regime in microchannels have shown the transport rates to be dependent on the length of the liquid slug. There were two approaches. The first, is to generate bubbles and slugs in a long tube using a time-dependent boundary condition. In the second method, the flow and heat transfer are modelled in a single unit cell, with a bubble surrounded by liquid slugs. There was a very large difference between the required computational mesh sizes and times for the two methods. The hydrodynamic and heat transfer results obtained from the two approaches were found to be very similar to each other and with results from earlier verification and validation studies.

Leung *et al.* (2010) studied experimentally the flow and heat transfer behaviours of gas–liquid (nitrogen and water), non-boiling, Taylor flow, with a 2 mm diameter channel oriented in the vertical direction. Three circular T-junction mixers with different diameters were used to generate gas bubbles and liquid slugs of different lengths (1–220 channel diameters) with controlled mixture velocities ($0.11 < U_{TP} < 0.53$ m s^{-1}, $200 < Re_{TP} < 1100$) and homogeneous void fractions ($0.03 < \beta < 0.90$). High-speed visualization of adiabatic flow and heat transfer rate determination for constant wall heat flux conditions were performed. The heat transfer enhancement in Taylor flow is found to be larger with shorter slugs and higher mixture velocities. An enhancement of heat transfer was observed to be up to 3.2 fold of the liquid-only. Based on the experimental data, a correlation between the apparent slug Nusselt number (Nu_L*) with a Graetz number, where the characteristic length is that of the slug, is proposed.

It has been shown that the Nusselt number in Taylor flow regime can be 2-3 times higher than that in the fully-developed single phase flow in microchannels for constant wall heat flux and constant wall temperature boundary conditions (Gupta *et al.*, 2010). The Nusselt number in gas-liquid

TH-2207_146107023

Taylor flow is a function of fluid properties, bubble and slug lengths, phase flow rates. Leung *et al.* (2010) has developed correlation for heat transfer in Taylor flow regime.

2.4 Bubble Volume: Spherical Bubbles

The hydrodynamics of the Taylor flow regime in gas-liquid flow in microchannels has been studied extensively in the last few decades and extensive reviews can be found in Angeli *et al.* (2008), Gupta *et al.* (2010), Talimi *et al.* (2012), Bandara *et al.* (2015) and Hasse *et al.* (2016). However, little attention has been paid to the short bubbles and the transition in the bubble shape from near spherical to capsular with an increase in the bubble volume.

Ratulowski and Chang (1989) computed pressure drop and film thickness for isolated bubbles as well as for a bubble train over a range of bubble volumes in circular and square capillaries. They observed the rear of the bubble to be wavy for long bubbles but not for very short bubbles.

Lac and Sherwood (2009) studied the deformation of a drop, its velocity and additional pressure drop caused by the presence of the drop in a capillary for pressure driven flow for a range of viscosity ratios, drop sizes and capillary numbers. They found the drop curvature at the front to be higher than that at the rear for all the cases. This deviation from spherical shape was small for low drop volumes and became clearly visible only for $R_{eqv} \geq 0.9$. They found that for $R_{eqv} \geq 1.1$ the front and rear of the drop remained unchanged with an increase in the droplet volume and increase in drop volume merely added to the length of the droplet.

Feng (2010) studied the behaviour of small bubbles ($0.1 < R_{eqv} < 0.95$) in a circular tube for a range of capillary ($0.001 < Ca < 100$) and Reynolds numbers ($0 < Re < 800$). He observed that for small value of *Re*, the velocity of a bubble increased with bubble size for large values of *Ca* but decreased

TH-2207_146107023

for small values of *Ca*. However, a bubble of larger size was observed to move at a slower velocity for all values of *Ca* at large values of *Re*.

As the short, spherical bubbles move with a higher velocity than that of a Taylor bubble, a simultaneous occurrence of the Taylor bubble followed by a shorter bubble may cause the coalesecene of bubbles.

2.5 Coalescence of Bubbles

The flow of bubbles and droplets is encountered in several industrial processes. These include chemical synthesis, gas absorption, food processing, drug discovery, emulsion production, amongst others. The bubbles / droplets of different sizes move with different velocities. This may often cause bubble coalescence.

In microfluidic devices, droplet merging is used as a technique for hydrogel-beads formation and cell transplantation (Shintaku *et al.,* 2007) and nanoparticle synthesis using chemical reactions (Hung *et al.,* 2006). In microscale multiphase reactors, the coalescence of bubbles and drops can influence the heat and mass transfer rates by changing the interfacial area between the phases. The coalescence of bubbles in a gas-liquid reactor can reduce the overall interfacial area, lowering the efficiency of the operation. There are also cases where coalescence is a desirable phenomenon. One such example is controlled coalescence of liquid droplets. Liquid droplets can act as excellent microcarriers, capable of being transported with negligible loss of the liquid or reagents (Deng *et al.,* 2014). Chemical reactions can be carried out with high precision by their controlled coalescence. Therefore, it is important to develop an understanding of the hydrodynamics of the coalescence of bubbles / droplets in microchannels.

Three stages of coalescence

TH-2207_146107023

Three distinct stages have been identified in the coalescence process of bubbles. In the first stage, the bubbles approach each other within the liquid phase, and a thin film of liquid forms between them. In the second stage, the thinning of the film occurs by the drainage of liquid. When the thickness of the film is reduced to about 10 nm, it ruptures, leading to coalescence (Vrij 1966).

The coalescence of bubbles proceeds via the formation of a thin bridge (neck) between them. The surface energy of the bubbles increases as a result of the formation of the thin bridge. It is converted into kinetic energy imparted to the surrounding fluid as the radius increases. Several authors have proposed scaling laws for the rate of growth of the neck with time. Paulsen *et al.* (2014) have given the following equation for the growth of the neck radius by equating the viscous stresses and the Laplace pressure.

$$r(t)/A = C_1 \left(\frac{\sigma}{\mu_{liq} A}\right)^{1/2} t^{1/2} \tag{2.7}$$

where C_1 is a dimensionless prefactor. For the system of air and water $C_1 = 1.2$.

Past studies have established that the volume of bubbles / droplets is an important parameter determining their flow behaviour inside a confined fluid. Employing finite element method, Feng (2010) studied the motion of small bubbles in a tube in a flowing liquid. It was seen that for large values of Reynolds number, a bubble of smaller volume moves at a higher velocity for a given value of capillary number. Almatroushi & Borhan (2006) experimentally studied the pressure-driven flow and coalescence of air bubbles translating through a tube of 7.96 mm diameter. When the separation between the leading and trailing bubbles was greater than one tube diameter, there was no effect of one bubble on the other. Each achieved a steady shape that was the same as that observed for a single bubble of the same size. However, there were measurable changes in the velocity and the shape of the trailing bubble when this distance decreased below one diameter.

TH-2207_146107023

Coalescence was observed for all the cases where the size of the trailing bubble was smaller than the leading bubble.

Recently, the interaction of bubbles / droplets inside a fluid has been investigated using numerical techniques. The coalescence of bubbles in a stagnant liquid has been studied numerically by Chen *et al*, (2011) and Hasan & Zakaria (2011). Hasan & Zakaria (2011) have shown that the VOF approach can be used to model the phenomena accurately. The growth and/or merger of bubbles during phase change was investigated by Magnini *et al.* (2013) and Liu and Palm (2016). Chen *et al.* (2017) studied the coalescence of two unequal bubbles kept in close contact with each other. They observed an increase in coalescence time with a decrease in the size difference between the bubbles. The coalesced bubble was found to be closer to the larger bubble. This phenomenon is called "coalescence preference" and is described by a power law relationship.

As the above literature review suggests, there has been a lot of interest in bubble coalescence in liquids. Although this has led to a few numerical studies of bubbles coalescence in stagnant liquid, the phenomenon is yet to be fully understood when occurring inside a microchannel with a co-flow of the liquid.

2.6 Change in Channel Cross-Section

In micro-devices sudden contractions and expansions are encountered frequently, for example at the channel inlet and outlet connections. With a sudden change in the channel dimension, significant changes in the hydrodynamics of two-phase flow passing through such a system are expected.

Abdelall *et al.* (2005) studied the pressure drop caused by an abrupt flow area expansion and contraction having smaller and larger channel diameters of 0.84 and 1.6 mm, respectively for the

TH-2207_146107023

flow of air only, water only and air-water two phase flow. The pressure drop in the zone of area change was found to be in agreement with the correlation available in literature for most of the cases. For two-phase flow, the measured pressure drop in the expansion / contraction zone suggested significant velocity slip at the zone of area change.

Kawahara *et al.* (2015) studied the effect of Reynolds number and contraction ratio on gas-liquid flow across the sudden contraction in horizontal millimeter-size channels of rectangular cross-section experimentally as well as computationally. They estimated the pressure loss due to contraction for single phase as well as two-phase flow. They also developed a correlation for contraction coefficient for liquid flow as a function of Reynolds number and contraction ratio. CFD simulations were performed to capture the bubble shape during contraction using VOF method.

Balakrishna *et al.* (2010) studied experimentally the flow of viscous oil and water in a channel having sudden contraction and expansion. Recently, Sudhakar and Das (2018) studied the evolution of a liquid Taylor shaped droplet in a vertical channel having sudden contraction using the lattice Boltzmann method (LBM) over a range of contraction ratios, droplet volumes and channel inclinations.

2.7 Oscillatory or Pulsatile Flow

Gas-liquid slug flow has been found to enhance heat transfer characteristics in micro-scale devices such as micro-heat exchanger, electronic chips etc. but upon increasing the length of the Taylor bubbles this effect gradually attenuates. Introduction of pulsating Taylor bubbles is another option to enhance local heat transfer.

TH-2207_146107023

Mehta and Khandekar (2014) studied hydrodynamics and heat transfer experimentally in continuous and pulsating gas-liquid Taylor flow for three frequencies 1, 2 and 3 Hz in a square channel of dimension 3 mm. They showed that the introduction of an isolated Taylor bubble caused a substantial increment in heat transfer in its vicinity. During the pulsatile Taylor flow, higher heat transfer rate is observed at 2 and 3 Hz than at 1 Hz and non-pulsatile flow.

Pattamatta *et al.* (2015) studied numerically hydrodynamics and heat transfer in Taylor flow under oscillatory conditions in a channel of diameter 1.2 mm for FC-72 liquid and vapour for four different frequencies 5, 10, 20 and 50 rad s^{-1}. A qualitative comparison between the bubble shapes and a quantitative comparison between the bubble location was made with the experimental data. They observed the average film thickness to decrease with the oscillation frequency. The Nusselt number in the liquid film close to the wall was estimated from the simulations which was inversely proportional to the film thickness. The time-averaged film Nusselt number was observed to first decrease with the frequency at lower frequencies and then increased with frequency at higher frequencies.

2.8 Knowledge Gap

From the review of the literature presented here, it is evident that the hydrodynamics and heat transfer in slug flow regime having Taylor bubbles in gas-liquid flow in microchannels have been studied extensively. Increased mixing in the liquid phase and high shear stress on the channel wall in the slug flow regime have made it a preferred flow regime to operate in several applications. The enhanced mixing in the liquid phase is caused by the segmentation of the flow and the high wall shear stress occur at the nose and tail of the bubble.

TH-2207_146107023

The effect of bubble volume, especially at low bubble volume (R_{eqv} ~1 or less) on the wall shear stress and heat transfer has not been explored, though it is known that the bubbles of lower volume move with a higher velocity than the long Taylor bubbles. It is important to understand this effect as it is desired to use minimum amount of gas in the applications where it is used only for segmentation of enhancement in wall shear stress.

In experimental systems, the volume of the bubbles generated can be over a range until great care is taken to generate monodisperse bubbles. Therefore, many micro-structured devices can have variation in the bubble volume over a certain range and therefore it is important to understand their interaction which has remained relatively unexplored till date.

Almost every micro-structured device has variation in channel dimension at the inlet and outlet of the main channel, connections and fittings. Therefore, it is important to understand the bubble dynamics at the channel contraction and expansion.

Finally, the two-phase in microchannels is prone to instabilities which may be caused by non-uniform flow distribution in a parallel channel system, pressure drop oscillations or flow boiling. Moreover, some applications such as heat pipes employ oscillatory flow for heat transfer enhancement. There are only a few studies on the effect of oscillations on flow and heat transfer in Taylor flow in microchannels and further investigations are needed to develop a better understanding.

This thesis addresses these knowledge gaps by investigating two-phase slug flow in microchannels over a range of conditions as outlined in the objectives in Chapter 1.

TH-2207_146107023

Chapter 3
Mathematical Framework

TH-2207_146107023

CHAPTER 3

Mathematical Framework

In this chapter, a mathematical framework to model the flow of channel-size bubbles is presented. The assumptions, governing equations and boundary conditions for the volume of fluid (VOF) method are discussed.

3.1 Introduction

A number of approaches, such as the Eulerian-Eulerian approach, the Eulerian-Lagrangian and the single-fluid formulation are used to model multiphase flows. The modelling of a multiphase flow problem depends on the flow characteristics, length-scales, etc. For the Taylor flow modelling, the interface can be explicitly captured. There are various method for Taylor flow modelling such as

(i) Boundary Integral Method

(ii) Finite Element Methods

(iii) Interface Capturing Methods

  (a) Volume-of-Fluid (VOF) Method

  (b) Level-Set Method

  (c) Phase Field Method

  (d) Marker Points Method

(iv) Lattice Boltzmann Methods

As the gas-liquid interface is large in the slug or Taylor flow regime in microchannels, various interface capturing or tracking methods such as Volume of Fluid (Hirt and Nichols, 1981), Level

TH-2207_146107023

Set (Sussman *et al*. 1994), marker point (Unverdi and Tryggvason, 1992) and phase field (Cahn and Hilliard, 1958) can be used to model the flow. VOF method is chosen to model Taylor flow because of its simple formulation and inherent capability to conserve mass of each phase.

3.2 Governing Equations

In this work, the VOF method as implemented in ANSYS 15 Fluent has been employed to capture the gas-liquid interface. In the VOF method, continuum description of two-phase flow is given by the mass, momentum, and energy conservation equations for each phase along with the appropriate boundary conditions at the interface (Hirt and Nicholas, 1981). The interface capturing/tracking methods generally employ a 'single-fluid formalism' in which only a single set of conservation equations are solved together with an advection equation for a colour or marker function. The marker function has a value of '0' in one and '1' in the other and a value between 0 and 1 in the interface region. For the VOF method, the volume fraction of one of the phases is the marker function (Gupta *et al.*, 2010).

Assumptions:

1. The flow is axisymmetric.
2. The flow is laminar.
3. The flow is incompressible.
4. The properties of the fluids such as density, viscosity, thermal conductivity and specific heat capacity and surface tension are constant.
5. Phase change during heat transfer is neglected.
6. There is no mass transfer between the two phases.

The conservation equations for VOF method can be written as:

TH-2207_146107023

Conservation of mass:

$$\frac{\partial \rho}{\partial t} + \boldsymbol{\nabla}.(\rho \boldsymbol{v}) = 0 \tag{3.1}$$

Conservation of momentum:

$$\frac{\partial \rho \boldsymbol{v}}{\partial t} + \boldsymbol{\nabla}.(\rho \boldsymbol{v} \otimes \boldsymbol{v}) = -\boldsymbol{\nabla} P + \boldsymbol{\nabla}.\left(\mu(\boldsymbol{\nabla} \mathrm{v} + \boldsymbol{\nabla} v^{T})\right) + \rho \boldsymbol{g} + \boldsymbol{F}_{SV} \tag{3.2}$$

Conservation of energy:

$$\frac{\partial (\rho e)}{\partial t} + \boldsymbol{\nabla}.(\rho \boldsymbol{v} h) = \boldsymbol{\nabla}.(k \boldsymbol{\nabla} T) \tag{3.3}$$

An additional equation is solved for the advection of a marker function to identify if a cell has gas phase, liquid phase or a mixture of the two. The marker function is the volume fraction of one of the phases as given by Eq. (3.4).

$$\frac{\partial \alpha}{\partial t} + \boldsymbol{v}.\boldsymbol{\nabla}\alpha = 0 \tag{3.4}$$

The equations (3.1-3.4) represent the conservation equations in phase 1 when α = 1 and in phase 2 when α = 0. For the interface cells in which 0 <α < 1, the volume fraction-weighted average of the properties of the two fluids is used in the conservation equations.

$$\varphi = \varphi_1 \alpha + (1 - \alpha)\varphi_2 \tag{3.5}$$

Where φ represents the bulk properties of the fluid such as density, viscosity, thermal conductivity. The use of the phase volume fraction as the marker function results in the inherent mass conservation of each phase unlike some other interface capturing methods such as level-set method. The conservation equations reduce to those for a single phase for all the cells that do not have interface in them as they have either gas or liquid phase only in them. The kinematic boundary condition requiring continuity of velocity at the interface (in case of no mass transfer between phases) is satisfied as only one velocity field is shared by two phases which is continuous

TH-2207_146107023

everywhere. The dynamic boundary condition at the interface requires the jump in the normal and tangential stresses at the interface to be balanced by the surface tension ($\sigma\kappa$) and Marangoni stresses ($\nabla\sigma$), respectively. Marangoni stresses are caused by the gradient in surface tension and are not considered in this work as surface tension is assumed to be a constant.

The jump in the stresses normal to the interface is modelled using continuum surface model (CSF) (Brackbill *et al.*,1992) which approximates the surface force as a body force in the vicinity of the interface using Dirac delta function ($\delta(\boldsymbol{r}-\boldsymbol{r}_{int})$) as given by Eq. (3.6) :

$$\boldsymbol{F}_{SV} = \kappa\sigma\delta(\boldsymbol{r}-\boldsymbol{r}_{int})\hat{\boldsymbol{n}} \tag{3.6}$$

The Dirac delta function is zero everywhere except at the interface i.e. $\boldsymbol{r}=\boldsymbol{r}_{int}$ where $\boldsymbol{r}$ is the position vector. The surface curvature, κ, is calculated from the local gradients in the surface normal at the interface.

$$\kappa = \nabla.\hat{\boldsymbol{n}} \tag{3.7}$$

The surface normal is obtained from the gradient of the volume fraction.

$$\hat{\boldsymbol{n}} = \frac{\boldsymbol{\nabla}\alpha}{|\boldsymbol{\nabla}\alpha|} \tag{3.8}$$

The surface tension term given by Eq. (3.6) is implemented in the following form in ANSYS Fluent (ANSYS Help, 2015).

$$\boldsymbol{F}_{SV} = \frac{\sigma\rho\kappa\boldsymbol{\nabla}\alpha}{\frac{1}{2}(\rho_L+\rho_G)} \tag{3.9}$$

3.3 Modelling Approaches for Slug Flow

TH-2207_146107023

Slug flow in microchannels is periodic in time in the laboratory frame of reference i.e. at a particular cross section in the channel, the flow repeats itself after a certain time. The frequency is equal to the ratio of the bubble velocity to the distance between the nose (or any two corresponding points) of two adjacent bubbles i.e. $f = U_B/L_{UC}$. The flow is also periodic in space i.e. at any time instant, the flow is observed to repeat after a certain distance. This distance is again equal to that between two corresponding points on a bubble and can be termed as unit cell length (L_{UC}). To understand the flow and heat transfer in the periodic flow, the flow is required to be simulated in a long enough domain so that the flow is independent of entrance and exit effects. Alternatively, the flow can be modelled in a periodic unit cell employing periodic boundary conditions on the domain boundaries by modelling the flow in the bubble frame of reference. Both of these approaches have been employed by researchers to study periodic slug flow. In this work, the flow is modelled in a periodic unit cell for all the cases except for the flow of bubble in channels with sudden change in diameter as the flow is not periodic in such a case. In this section both the approaches have been discussed briefly.

3.3.1 Laboratory Frame of Reference

Modelling the flow in the laboratory frame of reference is conceptually simple and easy to implement. The two phases enter the computational domain and the bubbles are generated periodically. As the bubbles travel downstream, their shape evolve and eventually they attain a steady shape and velocity. Thus, a certain development length is required for the flow to become fully periodic. As the slug flow has a train of bubbles, few bubbles are needed to be generated for it to achieve the periodic flow in the following bubbles. Therefore, this technique requires a long computational domain and long computational time as a number of bubbles are required to be generated. This technique has been employed by several researchers to model slug flow e.g. Gupta

TH-2207_146107023

et al., (2009, 2010), Asadolahi *et al.* (2011). Gas and liquid flow rates or superficial velocities or two-phase velocity (U_{TP}) and homogeneous void fraction (β) are the only inputs required in this technique and bubbles are generated.

3.3.2 Moving Frame of Reference

In the bubble frame of reference the flow becomes steady and is periodic in space. Therefore, fully-developed Taylor flow can be studied in a periodic unit consisting of a gas bubble and a liquid slug. Note that the fully-developed Taylor flow refers to the flow that has become fully periodic i.e.

$$\boldsymbol{v}(x,t) = \boldsymbol{v}(x + L_{UC}, t) \tag{3.10}$$

and fully-developed heat transfer for constant wall heat flux boundary condition refers to

$$\frac{T_W(x,t) - T(x,t)}{T_W(x,t) - T_m(x,t)} = \frac{T_W(x + L_{UC}, t) - T(x + L_{UC}, t)}{T_W(x + L_{UC}, t) - T_m(x + L_{UC}, t)} \tag{3.11}$$

Where T_W and T_m are the wall and mean fluid temperatures at location x and time t and L_{UC} is the length of the periodic unit. Asadolahi *et al.* (2011) developed a methodology to model periodic flow and heat transfer in gas-liquid Taylor flow in a periodic unit cell in a frame of reference moving with the bubble. This methodology has been extensively validated by comparison with the experimental data for bubble shape, bubble velocity, film thickness and overall Nusselt number for heat transfer without phase change for flow of long Taylor bubbles in microchannels (Asadolahi *et al.*, 2012; Gupta *et al*., 2013). The same methodology has been adopted in this work.

3.4 Boundary Conditions

Inlet and Outlet: At the domain inlet, the two velocity components, axial and radial, are specified. When the flow is periodic, the axial and radial velocity components from the outlet boundary are

TH-2207_146107023

specified at the corresponding locations at each time step using a user subroutine. At the first time step and while restarting the simulation at an intermediate time, a parabolic velocity profile having average velocity equal to the two-phase velocity is specified at the inlet for first few initial time steps as there is no data available to be specified at the inlet initially. At the exit boundary, a uniform pressure boundary condition having a zero pressure (gauge) is specified.

As only the liquid phase remains present at the channel walls, volume fraction of gas is specified to be zero at the inlet and outlet boundaries.

The fluid temperature increases along the axial direction and the increase in temperature over a periodic unit cell is a constant in the thermally fully-developed flow for the constant wall heat flux boundary condition. Considering energy balance over a unit cell, Asadolahi et al. (2011) showed that the temperature rise over a unit cell can be given by Eq. (3.12).

$$T(x + L_{UC}, t) - T(x, t) = \frac{q_w A_{w,UC}}{\left[(U_{TP} - \varepsilon_G U_B)\rho_L c_{p,L} + \varepsilon_G U_B \rho_G c_{p,G}\right] A_{CS}} \tag{3.12}$$

The liquid in the slug recirculates in the bubble frame of reference and the axial velocity is given by the difference between the fluid velocity in the laboratory frame of reference and the bubble velocity. Thus the fluid enters and comes out of the computational domain at the inlet as well as exit boundaries. This fact needs to be taken into account for the implementation of the periodic boundary condition for temperature. Therefore, the temperature is specified on those cells at the inlet and exit boundaries for which the fluid enters in the computational domain using Eq. (3.12), as shown in Fig. 3.1.

TH-2207_146107023

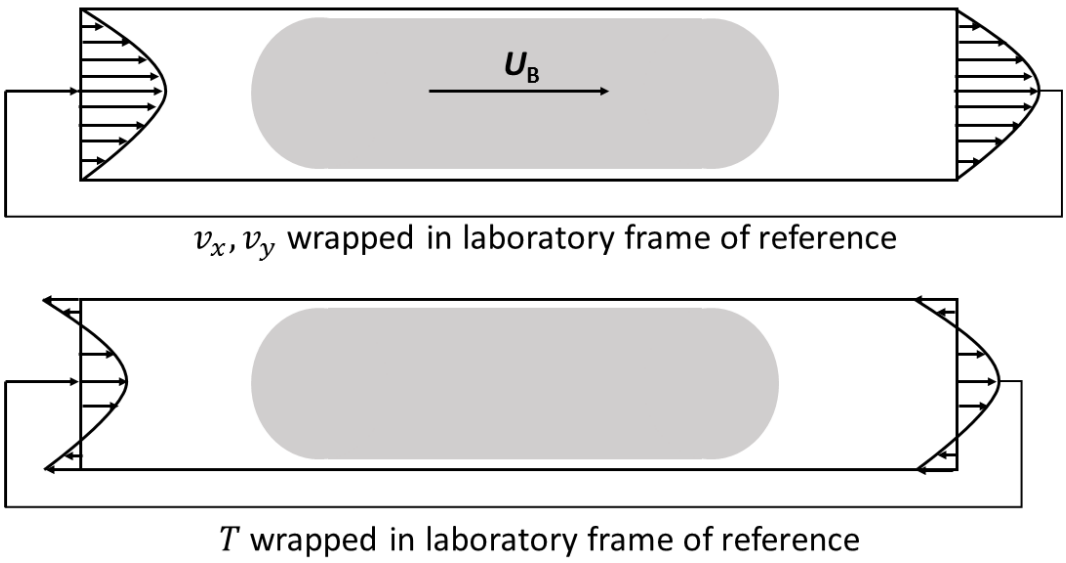

Figure 3.1: A schematic of the computational set up

Wall: A no-slip boundary condition is specified at the channel wall. It might be noted that a liquid phase is always present during the simulations and therefore no three phase contact occurs at any time. For heat transfer studies, a constant heat flux boundary condition is specified on the channel wall and the value of constant wall heat flux 32000 W m^{-2} is used throughout the simulation.

Axis: For the axisymmetric calculations, the governing equations are solved in the cylindrical coordinate system. While no boundary condition need to be specified at the axis boundary, the formulation in ANSYS Fluent requires the axis boundary to lie at r = 0 line only. It can be noted that the cell value in the adjacent cell is used to determine the physical value of a particular variable on the axis.

3.5 Initial Conditions

Pressure: The initial pressure in the domain is specified to be zero (gauge pressure).

TH-2207_146107023

Velocity: The velocity profile in the domain is defined to be parabolic in the entire computational domain initially with the average velocity being equal to two-phase velocity.

Volume fraction: Based on the gas hold-up, the gas volume fraction is specified such that the gas bubble is located in the centre of the computational domain. The bubble volume is gas hold-up times the volume of the computational domain. The initial bubble shape was specified to be cylindrical which appears as rectangle in axisymmetric computations.

Temperature: The initial temperature in the domain is specified to be 300K.

The simulations are run in transient manner. The simulation is therefore run until a steady Nusselt number is obtained. Simulations for heat transfer are initialised once a steady flow solution is obtained. The initial temperature in the domain is specified to be 300 K.

TH-2207_146107023

Chapter 4

Hydrodynamics of Slug Flow: Effect of Parameters

TH-2207_146107023

CHAPTER 4

Hydrodynamics of Slug Flow: Effect of Parameters

This chapter presents a CFD methodology to model the hydrodynamics of periodic slug flow. The results obtained are validated by comparison with the experimental data published in the literature, analytical and empirical correlations and other computational studies, wherever possible. The transition in the bubble shape from spherical to that of Taylor bubble with an increase in the bubble volume is studied. Further, the effect of Reynolds number and capillary number on the hydrodynamics are investigated. Finally, a phenomenological model is presented for shear stress on the channel wall.

4.1 Introduction

A number of parameters such as bubble and slug volumes (or lengths), two-phase velocity, liquid propoerties can affect the hydrodynamics and heat transfer in the slug flow regime. In non-dimensional terms, the changes in two-phase velocity and liquid properties can be represented by Reynolds and capillary numbers. As for the bubble and slug volumes, both the volumes of the gas bubble and liquid slug and their ratio is important. The ratio of gas volume and the unit cell volumes can be represented by the gas hold-up or void fraction in a unit cell. The bubble volume is represented by the equivalent sphere radius and slug length can be non-dimensionalised by the channel diameter. In this chapter, the effect of all of these parameters on the hydrodynamics of slug flow has been investigated.

TH-2207_146107023

4.2 CFD Methodology

As the gas-liquid interface is large in the slug or Taylor flow regime in microchannels, various interface capturing or tracking methods such as Volume of Fluid (Hirt and Nichols, 1981), Level Set (Sussman *et al*. 1994), Marker point (Unverdi and Tryggvason, 1992) and phase field (Cahn and Hilliard, 1958) can be used to model the flow. In this work, the Volume of Fluid (VOF) method as implemented in ANSYS Fluent has been employed to capture the gas-liquid interface. Gas and liquid both phases are assumed to be incompressible. The fluids are assumed to follow Newtonian behavior. As the channel cross section is circular and the bubble shape is axisymmetric at Reynolds number below ~1000 (Asadolahi *et al.*, 2012), the flow can be assumed to be axisymmetric. Axisymmetric flow often refers to considering the governing equations in a cylindrical coordinate (r, θ, z) system neglecting the azimuthal velocity components as well as gradients in the azimuthal direction requiring the momentum equations for r and z directions only to be considered.

To model the flow in a frame of reference moving with the bubble, the entire computational domain is moved with the bubble velocity using dynamic mesh feature of ANSYS Fluent. Figure 4.1 shows a schematic of the periodic computational domain to model slug flow. The expected velocity profiles at the domain boundaries in the laboratory and bubble frame of references have also been shown.

Since the bubble velocity is not known a priori, it is calculated from the previous time step using Eq. (4.1). The bubble velocity becomes time-independent once the bubble shape becomes steady.

$$U_B = \frac{\int_x^{x+L_{UC}} \int_0^R \alpha_G u_x 2\pi r dr dx'}{\int_x^{x+L_{UC}} \int_0^R \alpha_G 2\pi r dr dx'} \tag{4.1}$$

TH-2207_146107023

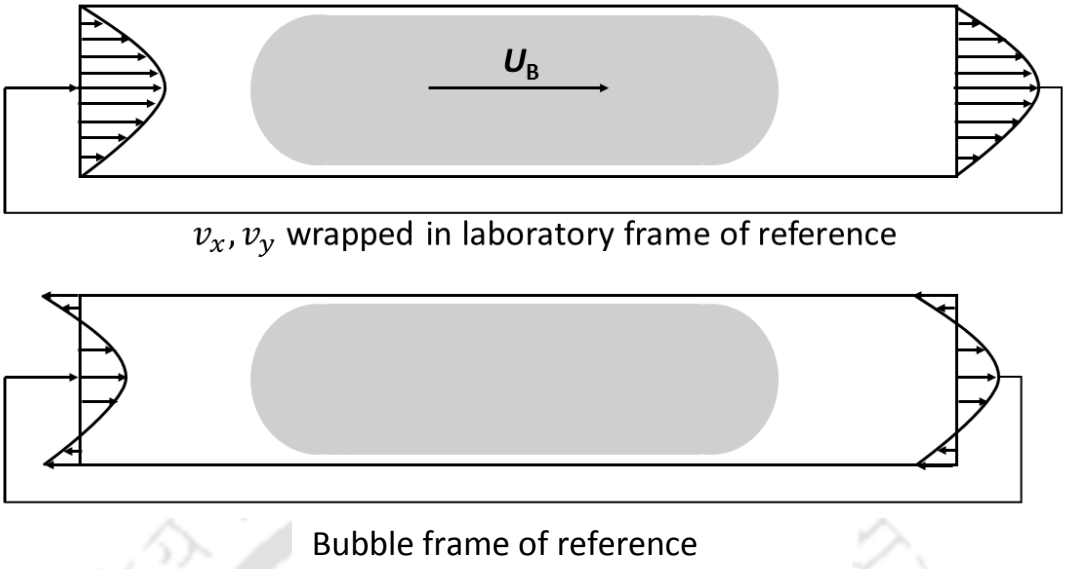

Figure 4.1: A schematic of the computational set up.

As the bubble remains stationary, it is advantageous to keep the bubble in the centre of the computational domain with only liquid phase present at the domain boundaries. This eliminates the need for the implementation of the periodic boundary condition for the phase fraction (α) and only the velocity components. Moreover, the velocity profile in the middle of the liquid slug i.e. at the ends of the periodic domain is nearly parabolic and have almost zero axial gradients. This eliminates the need for the velocity gradients to be wrapped (Rosaguti *et al.*, 2007). Two-phase velocity (U_{TP}) and gas hold-up (ε_G) are the input parameters in this case.

4.2.1 Boundary Conditions

For the velocity, a periodic boundary condition is employed and the velocity components from the exit boundary are specified to the inlet boundary at the corresponding radial location. Initially and for each restart of the simulation, a parabolic velocity profile is defined at the inlet for the first few time steps. At the outlet, a uniform gauge pressure is specified. On the channel wall, a no-slip boundary condition is specified.

TH-2207_146107023

4.2.2 Initial Conditions

The simulations are run in transient manner. However, one should note that the problem is steady in a frame of reference moving with the bubble. The simulation is therefore run until a steady solution is obtained. Initially, the known volume of gas corresponding to the bubble volume is specified as a bubble. The initial bubble shape can be specified either cylindrical or cylindrical with ellipsoidal caps at the two ends. The use of a bubble shape with ellipsoidal caps avoids the singularities that arise at the corner of a cylindrical bubble and approaches to a steady shape faster. In this work, initially the bubble shape has been defined to be cylinder with ellipsoidal ends. For short bubbles, the initial bubble shape can be defined to be spherical. The velocity profile in the domain at time $t = 0$ is defined to be parabolic corresponding to the fully-developed single phase flow having average velocity equal to mixture velocity (U_{TP}). Mixture or two-phase velocity is the sum of the gas and liquid superficial velocities. It can be noted that the average liquid velocity at any cross-section in the slug is equal to the two-phase velocity (U_{TP}) (Suo and Griffith, 1964). The initial (gauge) pressure in the domain is specified to be zero.

4.2.3 Solver Settings

The simulations are performed in a transient manner using a first order explicit time-marching scheme until a steady bubble shape and flow field is obtained. QUICK scheme (Leonard *et al.,* 1990) is used to discretize the convective terms in the momentum equation. An explicit scheme is used to solve the VOF equation and piecewise-linear interface construction scheme is used to keep the interface sharp. A fractional step scheme (Glaz *et al.,* 1993) is used for pressure-velocity coupling. The gradients of scalars are calculated using the Green-Gauss node base method (Rauch *et al.,* 1991) where the values are computed as the mean of values at the nodes of the

TH-2207_146107023

cell. A variable time step with Courant number ($C = v\Delta t/\Delta x$) equaling 0.25 is used. The residuals for velocity and pressure are kept as low as possible (10^{-9} or less). The simulations have been performed employing ANSYS Fluent, a commercial CFD solver.

4.3 Result and Discussion

CFD simulations have been performed in a channel of radius 0.5 mm and unit cell length 5 mm. The simulations have been performed for different gas-liquid systems. Nitrogen has been used as the gas phase in all the simulations. Water and mixture of water and ethylene glycol in different proportions, encompassing a range of viscosities have been used as the liquid phase. The hydrodynamic properties of all the fluids used in the simulations are given in Table 4.1. These values, at room temperature and pressure, have been taken from different literature sources (Leung *et al*., 2014, Gupta *et al*., 2010, Kurimoto et *al.,* 2017), as pointed out in the table. In Table 4.2, the input parameters for the CFD simulations i.e. non-dimensional equivalent sphere radius and two phase velocities for all the cases have been given. The relevant non-dimensional numbers i.e. channel Reynolds numbers, void fractions i.e. gas volume fraction in the unit cell has also been given in Table 4.2. Three cases, as shown in the Table, correspond to the experimental conditions of (Laborie *et al.,* 2005*).*

4.3.1 Mesh Independence Study

A structured, rectangular mesh has been used for the simulations. Gupta *et al.* (2009) suggested the use of mesh elements having aspect ratio close to one in the channel except in the near wall region where the grid should be refined sufficiently in the radial direction to capture the thin liquid film surrounding the bubble. As a guideline, Gupta *et al.* (2009) suggested the use of at

TH-2207_146107023

least five elements in the liquid film region. As the film thickness is not known a priori, an estimate of the film thickness can be made using expression developed by Bretherton (1961).

$$\frac{\delta_F}{R} = 1.34 \left(\frac{\mu U}{\sigma}\right)^{2/3} \quad (4.2)$$

Following these guidelines, the simulations have been performed using different mesh densities for two different bubble volumes: one for the spherical bubble and the other for Taylor bubble as shown in Fig. 4.2.

Table 4.1: Properties of the fluids used in the CFD simulations

Fluid	**Density (kg m^{-3})**	**Dynamic viscosity (kg m^{-1} s^{-1})**	**Surface tension (Nm^{-1})**
Water	997.0	8.90×10^{-4}	0.072
Ethylene glycol (Leung *et al.*, 2014)	1111.4	1.57×10^{-2}	0.048
Glycerol-Water (52 wt %) solution (Kurimoto et *al.*, 2017)	1129.0	5.62×10^{-3}	0.069
Glycerol-Water (64 wt %) solution (Kurimoto et *al.*, 2017)	1164.0	1.16×10^{-2}	0.067
Air	1.185	1.83×10^{-5}	

TH-2207_146107023

Table 4.2: Flow Conditions and non-dimensional numbers

S.No.	Liquid	R_{eqv}	U_{TP} (m s^{-1})	ε_G	Re	Ca
1	Water	0.72	0.3	0.05	336	0.0037
2	Water	0.91	0.1	0.1	112	0.0012
3	Water	0.91	0.2	0.1	224	0.0024
4	Water	0.91	0.3	0.1	336	0.0037
5	Water	0.91	0.4	0.1	448	0.0049
6	Water	0.91	0.5	0.1	560	0.0061
7	Water	0.97	0.3	0.12	336	0.0037
8	Water (Laborie *et al.*, 2005)	0.98	0.64	0.128	717	0.0079
9	Water	1.04	0.3	0.15	336	0.0037
10	Water	1.15	0.3	0.2	336	0.0037
11	Water	1.31	0.2	0.3	224	0.0024
12	Water	1.31	0.3	0.3	336	0.0037
13	Water	1.31	0.4	0.3	448	0.0049
14	Water	1.31	0.5	0.3	560	0.0061
15	Water (Laborie *et al.*, 2005)	1.34	0.5	0.36	561	0.0062
16	Water (Laborie *et al.*, 2005)	1.45	0.58	0.41	649	0.0072
17	Water	1.55	0.3	0.5	336	0.0037
18	Water	1.74	0.3	0.7	336	0.0037
19	Ethylene Glycol	1.31	0.3	0.3	21	0.0981
20	Glycerol-Water (52 wt %)	1.31	0.3	0.3	60	0.0247
21	Glycerol-Water (64 wt %)	1.31	0.3	0.3	30	0.0517

TH-2207_146107023

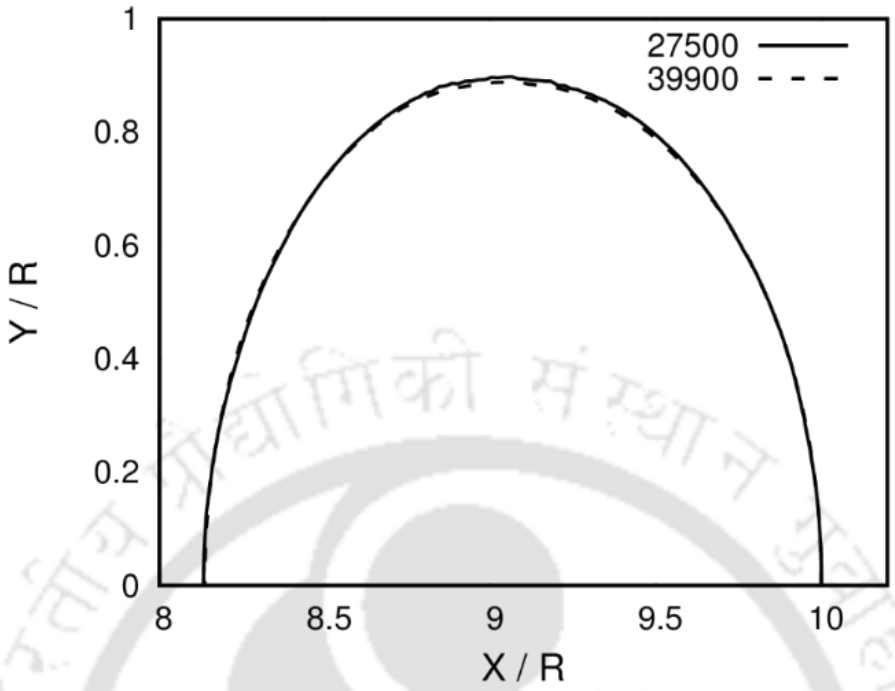

Figure 4.2: Grid independence study for bubble shape for R_{eqv} = 0.91 and Re = 112

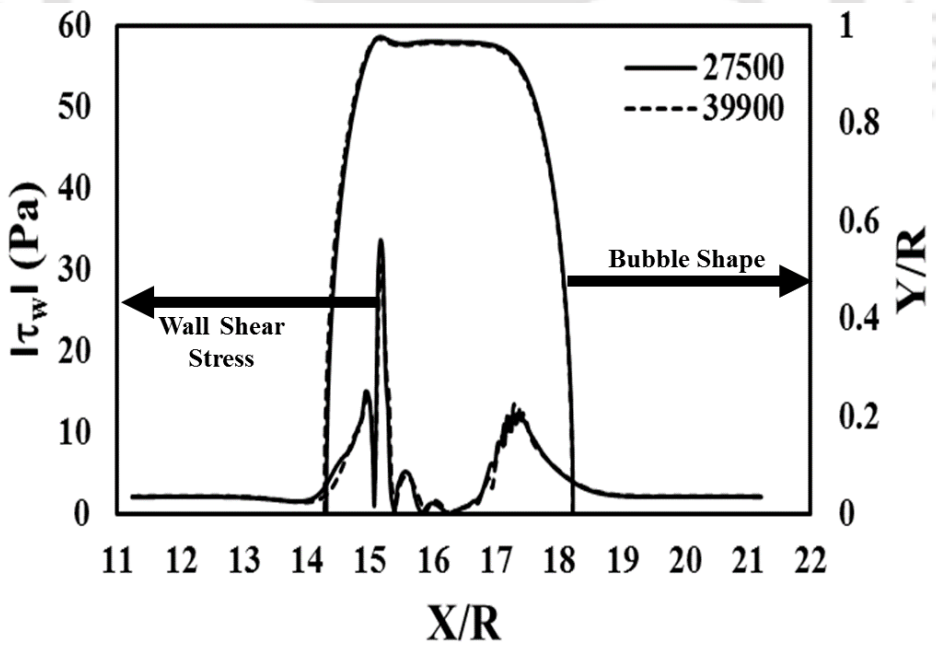

Figure 4.3: Grid independence study for bubble shape and wall shear stress for R_{eqv} = 1.31 and Re = 336.

TH-2207_146107023

For the spherical bubble, two meshes comprising of 27500 and 39900 elements has been used. As can be seen from Fig. 4.2, the bubble shape obtained by the two meshes are same, therefore the mesh containing 27500 elements has been used for further simulations. For the longer bubble, simulations were run for three different meshes consisting of 27500, 39900 and 78750 elements (not shown in the Fig. 4.2) for flow. Figure 4.3 shows a comparison of the bubble shape and wall shear stress obtained from two grids having 27500 and 39900 elements for two-phase velocity of 0.3 m s^{-1} and void fraction of 0.3. Again, the bubble shape obtained from the three meshes are same and mesh consisting of 27500 elements has been used for further simulations.

4.3.2 Validation

The computational methodology developed by Asadolahi *et al.* (2011) for the modelling of Taylor flow has been adopted in this work. The methodology was extensively validated by comparison with the experimental data for the bubble shape and overall Nusselt number by Asadolahi *et al.* (2012) for nitrogen-water and nitrogen-ethylene glycol systems. In this work, validation has been carried out by comparing the bubble shapes for two liquids: (a) a viscous liquid (ethylene glycol) (experiments of Hägnefelt, 2009) (b) low viscosity liquid (water) (experiments of Kurimoto *et al.*, 2017). The bubble shape obtained from CFD simulations for ethylene glycol-nitrogen system has been compared with that obtained by Hägnefelt (2009) in a circular channel of 1.97 mm diameter for a mixture velocity of 0.1 m s^{-1}. For the water-nitrogen system, the bubble shapes are compared with the bubble image obtained experimentally by Kurimoto *et al.* (2017) in a channel of diameter 0.32 mm for a mixture velocity of 0.60 m s^{-1}. Figure 4.4 shows the comparison between the bubble shapes obtained from CFD and experiments for the two cases. It can be seen from the figure that there is good agreement between the bubble shapes obtained from CFD and experiments for both the cases. There is also good agreement between the bubble velocities obtained from CFD and

TH-2207_146107023

experiments for the two cases: for nitrogen-water case the bubble velocities are 0.67 m s^{-1} (CFD) and 0.69 m s^{-1} (experiment) whereas for ethylene glycol-nitrogen case the values are 0.13 m s^{-1} (CFD) and 0.12 m s^{-1} (experiment).

Laborie and Cabassud (2005) reported average magnitudes of shear stress for the liquid slug and gas bubble regions, separately. They also compared the average magnitude of shear stress on the wall in the liquid slug region with that obtained from Hagen-Poiseuille equation (given in Eq. 4.4) and found them to be in good agreement. Our CFD simulations have also shown the wall shear stress in the liquid region to be in good agreement with the Hagen-Poiseuille equation.

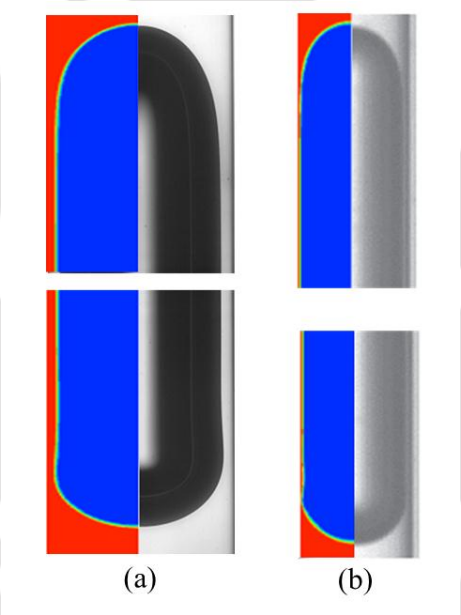

Figure 4.4: Comparison of the bubble shapes obtained from CFD simulations (left, in colour) and experiments (right, in black and white) for (a) ethylene glycol-nitrogen system in a channel of diameter 1.97 mm and a mixture velocity of 0.1 m s^{-1}. Experimental data is from Hägnefelt (2009). (b) water-nitrogen system in a channel of diameter 0.32 mm and a mixture velocity of 0.6 m s^{-1}. Experimental data is from Kurimoto et al. (2017). The red colour represents liquid and blue colour denotes gas phase.

TH-2207_146107023

In Fig. 4.5, the average magnitudes of wall shear stress in the gas bubble region obtained from CFD simulations and experiments of Laborie and Cabassud (2005) have been plotted for cases 1-3 (U_{TP} = 0.50 m s^{-1}, ε_G = 0.360, U_{TP} = 0.58 m s^{-1}, ε_G = 0.410 and U_{TP} = 0.64 m s^{-1}, ε_G = 0.128). The values reported from CFD simulations are those in the constant radius cylindrical region. These values are also in good agreement with each other. It must be noted that for the cases presented in Fig. 4.5, the two-phase velocity is same in CFD and experiments but the bubble lengths are different in the two cases. While the averaging procedure is not clear for the data reported in Laborie and Cabassud (2005), in the case of CFD simulations the shear stress at the bubble nose and tail has not been taken into account to calculate the average wall shear stress in the gas slug region.

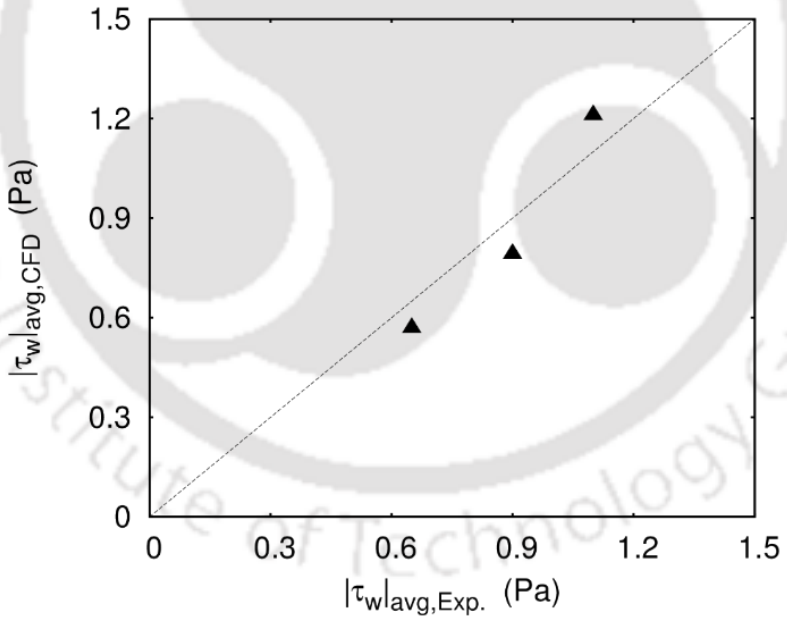

Figure 4.5: Comparison of the average magnitudes of wall shear stress in the gas bubble region obtained from CFD simulations and experiments of Laborie and Cabassud (2005) for cases 1-3 (U_{TP} = 0.50 m s^{-1}, ε_G = 0.360, U_{TP} = 0.58 m s^{-1}, ε_G = 0.410 and U_{TP} = 0.64 m s^{-1}, ε_G = 0.128).

TH-2207_146107023

4.3.3 Typical Flow Field

Figure 4.6 shows the bubble shape and local wall shear stress profile for two-phase velocity of 0.3 m s^{-1} and void fraction of 0.3. In the coloured plot at the top, water is shown in red and air is shown in blue. Note that only half the bubble obtained from axisymmetric CFD simulations is shown. The graph at the bottom shows the bubble interface (isosurface of volume fraction 0.5) together with the local shear stress distribution. The flow direction is from left to right. As the X and Y scales are not same in the graph, the aspect ratio of the bubble is not the same as in the coloured plot above. At the bubble front, bubble radius increases rapidly first and then reaches a plateau while approaching the constant radius cylindrical region. The thickness of the liquid film surrounding the bubble in the cylindrical region is 17 microns. The thickness of the liquid film obtained from well-known equations for calculating film thickness Bretherton expression $\delta_F/R = 1.34Ca^{2/3}$ (Bretherton, 1961) and A&Q correlation $\delta_F/R = 1.34Ca^{2/3}/\left(1 + 3.34Ca^{2/3}\right)$ (Aussillous and Quèrè, 2000) are 16 and 15 microns, respectively. Thus, the film thickness obtained from CFD simulations is in good agreement with that obtained from the correlations available in the literature. Some undulations i.e. oscillatory profile is observed at the back of the bubble. These undulations have been reported in the literature (see for example Giavedoni and Saita, 1999). In his classic paper, Bretherton (1961) obtained analytical solution for the bubble shape at low capillary numbers and his analytical solution showed the presence of undulations at the back of the bubble.

The wall shear stress is defined as

$$\tau_W = -\mu \frac{du}{dr}\Big|_{Wall} \tag{4.3}$$

TH-2207_146107023

The wall shear stress is positive when the flow near the wall is in the forward direction and negative when there is backflow near the wall. The shear stress is always positive in the liquid slug region and almost constant for the case shown in Fig. 4.6(a). Near the bubble nose and tail, the shear stress is observed to increase gradually from the liquid slug to bubble region and a maximum is observed as the cylindrical region having constant film thickness begins. Similarly, at the tail of the bubble the shear stress increases on moving from slug region to the bubble region and reaches a maximum just before the liquid film thickness is minimum. Further moving in the liquid film, a pair of minimum and maximum in the shear stress having negative and positive values respectively are observed. This behaviour corresponds to the recirculating flow near the wall as shown in Fig. 4.6(b). There are two recirculations in the film in this case. The bigger one is in the region where the film thickness is minimum and the other at the start of the constant thickness film region.

This suggests that the introduction of the Taylor bubbles improves the capability of the flow to remove the scale deposited on the walls and can be used in membrane fouling removal applications (Laborie *et al.*, 2005). The change in the sign of shear stress at the tail of the bubble further helps in scale removal. The magnitude of wall shear stress averaged over a unit cell is 3.9 Pa. The wall shear stress for the liquid-only, laminar, fully-developed flow having same average velocity as the mixture velocity can be calculated from Hagen-Poiseuille law (Bird *et al.,* 1961) as given in Eq. (4.4) below:

$$\tau_{w,LO} = \frac{8\mu U_{TP}}{d} \tag{4.4}$$

The liquid-only wall shear stress obtained from Eq. (4.4) is 2.14 Pa. The wall shear stress in the liquid slug region obtained from CFD simulations is 2.14 Pa and is same as the liquid-only value

TH-2207_146107023

given by Eq. (4.4). Clearly, the presence of the bubbles in the flow causes the average shear stress on the wall to almost double. Also note that the maximum and minimum values of wall shear stresses vary between 12.4 and -34.2 Pa – one order of magnitude higher than the average value. These values occur at the locations of minimum and maximum film thickness.

In Fig. 4.6(c), the pressure on the channel wall and axis has been shown. The two sudden jumps in the axis pressure correspond to the bubble front and back and can be attributed to the Laplace pressure difference caused by surface tension. A clear reverse pressure gradient is observed at the axis i.e. in the gas bubble. The wall and axis pressures are same in the liquid slug region, however, in the gas bubble region, the axis (gas) pressure is more than that on the wall (liquid). The pressure in the liquid film (wall) balances the pressure loss caused by the viscous force, change in Laplace pressure caused by change in bubble curvature and accelerational pressure drop, if any. The pressure change at the bubble front can be attributed to the change in bubble curvature from ~$(2/(R-\delta_F))$ to ~$1/(R-\delta_F)$. In the middle, the pressure is almost constant before it dips at a location that corresponds to the recirculation in the constant thickness film region. The bigger oscillation in the pressure at the bubble back corresponds to the recirculation near the minimum film thickness region shown in Fig. 4.6(b). Recently, Abiev (2017) has analysed the bubble shape at the ends and the associated velocity, shear stress and pressure field with simple phenomenological modeling and showed that the reverse flow in the film is caused by the inverse pressure gradient in the film.

TH-2207_146107023

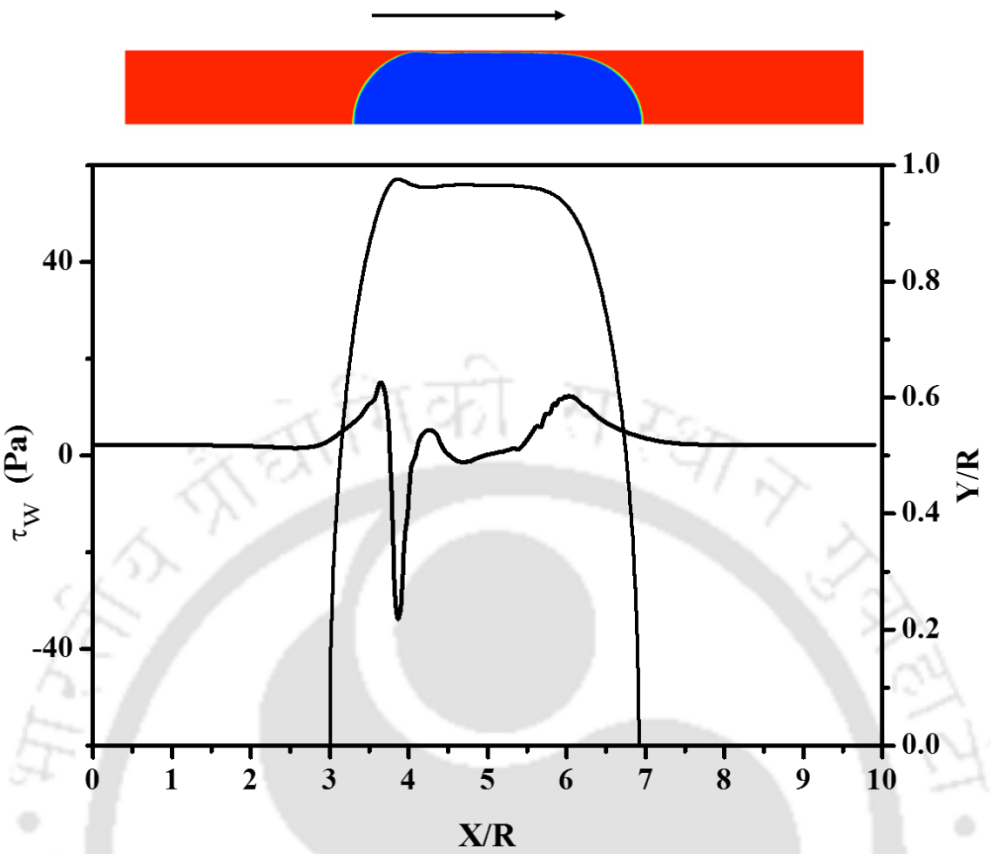

(a)

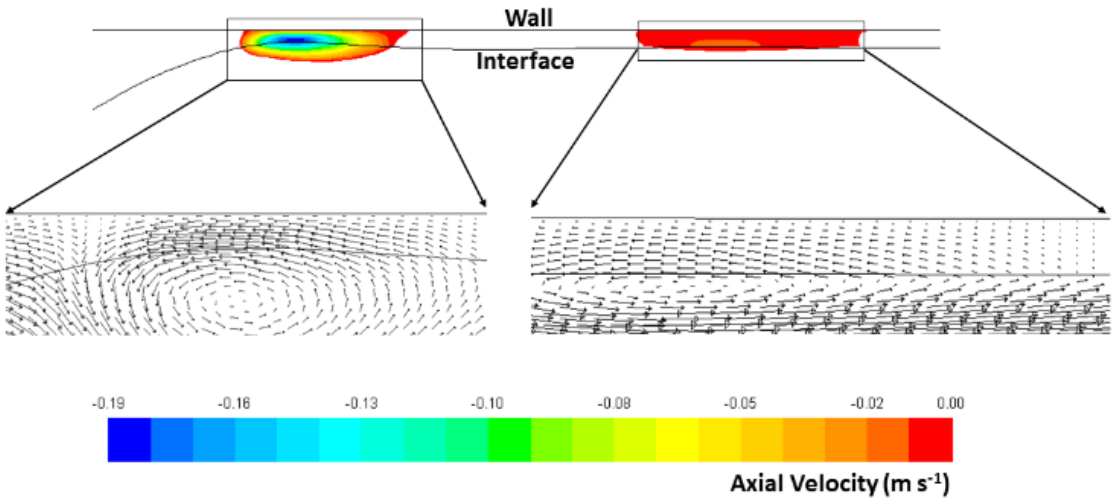

(b)

TH-2207_146107023

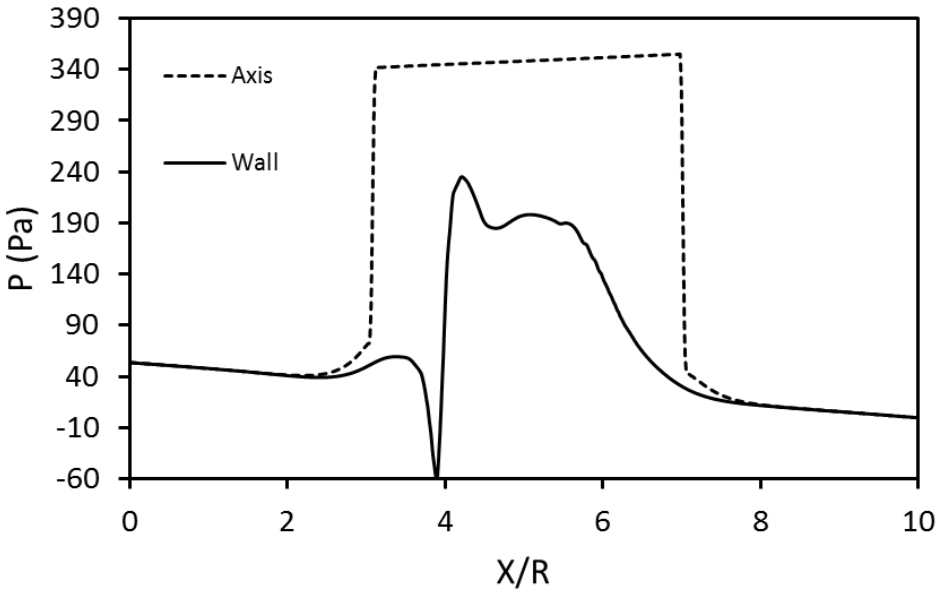

(c)

Figure 4.6: (a) Bubble shape and local wall shear stress profile (b) velocity field in the film near the wall for two-phase velocity of 0.3 m s^{-1} and equivalent sphere radius of 1.31 for air-water flow having Ca = 0.0037 and Re = 336. (c) Pressure profile along the axial direction on the channel wall and axis. The colour contour in (b) shows the regions of negative axial velocity in the film.

4.3.4 Effect of Bubble Volume

Bubble Shape: CFD simulations have been performed for a range of bubble volumes ($0.72 \leq R_{eqv} \leq 1.55$) for *Re* = 336. Figure 4.7 shows the bubble shapes and pressure contours obtained from CFD simulations for all the cases. As the computational domain is axisymmetric, only one half of the bubble is shown in the figure. The bubble shape is close to spherical for small bubble volumes ($R_{eqv} \leq 0.97$). For $R_{eqv} = 1.15$, the bubble takes the shape of a Taylor bubble i.e. it has a constant thickness film region between the hemi-spherical / ellipsoidal front and rear. A further increase in the bubble volume results in an increase in the length of the cylindrical region in the

TH-2207_146107023

middle. In their work on liquid drops, Lac and Sherwood (2009) also found that for $R_{eqv} \geq 1.1$ the front and rear of the drop remained unchanged with an increase in the droplet volume and the increase in drop volume merely added to the length of the droplet.

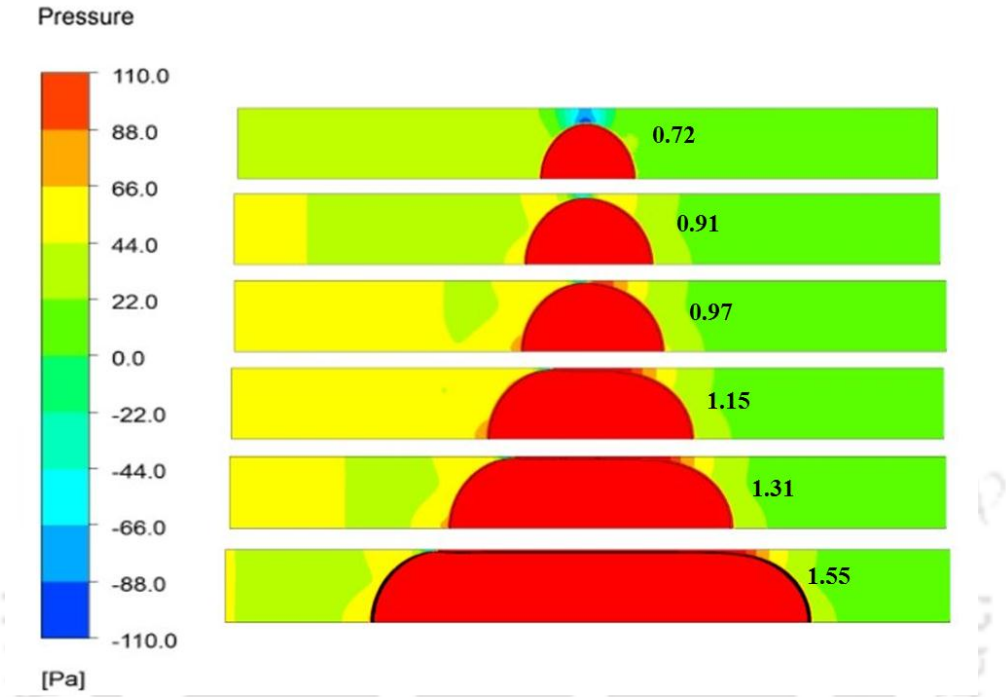

Figure 4.7: Bubble shape (interface shown by solid black line) and pressure field for R_{eqv} = 0.72, 0.91, 0.97, 1.15, 1.31 and 1.55 (value increasing from top to bottom) for Re = 336.

To compare the bubble shapes, the bubble interfaces identified by the isocontours of volume fraction 0.5 are plotted together in Fig. 4.8. In Fig. 4.8(a), the bubble shapes at the front or nose has been compared by plotting the bubble interfaces with the bubble fronts matched. In Fig. 4.8(b) the bubble tails are matched together in order to compare the shape of bubble tail for different bubble volumes. The x and y axes have different scales (i.e. the length of 1 unit on y-axis is not same as that on the x-axis) in Fig. 4.8, therefore actual bubble aspect ratio is not seen in these figures. While the curvatures at the front and back ends of the bubbles are same for all the cases, the bubbles belong to two broad categories. For the three low bubble volumes ($R_{eqv} \leq$

TH-2207_146107023

0.97), the interface radius i.e. the radial distance between the channel axis and interface increases monotonically from front to the middle of the bubble to attain a maxima and then decreases monotonically towards the rear. The shape of these bubbles are same except near the maximum interface radius region in the middle. The maximum radius is a function of the bubble volume. The shape of these short bubbles is almost spherical.

For $R_{eqv} \geq 1.15$, the bubbles have a shape typical of a Taylor bubble: a cylindrical region in the middle and two ellipsoidal halves at the ends. The curvatures at the front and back of the bubbles are same as that for the short bubbles and the bubble interface transitions from a spherical shape at the front to the cylindrical region in the middle. After the cylindrical region, a minima in the interface radius is observed. Further, it increases to a maximum and then decreases monotonically at the back. The occurrence of these undulations at the back of the bubble has been explained by the analytical solution of the linearised Landau-Levich equation by Bretherton (1961) and has recently been explained by Cherukumudi *et al.,* (2015). Cherukumudi *et al.,* (2015) proposed a condition for the minimum length of a Taylor bubble assuming the length of the transition region between the front and back of the bubble to be 10 non-dimensional unit $\left(1 \text{ non} - \text{dimensional unit} = \frac{\delta_F}{R}(3Ca)^{-1/3}\right)$ and is given by Eq. (4.5).

$$\frac{L}{R} \approx 2\left(1 + 10\frac{\delta_F}{R}(3Ca)^{-1/3}\right) = 2 + \frac{18.55Ca^{1/3}}{1+3.34Ca^{2/3}} \tag{4.5}$$

For the present condition the minimum length of a Taylor bubble comes out to be 4.65*R* from Eq. (4.5). As can be seen from Fig. 4.8, the shortest Taylor bubble (R_{eqv} = 1.15) has a length less than 3*R*. However, it should be noted that a constant film thickness region has not developed in this case. For R_{eqv} = 1.31, the bubble length is ~4*R*.

TH-2207_146107023

In Fig. 4.9, the minimum film thickness (δ_{min}), the minimum distance between the bubble interface and channel wall has been shown as a function of R_{eqv}. The minimum film thickness decreases with an increase in the bubble volume for small bubbles. It is important to note that the minimum film thickness remains same for long Taylor bubbles as can be clearly seen in Fig. 4.8(b). The film thickness in the cylindrical region or Taylor bubble film thickness has also been shown for large bubble volumes for comparison.

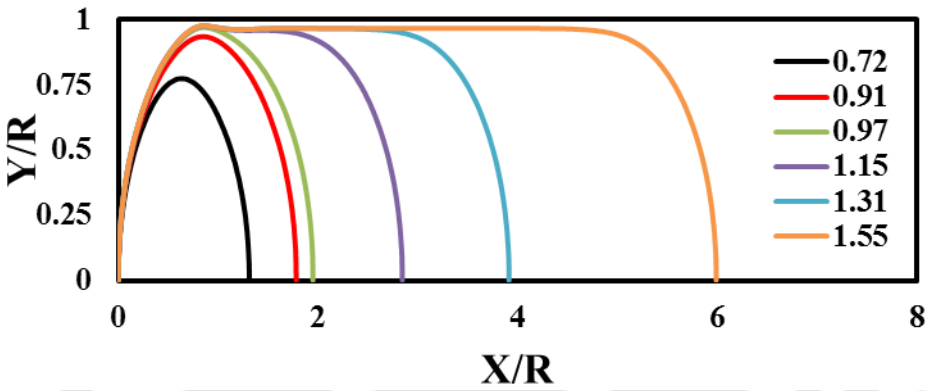

(a)

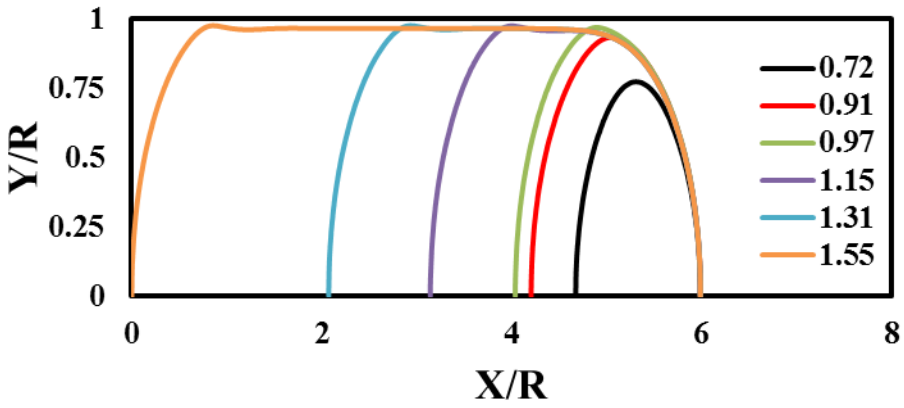

(b)

Figure 4.8: Bubble shapes with bubble (a) rears and (b) fronts matched for Re = 336 and R_{eqv} = 0.72, 0.91, 0.97, 1.15, 1.31 and 1.55 (area under the curve increases with increasing R_{eqv}).

TH-2207_146107023

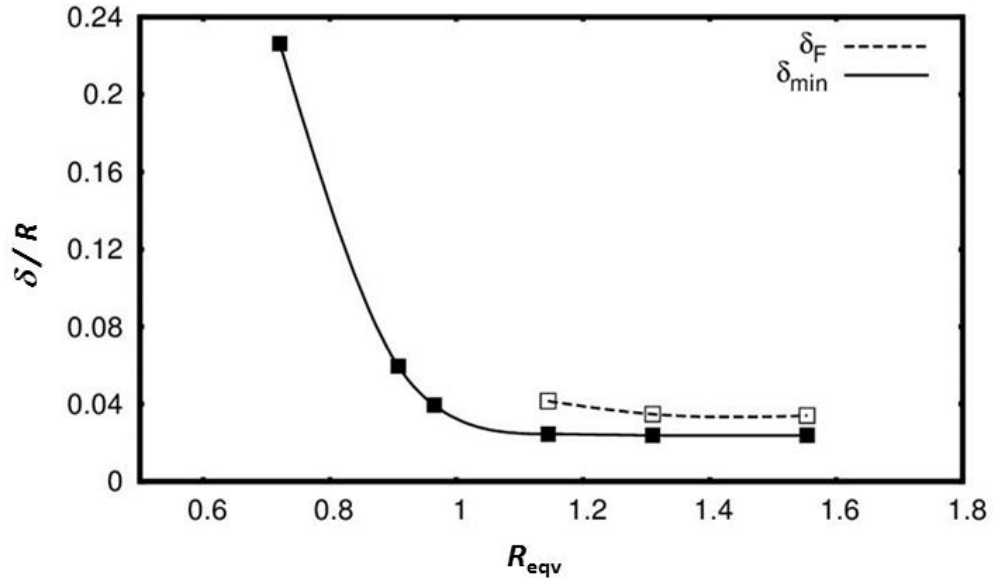

Figure 4.9: Minimum film thickness (δ_{min}) (solid symbols) and Taylor bubble film thickness (δ_F) (open symbols) variation with the bubble size for Re = 336.

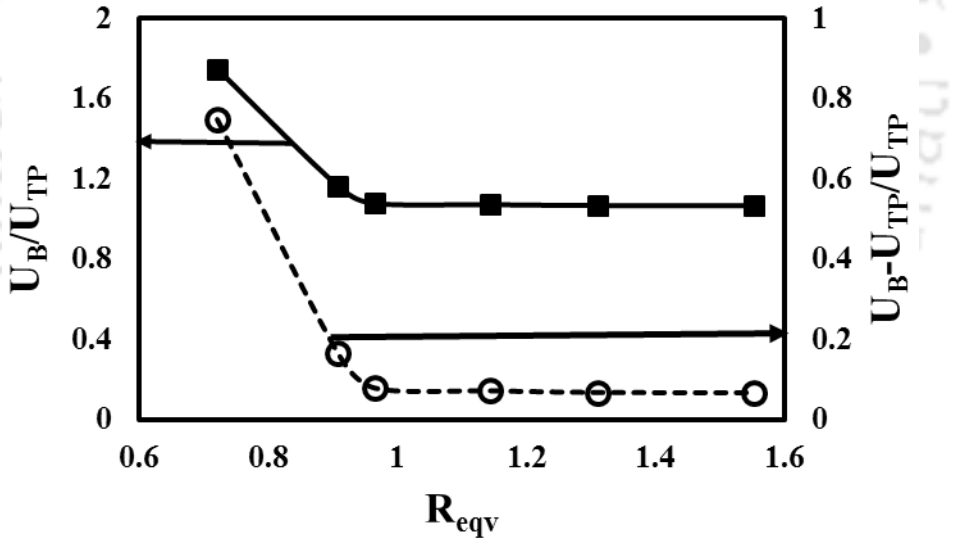

Figure 4.10: Non-dimensional bubble velocity variation with bubble size for Re = 336.

Bubble Velocity: The bubbles moves with a velocity U_B in the forward direction and this velocity is obtained from CFD simulations using Eq. (4.1). Figure 4.10 shows the variation of the bubble velocity with an increase in the bubble volume. The small bubble moves with a high velocity and the bubble velocity decreases with an increase in bubble volume until the bubble assumes the shape

TH-2207_146107023

of a Taylor bubble. Feng (2010) also observed that a bubble of larger size moved at a slower velocity in the range of parameters simulated in this work. The velocity of a Taylor bubble remains unchanged with further increase in bubble volume. Clift *et al*. (1978) also point out that the bubble length has no influence on the bubble velocity when its length exceeds 1.5 times the channel diameter. This result can have implication in a number of applications where a long bubble or droplet is followed by a short bubble for example evaporation and boiling, satellite bubble and droplets. As the velocity of the small spherical bubbles is more than that of the long Taylor bubble, a shorter bubble following a longer bubble will eventually coalesce to form a longer Taylor bubble.

Wall Shear Stress: The wall shear stress has been plotted for different cases along with the bubble shapes in Fig. 4.11. Figure 4.11 the wall shear stress has been plotted for larger bubbles (ε_G = 0.3, 0.5 and 0.7 and R_{eqv} 1.31, 1.55 and 1.74). While the wall shear stress is high in the nose and tail regions, it is very low in the cylindrical region. As with the bubble shapes, the wall shear stress distribution at the nose and tail is also same for all the three cases.

Some interesting observations can be made regarding the shear stress distribution for the three low volume fraction cases shown in Fig. 4.11(b). At ε_G = 0.1, three peaks are observed in the wall shear stress but the magnitude of the shear stress is low. For ε_G = 0.15, again three peaks are observed in the wall shear stress plot, albeit the magnitude of wall shear stress becomes double than that for ε_G = 0.1 case. For ε_G = 0.2, while the wall shear stress distribution at the back of the bubble remains same as that for ε_G = 0.15 case, two peaks appear in the front region.

TH-2207_146107023

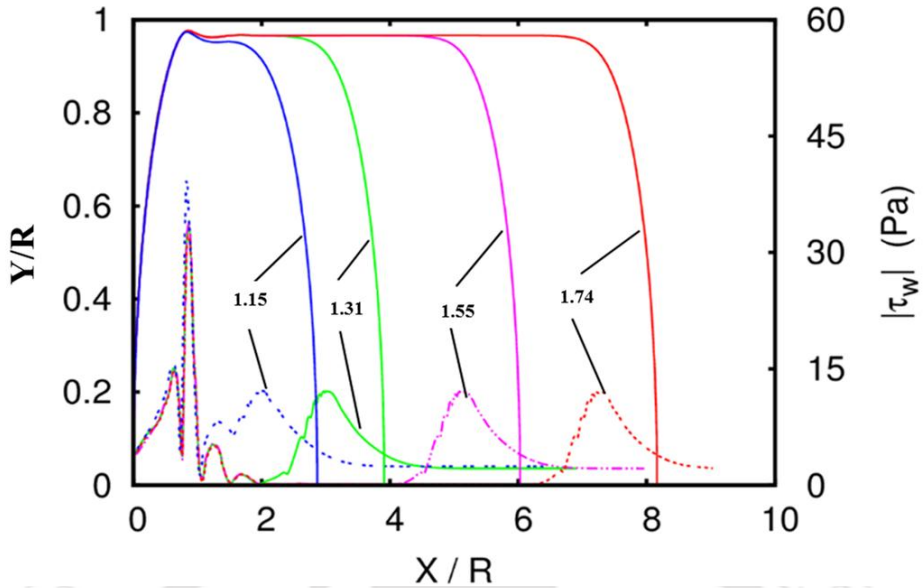

(a)

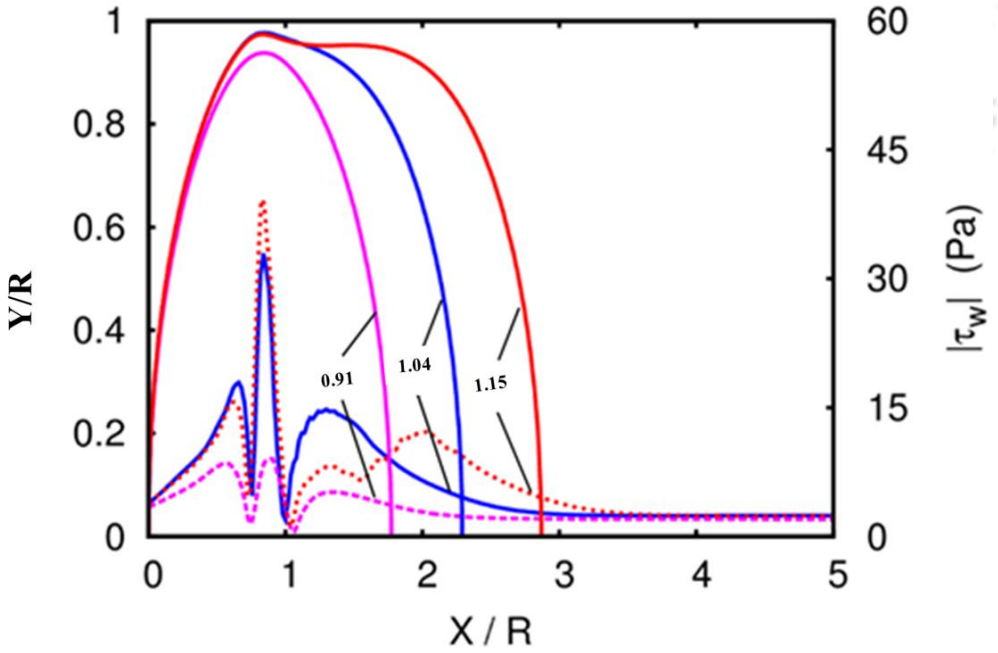

(b)

TH-2207_146107023

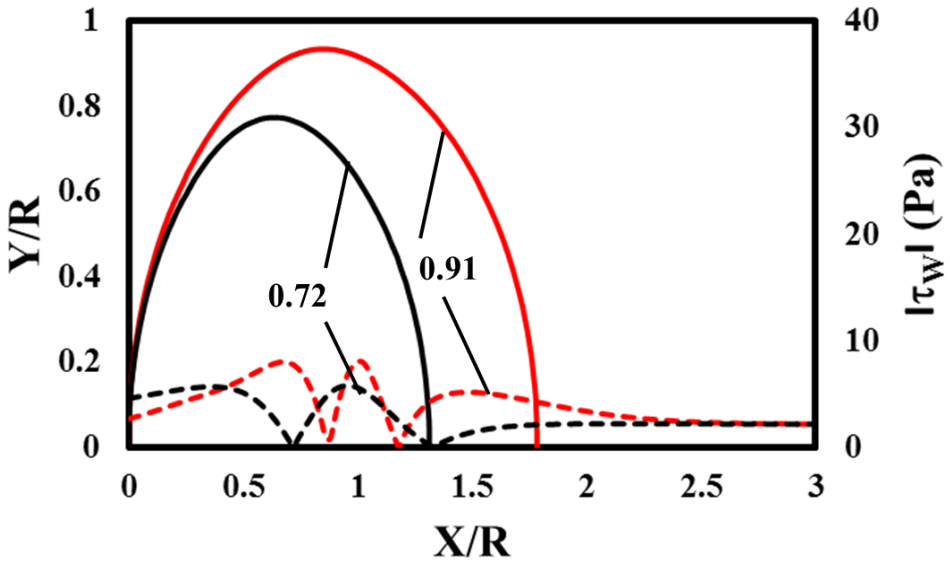

(c)

Figure 4.11: Bubble shapes and magnitude of wall shear stress (on secondary axis) obtained from CFD simulations for a mixture velocity of 0.3 m s^{-1} for air-water flow having Ca = 0.0037 and Re = 336 and void fractions of (a) 1.15, 1.31, 1.55 and 1.74 and (b) 0.91, 1.04 and 1.15 (c) 0.72 and 0.91.

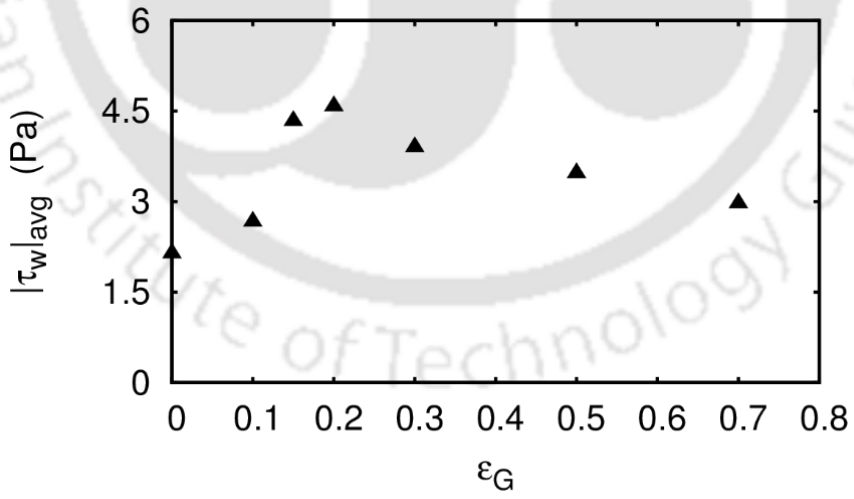

Figure 4.12: Average magnitude of wall shear stress over a unit cell as a function of void fraction for a mixture velocity of 0.3 m s^{-1} for air-water flow having Ca = 0.0037 and Re = 336.

TH-2207_146107023

In Fig. 4.12, the magnitude of wall shear stress averaged over a unit cell has been plotted. The average magnitude of wall shear stress increases when void fraction increase from 0.1 to 0.2 and then decreases with a further increase in the void fraction. This pattern is quite clear when one takes into account the local wall shear stress distribution. At low volume fractions, the wall shear stress at the bubble nose and tail region is higher than that in the liquid slug region and consequently the wall shear stress becomes higher than that for liquid only flow ($\varepsilon_G = 0$). The wall shear stress in the nose and tail region increases with void fraction until the nose and tail regions develop, this explains the increase in wall shear stress until void fraction is less than 0.2. For values of void fraction higher than 0.2, only the length of cylindrical region increases where wall shear stress is very low and therefore the average value of wall shear stress drops at higher void fractions.

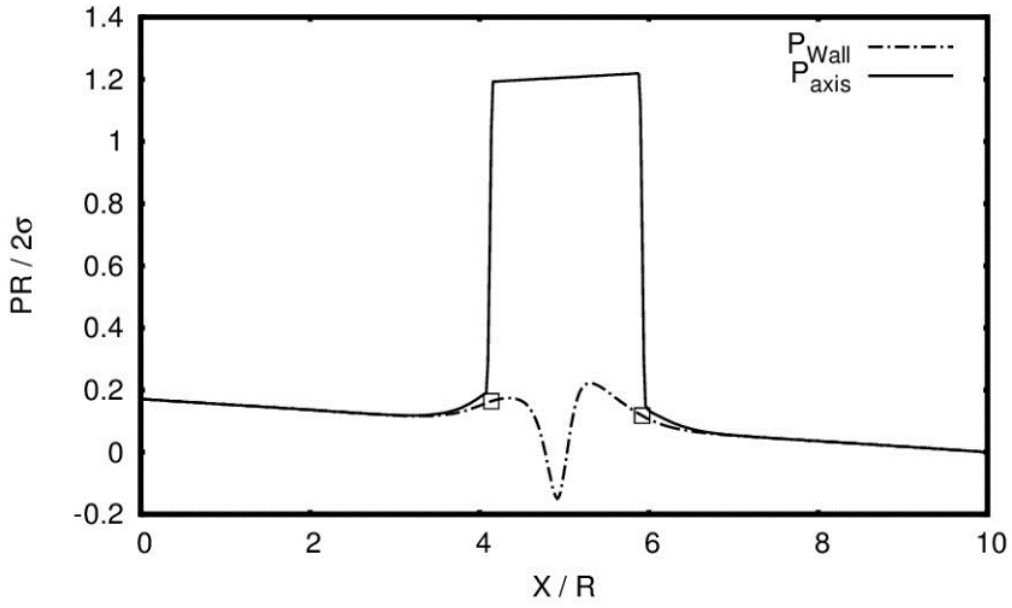

Figure 4.13: Typical wall and axis pressure distribution for Re = 336 and R_{eqv} = 0.91. The square symbols (□) show the start and end of the bubble.

TH-2207_146107023

***Pressure Distribution*:** The pressure contours has been shown in Fig. 4.7. The pressure in the bubble is observed to be almost uniform and the pressure jump at the gas-liquid interface caused due to surface tension (Young-Laplace equation) can be observed. Figure 4.13 shows the typical pressure distribution at the channel axis and channel wall for Re = 336 and R_{eqv} = 0.91. The pressure is non-dimensionalised by the Laplace pressure difference in the plot. Note that the gas bubble lies on the channel axis, whereas there is only liquid phase on the channel wall. The pressure jump on the axis is because of the Laplace pressure difference. The pressure at the back of the bubble is slightly lower than that at the front on the axis.

Figure 4.14 shows the pressure distribution on the channel wall for the four different bubble volumes. In the liquid slug region, the pressure gradient is constant i.e. the pressure varies linearly and is same as that for fully-developed, liquid-only laminar flow. In the bubble region, the wall pressure decreases and reaches a minimum at the location where film thickness is minimum. For R_{eqv} = 0.72, this dip in pressure is almost symmetric. For $R_{eqv} \geq 0.91$, the pressure first increases near the bubble back, then decreases to a minimum and then increases again near the front of the bubble and then decreases again. For R_{eqv} = 1.31, an almost constant pressre region is observed in the middle cylindrical region of the bubble before it starts decreasing near the bubble front.

Along with the bubbles, a part of liquid between two adjacent bubbles i.e. liquid slug also moves with the bubble velocity in the forward direction and remaining liquid is left behind. In addition to the forward motion, the liquid slug and gas bubbles both have internal recirculations which can be best observed in the bubble frame of reference. Figure 4.15 shows the streamlines in the liquid slugs and gas bubbles in a frame of reference moving with the bubble. For $R_{eqv} \geq 0.91$, the liquid in the slug is observed to recirculate covering almost the entire channel.

TH-2207_146107023

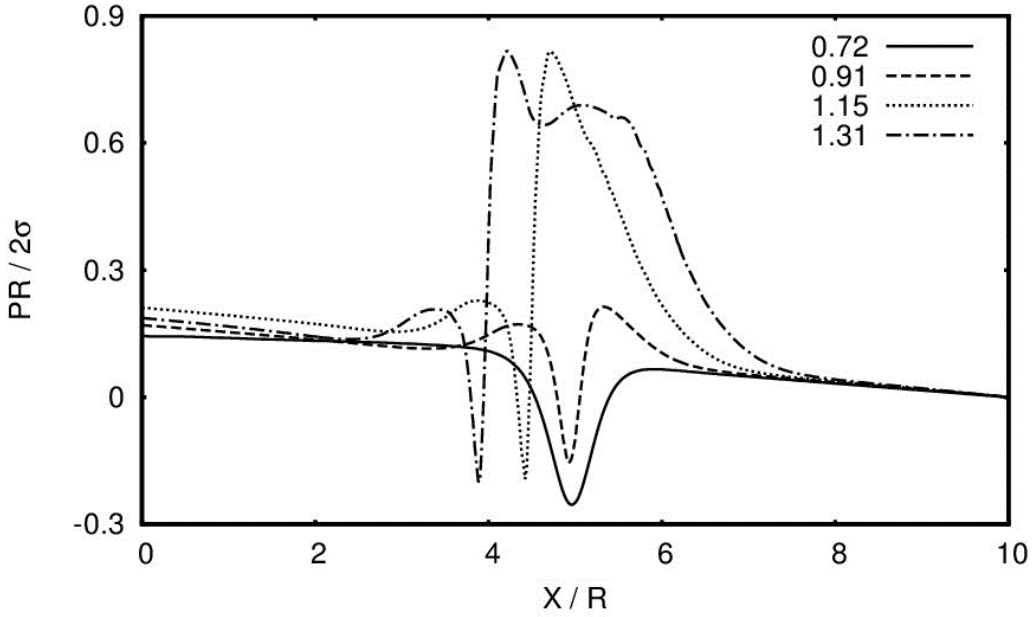

Figure 4.14: Wall pressure variation along the axial direction for four different bubble volumes (R_{eqv} = 0.72, 0.91, 1.15 and 1.31) at a Re = 336.

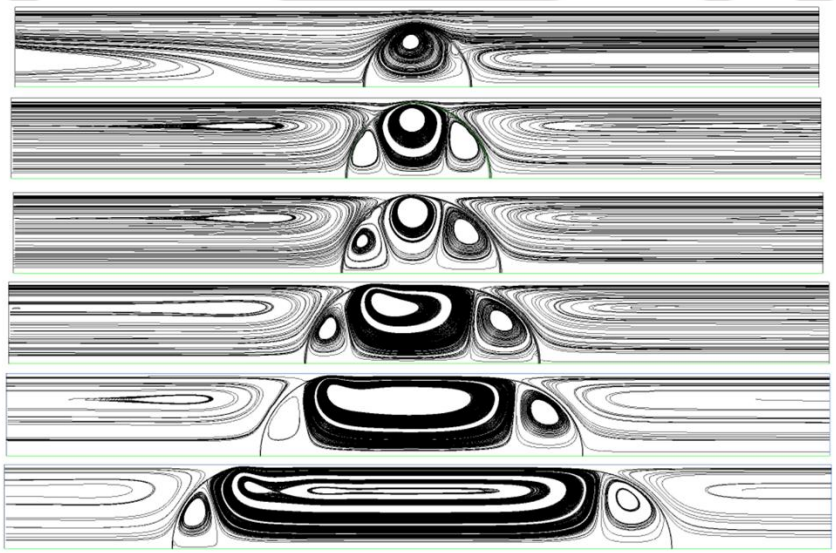

Figure 4.15: Bubble shape (interface shown by dark black line) and streamline for R_{eqv} = 0.72, 0.91, 0.97, 1.15, 1.31 and 1.55 for Re = 336.

TH-2207_146107023

For R_{eqv} = 0.72, the radial extent of recirculation is upto 0.5R from the channel axis and the recirculating liquid returns back well before the liquid can reach the back of the bubble. A big vortex is seen inside the gas bubble. For $R_{eqv} \geq 0.91$, there are three vortices in the bubble. An increase in bubble volume results in an increase in the size of the vortex in the middle whereas the vortices on the sides remain almost same in size. There are two stagnation points on the bubble. At these points, the flow direction reverses inside as well as outside the bubble.

4.3.5 Effect of Reynolds Number

The effect of increase in channel Reynolds number on the hydrodynamics has been studied by increasing the two-phase velocity for near-spherical (R_{eqv} = 0.91) as well as Taylor bubbles (R_{eqv} = 1.31). In Fig. 4.16, the streamlines in a frame of refernce moving with the bubble along with the bubble shape for R_{eqv} = 0.91 has been shown for 112 < Re < 560. While the bubble shape is observed to be spherical at low Reynolds numbers, the bubble can be clearly seen to be composed of two non-spherical halves at higher Reynolds numbers. With an increase in Reynolds number, the front or nose of the bubble becomes sharp i.e. the radius of curvature at the front decreases. Whereas the increase in the Reynolds number causes the back of the bubble to become flatter i.e. radius of curvature at the back increases. A similar effect of the increase in Reynolds number has been observed on the shape of the bubble front and back in Taylor flow in microchannels in literature (Gupta *et al.*, 2010). In their calculations for liquid drops, Lac and Sherwood (2009) also observed the curvature of the drop at the front to be higher than that at the rear. Figure 4.17 shows the variation of minimum film thickness with an increase in Reynolds number for R_{eqv} = 0.91. The minimum film thickness decreases from ~0.1R to ~0.05R with the increase in Reynolds number from 112 to 560.

TH-2207_146107023

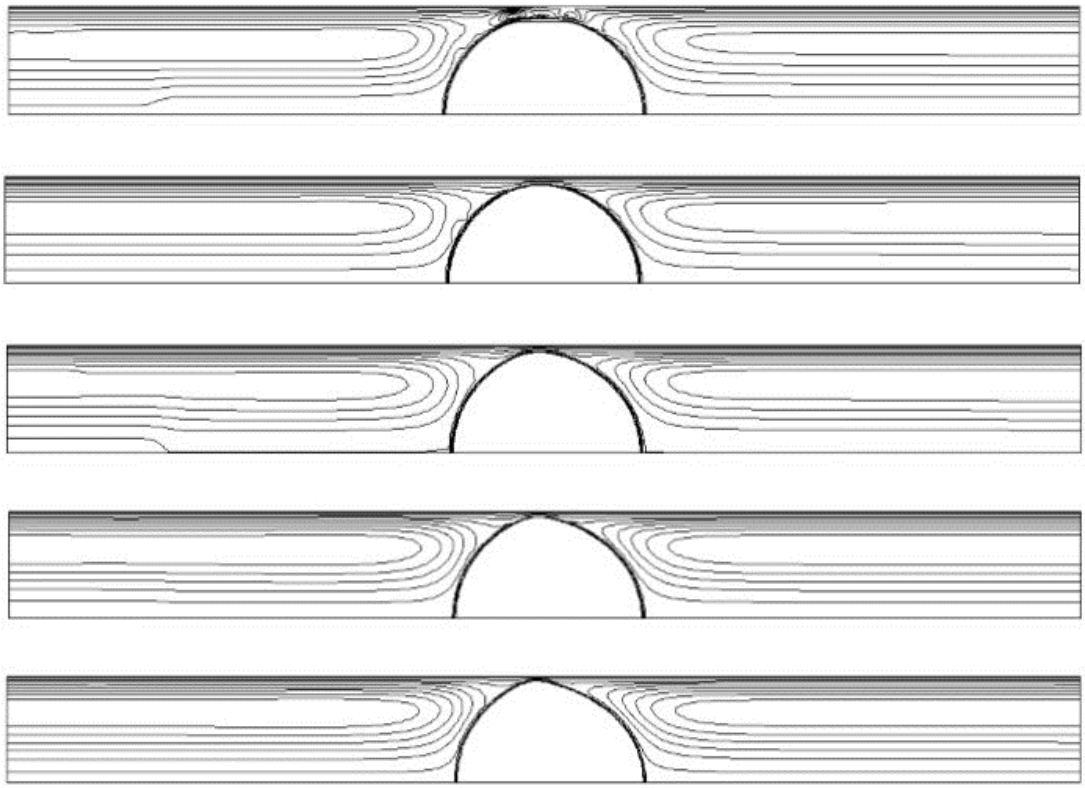

Figure 4.16: Bubble shape and streamlines for R_{eqv} = 0.91 for Re = 112, 224, 336, 448 and 560.

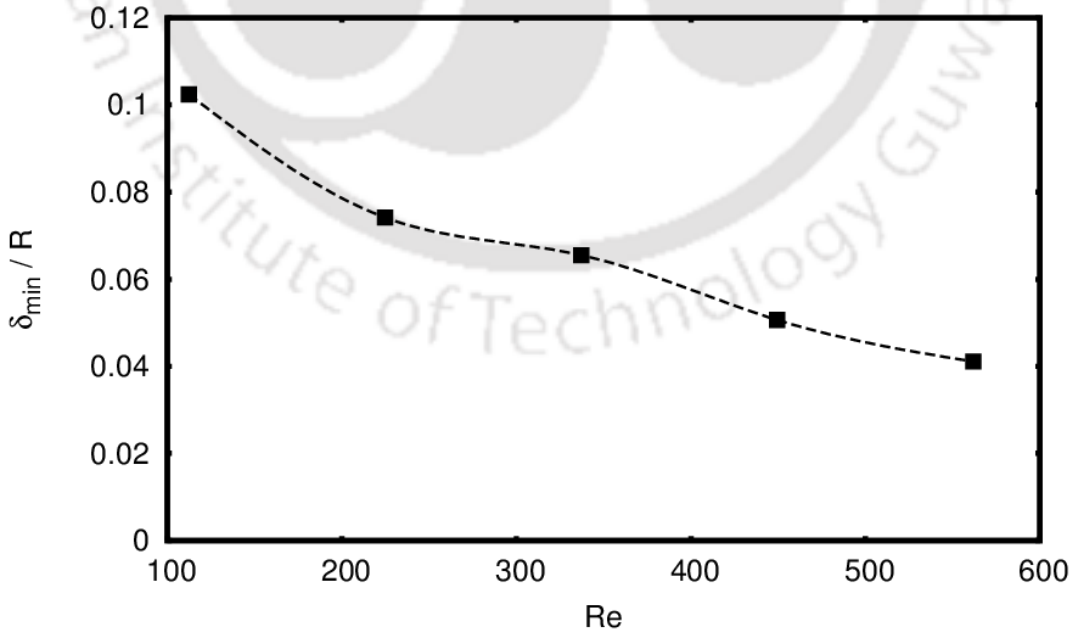

Figure 4.17: Minimum film thickness as a function of Reynolds number for R_{eqv} = 0.91.

TH-2207_146107023

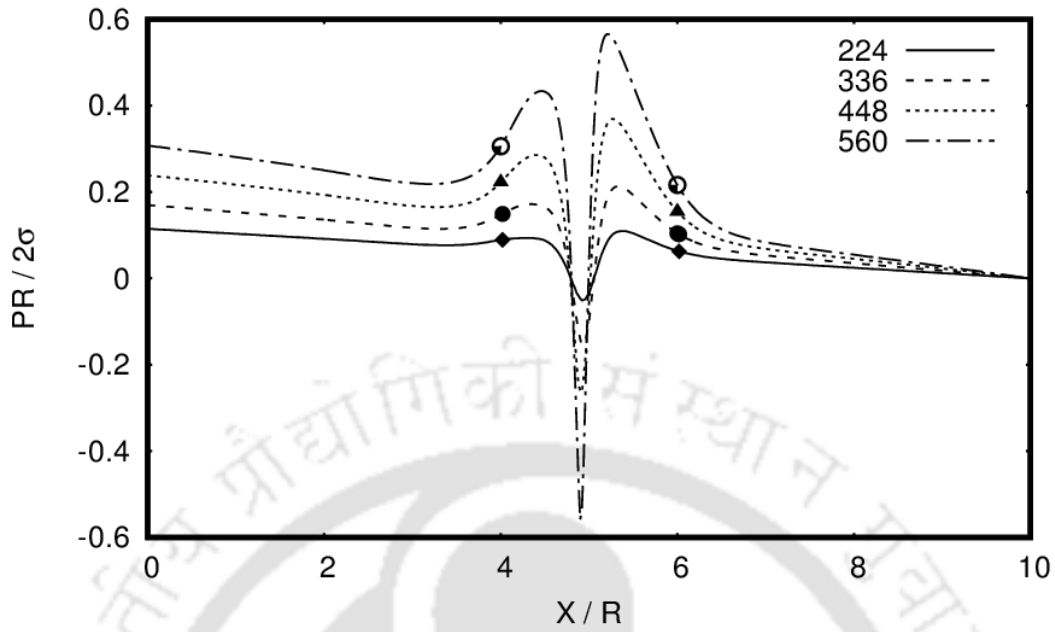

Figure 4.18: Wall Pressure for R_{eqv} = 0.91 and Re = 224-560. The symbols show the start (left) and end (right) of the bubble for each case.

Figure 4.18 shows the pressure on the channel wall for R_{eqv} = 0.91 and Reynolds numbers ranging from 224 to 560. As observed in the earlier section, pressure decreases linearly in the liquid slug region. The slope of the linear portion in the slug region increases with an increase in Reynolds number. This is similar to the laminar, fully-developed, liquid-only flow for which the pressure gradient can be given by Hagen-Poiseuille law i.e. $\frac{\Delta P}{L} = \frac{8\mu U}{R^2}$ and the pressure gradient increases with an increase in the mixture velocity. It can be seen that the dip in the pressure at the middle of the bubble decreases with an increase in Reynolds number. Similarly, the raise in the pressure near the bubble ends also increases with an increase in Reynolds number. This pressure profile also causes recirculation in the liquid film (in laboratory frame of reference) between the bubble and wall.

TH-2207_146107023

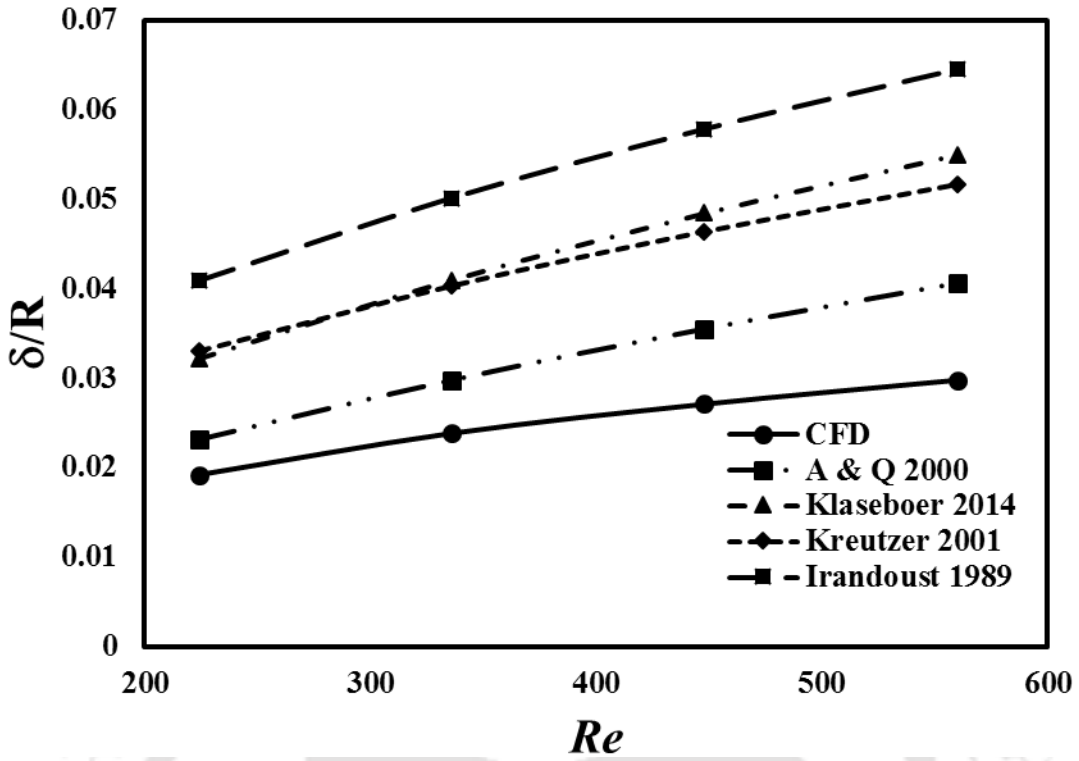

Figure 4.19: Non-dimensional film thickness in the cylidrical region obtained from CFD simulations for R_{eqv} = 1.31. The film thickness obtained from has also been shown.

The effect of increase in inertia on the shape of Taylor bubble has been studied by Edvinsson and Irandoust (1996), Giavedoni and Saita (1997), Heil (2001), Ryck (2002) and Gupta *et al.* (2010) amongst others. The thickness of the liquid film and the length of the transition region at the front increases with an increase in Reynolds number. In Fig. 4.19, the non-dimensional film thickness obtained from CFD simulations as well as the film thickness calculated from other correlations as given in table 2.1 are also plotted. From the figure 4.19 CFD film thickness is comparable with the different correlation given such as A & Q (2000), Klaseboer (2014), Kreutzer (2001) and Irandoust (1989). The film thickness in the cylindrical region increase with an increase in the Reynolds number.

TH-2207_146107023

4.3.6 Effect of Capillary Number

To understand the effect of different liquids, CFD simulations have also been performed for three different liquids, water-glycerol (52% by wt.) mixture, water-glycerol mixture (64% by wt.) and ethylene glycol, at a mixture or two-phase velocity of 0.3 m s^{-1} and void fraction of 0.3. These fluids have been considered by Kurimoto *et al.* (2017) in their experiments for gas-liquid slug flow and cover a range of liquid viscosities (given in Table 4.1). With an increase in liquid viscosity the capillary number increases from 0.0037 to 0.098. Whereas Reynolds number decreases from 336 to 21. Figure 4.20 shows the bubble shapes along with shear stress on the channel wall as calculated from Eq. (4.3). The volume of the bubble is same in all the cases. With an increase in the liquid viscosity, the bubble becomes longer and thinner. Bubble curvature at the front increases (and the radius of curvature decreases) with an increase in the liquid viscosity. The undulations at the back of the bubble are observed in all the cases but the amplitude of undulation is observed to decrease with an increase in the liquid viscosity. The thickness of the liquid film surrounding the bubble increases with an increase in the capillary number. Figure 4.21 shows the film thicknesses obtained from CFD calculation along with those obtained from Bretherton (1961) and Aussillous and Quéré expressions (2000). Bretherton expression is valid only for capillary number less than 0.005 whereas the A&Q expression is valid for viscous liquids as shown recently by Klaseboer *et al.* (2014). At low value of capillary number (Ca = 0.004), the film thickness is in good agreement with the Bretherton's correlation also. The film thickness obtained from CFD is in good agreement with A&Q correlation for all values of capillary numbers.

TH-2207_146107023

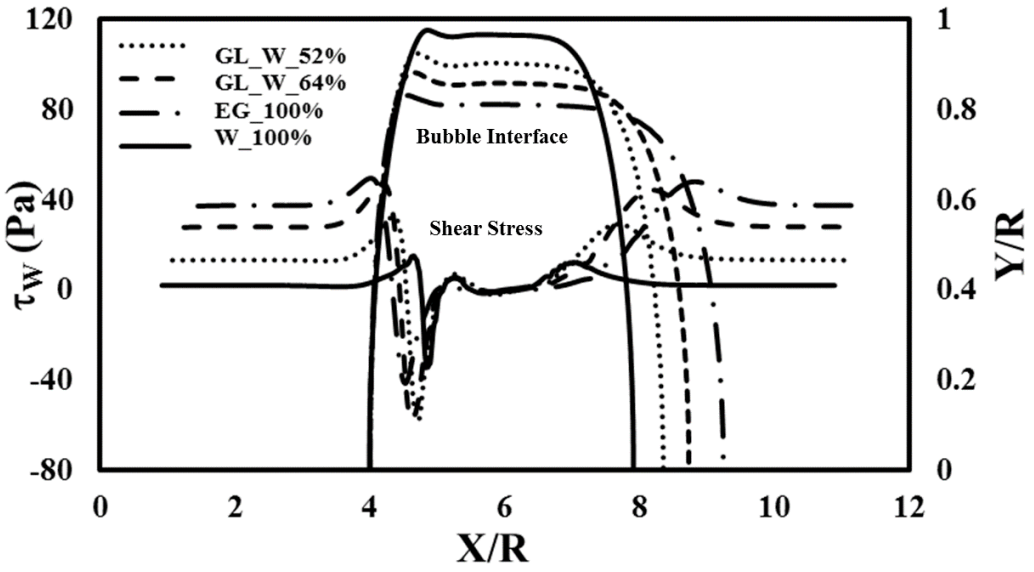

Figure 4.20: Bubble shape and wall shear stress for four air-water (Ca = 0.0037, Re = 336), air-water glycerol (52%) (Ca = 0.0247, Re = 60), air-water glycerol (64%) (Ca = 0.0517, Re = 30) and air-ethylene glycol (Ca = 0.0981, Re = 21) at a mixture velocity of 0.3 m s^{-1} *and* R_{eqv} *= 1.31.*

TH-2207_146107023

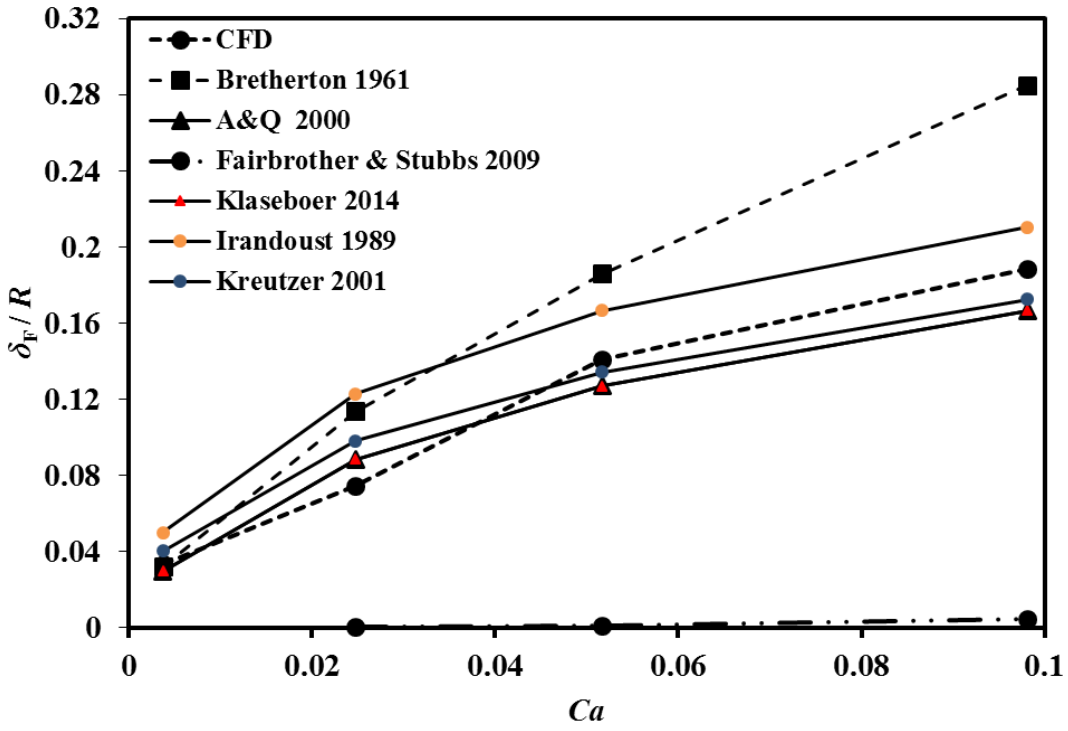

Figure 4.21: Film thickness as a function of capillary number

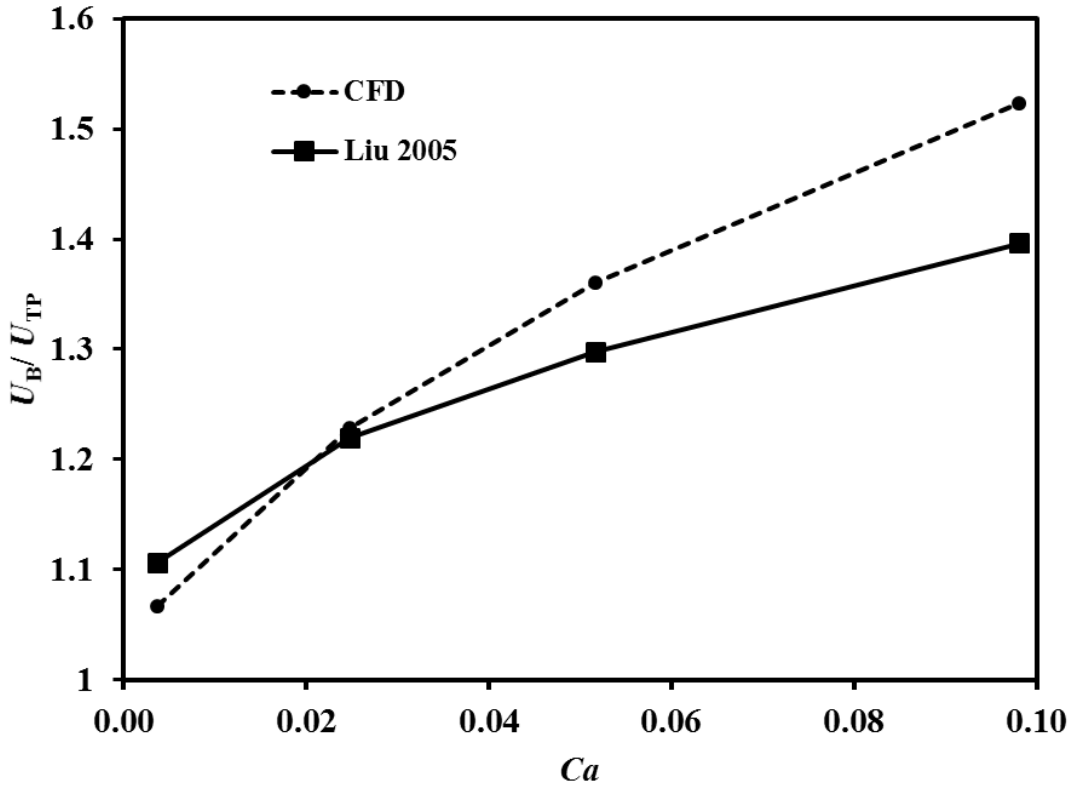

Figure 4.22: Bubble velocity as a function of capillary number.

TH-2207_146107023

Figure 4.22 shows the bubble velocities obtained from CFD calculations along with those obtained from Liu *et al.* (2005) correlation as given by Eq. (4.6) below.

$$\frac{U_B}{U_{TP}} = \frac{1}{1 - 0.61Ca^{0.33}} \tag{4.6}$$

Bubble velocity increases with an increase in capillary number i.e. the bubble moves with a higher velocity for the viscous liquid for the same mixture velocity. The bubble velocities obtained from CFD simulations are within 10% of those obtained from the Liu *et al.* (2005) correlation.

4.3.7 Shear Stress Model

Laborie and Cabassud (2005) calculated wall shear stress in a unit cell comprising of a gas bubble and a liquid slug using a simple mechanistic model developed by Fabre and Liné (1996). Here, the same model has been presented albeit with a simpler description. The model considers two zones: liquid slug and gas bubble. The shear stress on the wall in each zone is calculated assuming laminar, fully-developed flow using Hagen-Poiseuille law. The shear stress on the wall for the liquid slug is given by

$$\tau_{W,Slug} = \frac{8\mu_L U_{TP}}{d} \tag{4.7}$$

$$\tau_{W,Film} = \frac{8\mu_L U_F}{D_{Hyd,Film}} \tag{4.8}$$

where hydraulic diameter of the film, $D_{\text{Hyd, Film}}$ is $2\delta_F$. Laborie and Cabassud (2005) has given hydraulic diameter of the film as $4\delta_F$. The film velocity can be calculated by mass balance

$$U_F = \frac{A_{Ch}}{A_F} U_{TP} - \left(\frac{A_{Ch}}{A_F} - 1\right) U_B \tag{4.9}$$

TH-2207_146107023

where $A_{Ch} = \pi R^2$ is the channel cross sectional area and $A_F = \pi(R^2 - (R - \delta_F)^2)$ is the film cross sectional area. Eqs. (4.7-4.9) represents the model given in Laborie and Cabassud (2005).

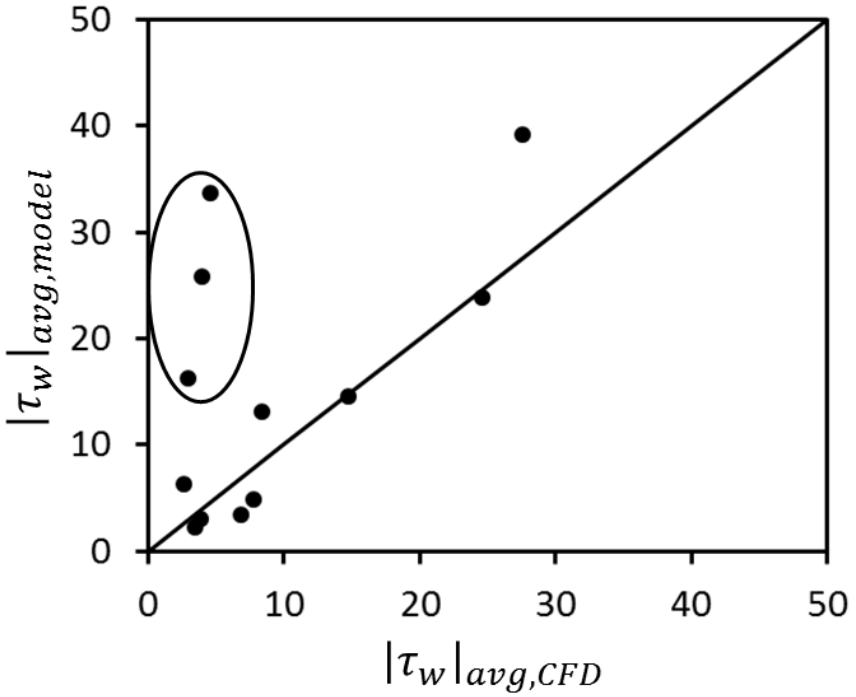

Figure 4.23: Comparison of the magnitude of wall shear stress obtained from CFD and the model.

The average magnitude of wall shear stress in a unit cell can be given by considering void fraction as the ratio of bubble length and slug length.

$$|\tau_w|_{UC,avg} = \varepsilon_G|\tau_{W,Slug}| + (1 - \varepsilon_G)|\tau_{W,Film}| \quad (4.10)$$

The comparison of the wall shear stress obtained from CFD and the phenomenological model is shown in Fig. 4.23. 75% data points (9 out of 12) are within one standard root mean square (RMS) error. The large disagreement is for the data encircled in the figure. For all the three cases, either the bubble or liquid slug is small. The model assumption of fully-developed flow is violated in both these cases. Further, the model does not take into account the variations in the

TH-2207_146107023

hydrodynamics at the nose and tail regions of the bubble and therefore is not valid when the bubble is short.

While the shear stress in the liquid slug region is very close to the value that obtained from CFD simulations, there are differences between the values obtained from model and CFD simulations in the gas bubble region. As described by Abiev *et al.* (2017), the hydrodynamics in the liquid film region is quite complex and the assumption of fully-developed laminar flow in the film is a very simplified model for the hydrodynamics in the film.

4.4 Conclusion

The observations of the hydrodynamic investigations can be summarised as:

- A CFD methodology to model gas-liquid Taylor flow in a periodic computational domain in a frame of reference moving with the bubble has been implemented in ANSYS Fluent 15. The bubble shape, velocity, film thickness and shear stress on the wall have been compared with the experimental data available in the literature.
- For $R_{eqv} \leq 1$, the bubbles are observed to have near spherical shape at low Reynolds number. At higher Reynolds number, the bubble has two distinct halves- a sharp one at the front and a flat half at the tail. For $R_{eqv} = 0.97$, the bubble shape at the back is observed to be same as that for a Taylor bubble. A low pressure zone exists between the channel wall and the middle of the bubble. The flow is observed to recirculate in this region in the laboratory frame of reference.
- For $R_{eqv} \geq 1$, the bubbles are observed to have the shape of a typical Taylor bubble- having ellipsoidal front, a cylindrical region in the middle and a ellipsoidal back with a small

TH-2207_146107023

undulation. With an increase in the bubble volume, the length of the cylindrical region increases whereas the bubble shape at the front and back remain same.

- The bubble velocity decreases with an increase in the bubble volume before it becomes volume-independent when bubble assumes the shape of a Taylor bubble.
- The effect of capillary number on the bubble shape has also been studied in the range Ca = 0.0037-0.098. The results obtained from CFD simulations have been compared with a simple phenomenological model available in literature for wall shear stress and found to be in good agreement for long Taylor bubbles whereas large deviations are observed for shorter bubbles.

TH-2207_146107023

Chapter 5

Heat Transfer in Slug Flow: Effect of Parameters

TH-2207_146107023

CHAPTER 5

Heat Transfer in Slug Flow: Effect of Parameters

This chapter presents a methodology to model heat transfer without phase change in periodic slug flow. Typical temperature field in the slug flow is described. The effect of bubble volume, Reynolds number, capillary number and slug length on heat transfer are studied. A phenomenological model to predict the heat transfer in the slug flow regime is presented.

5.1. Introduction

As discussed in Chapter 2, the rate of heat transfer in the gas-liquid slug flow can be significantly higher than that in fully-developed liquid-only flow. This enhancement in the rate of heat transfer is often attributed to two factors: (1) hydrodynamically and thermally developing flow in the liquid slugs and (2) internal recirculation within the liquid slug. The effectiveness of internal recirculation in the heat transfer depends upon the proximity of the recirculating zone with the channel wall: the closer the recirculation zone is to the wall, the higher the heat transfer coefficient. The role of the gas bubble is only to segment the flow and it hardly contributes towards heat transfer as the thermal mass of the gas is very low in comparison with that of the liquid (Gupta *et al.*, 2010, Leung *et al.*, 2010). An increase in the bubble volume therefore decreases the overall heat transfer coefficient in a unit cell (Zhang *et al.*, 2016). Thus it can be expected that the heat transfer would be efficient in a flow segmented by short bubbles having $R_{eqv} \sim 1$. The heat transfer performance in such systems can therefore be optimised by segmenting the flow using short but channel-size bubbles which segment the flow in the same manner as Taylor bubbles but occupy lesser channel volume. Further, the distance between the bubble (and the recirculating slug) and wall, the film thickness,

TH-2207_146107023

depends on the capillary number- the larger the capillary number, the thicker the film. The lengh of the liquid slug also affect the heat transfer significantly. The longer the slug, the greater the recirculation time of the fluid. Additionally, the thermal boundary layer would develop in a longer slug. In this chapter, the effect of bubble volume (R_{eqv}), Reynolds and capillary numbers and slug length on the heat transfer in the slug flow regime has been investigated.

5.2 CFD Methodology

The methodology to model the flow behaviour in a periodic unit cell in gas-liquid slug flow has been described in Chapter 4. As the bubble shape and hydrodynamics are steady and fluid properties are independent of temperature, the flow equations can be decoupled from the energy equation. Therefore, the temperature field can be obtained by solving the energy equation while the flow field is 'frozen'. To obtain the periodic temperature field, scaled temperature need to be wrapped from the outlet to the inlet of the domain as described in Chapter 3.

5.2.1 Solver Settings

As the flow field is not solved, the Courant number restriction need not be followed and a larger time step can be taken to solve the energy equation. A time step of the order of 10^{-4} s has been used to solve the energy equation. The convergence criteria for the energy equation was set 10^{-6} or below.

5.3 Results and Discussion

Heat transfer performance in fully-developed slug flow can be represented in term of Nusselt number defined as

$$Nu = \frac{hd}{k_L} = \frac{q_w}{(T_w - T_B)}\frac{d}{k_L} \tag{5.1}$$

TH-2207_146107023

The thermal conductivity of liquid phase has been used in Eq. (5.1) as only the liquid phase remains in contact with the wall at all times. The instantaneous local heat transfer coefficient at a cross section can be obtained by considering instantaneous local wall temperature $T_w(x,t)$ and local bulk mean temperature $T_B(x,t)$ which is given as

$$T_B(x,t) = \frac{\int_A \rho v_x(x,r,t) c_p T(x,r,t) dA}{\int_A \rho v_x(x,r,t) c_p dA} = \frac{\int_0^R \rho v_x(x,r,t) c_p T(x,r,t) 2\pi r dr}{\int_0^R \rho v_x T(x,r,t) c_p 2\pi r dr} \tag{5.2}$$

Time-averaged local Nusselt number can be calculated by considering time-averaged wall and bulk temperatures given by Eq. (5.3).

$$T_{w,av}(x) = \frac{\int_t^{t+T} T_w(x,t)\, dt}{\int_t^{t+T} dt} \tag{5.3a}$$

$$T_{B,av}(x) = \frac{\int_t^{t+T} \int_A \rho v_x c_p T\, dA\, dt}{\int_t^{t+T} \int_A \rho v_x c_p\, dA\, dt} \tag{5.3b}$$

Note that the time-averaged Nusselt number obtained using (5.1) and (5.3) would not be the same as obtained by time averaging the instantaneous Nusselt number i.e. that obtained using Eqs. (5.1) and (5.2).

As pointed out earlier, the flow is periodic in time and space and the periods in time (T) and space (L_{UC}) are related as $T = L_{UC} / U_B$. Therefore, the average Nusselt number can be obtained by

TH-2207_146107023

considering the a unit cell at any time instant. The mean wall and bulk temperatures can be obtained considering $t = x/U_B$.

$$T_{w,UC} = \frac{\int_x^{x+L_{UC}} T_w(x,t)\,dx'}{\int_x^{x+L_{UC}} dx'} \tag{5.4a}$$

$$T_{B,UC} = \frac{\int_x^{x+L_{UC}} \int_A \rho v_x c_p T\,dA\,dx'}{\int_t^{t+T} \int_A \rho v_x c_p\,dA\,dx'} \tag{5.4b}$$

These expressions for wall and bulk mean temperatures are same as those suggested by Gupta *et al.* (2010).

Table 5.1: Properties of the fluids used in the CFD simulations (Leung *et al.*, 2014) at 25 °C and atmospheric pressure

Properties	**Thermal Conductivity ($W\ m^{-1}\ K^{-1}$)**	**Specific Heat Capacity ($J\ kg^{-1}\ K^{-1}$)**
Air	0.02	1006.4
Water	0.6	4182.0

The thermal properties of the fluids have been given in Table 5.1. The simulations have been performed for several cases listed in Table 4.2 and have been described in the following sections.

5.3.1 Effect of Bubble Volume

The heat transfer in a unit cell has been represented by normalising the two phase Nusselt number with that for liquid-only, laminar, fully-developed flow for the same thermal boundary condition

TH-2207_146107023

on the wall. Note that the Nusselt number for single phase, laminar, fully-developed flow is a constant (Bejan, 2013) and has a value of 48/11 = 4.364 for constant wall heat flux boundary condition. The variation of normalised Nusselt number with the bubble volume represented by equivalent sphere radius has been shown in Fig. 5.1. The normalised Nusselt number increases from 2.0 to 3.3 with a decrease in equivalent sphere radius from 1.55 to 0.97. A further decrease in the equivalent sphere radius to 0.91 results in normalised Nusselt number decreasing to a value of 2.5 and finally it reduces to 1.18 at an equivalent sphere radius of 0.72. Thus the Nusselt number is observed to have a maximum value at $R_{eqv} \sim 1$ and decreases on moving away from it.

With a change in bubble volume the following parameters vary in the simulations: slug length, the volume, length and shape of the bubble. Although the bubble and slug lengths are almost same for R_{eqv} = 0.91 and 0.97, there is a large difference in the values of Nusselt number in the two cases. This can be understood by temperature distribution plotted in Fig. 5.2. The difference in wall and fluid temperatures is smaller in the case of R_{eqv} = 0.97. As can be seen in Fig. 4.9 in chapter 4, the minimum film thicknesses for R_{eqv} = 0.91 and 0.97 are 0.04R and 0.06R, respectively. The larger value of Nusselt number in case of R_{eqv} = 0.97 can be attributed to the deeper penetration of the bubble in the thermal boundary layer for this case.

For the case of R_{eqv} = 0.72, Nusselt number is close to that for liquid-only flow. As the bubble and the recirculating liquid slug is very far from the channel wall, very little heat transfer enhancement is achieved in this case as compared to the other cases where the bubble is close to the wall.

For the comparison of R_{eqv} = 0.97 and 1.15, there are two opposing effects: R_{eqv} = 1.15 has smaller minimum film thickness and larger bubble volume. The cumulative effect is an increase in Nusselt number. A further increase in R_{eqv} causes the bubble volume to increase and consequently the Nusselt number to decrease.

TH-2207_146107023

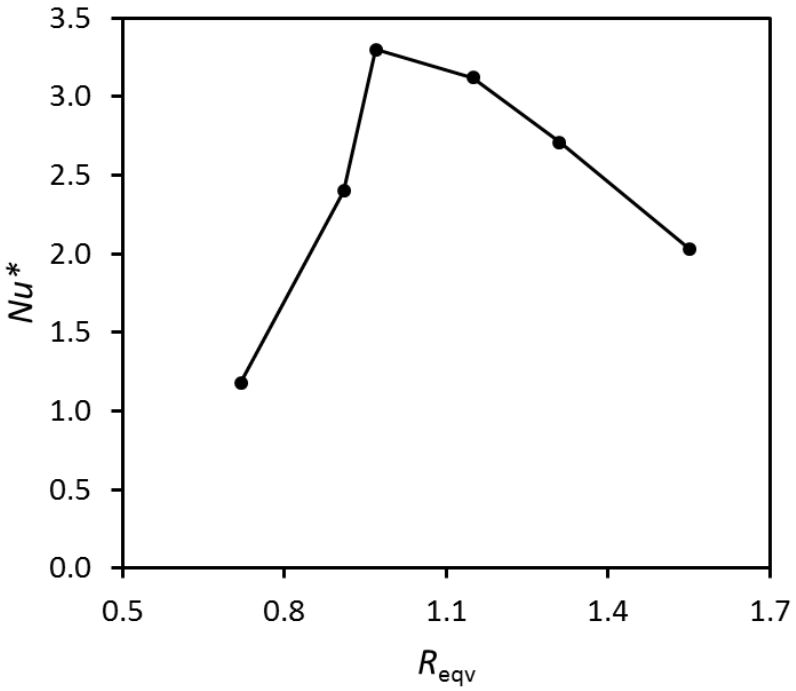

Figure 5.1: Variation of Normalised Nusselt number with equivalent sphere radius at a Reynolds number of 336.

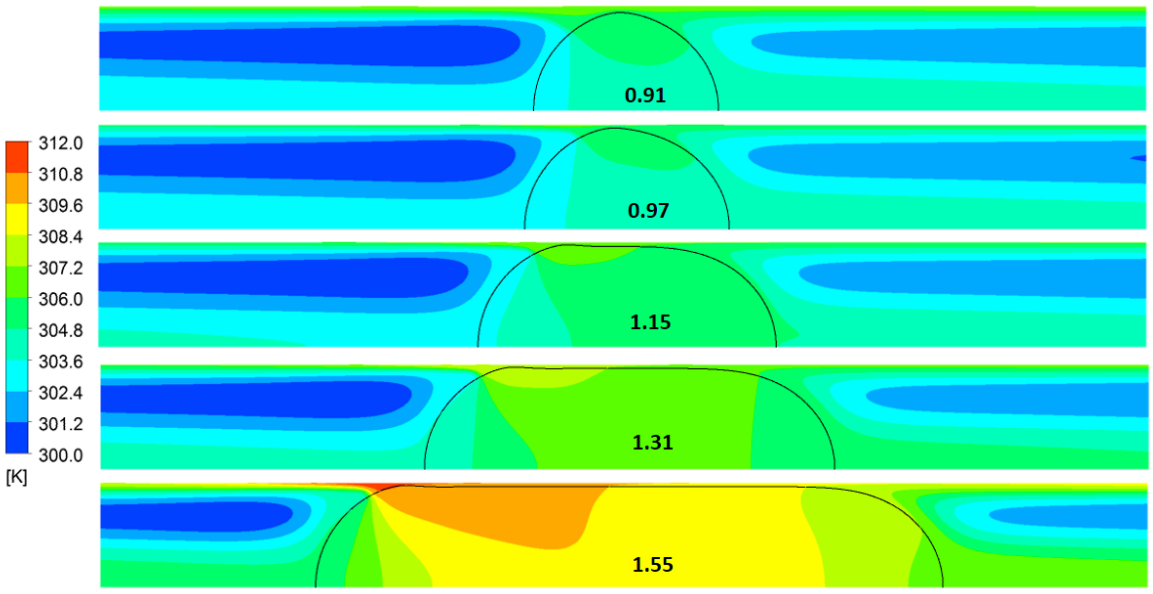

(a)

TH-2207_146107023

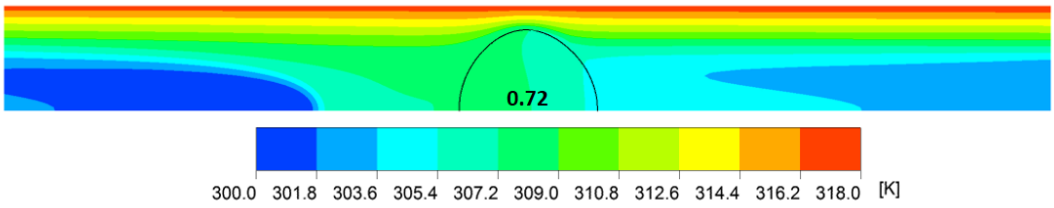

(b)

Figure 5.2: Temperature contour plots for equivalent sphere radius (a) 0.91-1.55 and (b) 0.72 at a Reynolds number of 336.

5.3.2 Effect of Reynolds Number

The effect of Reynolds number on the heat transfer has been studied for two cases of R_{eqv} : one having value less than one (0.91) and another having value more than one (1.31). The normalised Nusselt number as a function of Reynolds number has been plotted in Fig. 5.3. For R_{eqv} = 0.91, the normalised Nusselt number increases from a value of 1.8 at *Re* = 224 to 3.0 at *Re* = 560. However, for R_{eqv} = 1.31, the Nusselt number is almost independent of Reynolds number.

Figure 5.4 shows the temperature distribution at R_{eqv} = 0.91 for Reynolds numbers 224, 336, 448 and 560. With an increase in Reynolds number, the difference between the wall temperature and the fluid temperature can be observed to decrease. This can be attributed to the increase in the size of the reciculating liquid with the increase in Reynold number. A bigger recirculation brings about hotter liquid from wall towards the axis making the heat transfer more effective.

Figure 5.5 shows the temperature distribution at R_{eqv} = 1.31 for Reynolds numbers 224, 336, 448 and 560. Although, the fluid temperature at the tail of the bubble is observed to be high at low Reynolds numbers, the size of the recirculation zone is almost same in all the cases. Consequently, the difference between the average wall and bulk temperatures and therefore the Nusselt number is independent of Reynolds number. In their CFD simulations, Gupta *et al.* (2010) also observed the Nusselt number to be independent of Reynolds number in gas-liquid Taylor flow. It is

TH-2207_146107023

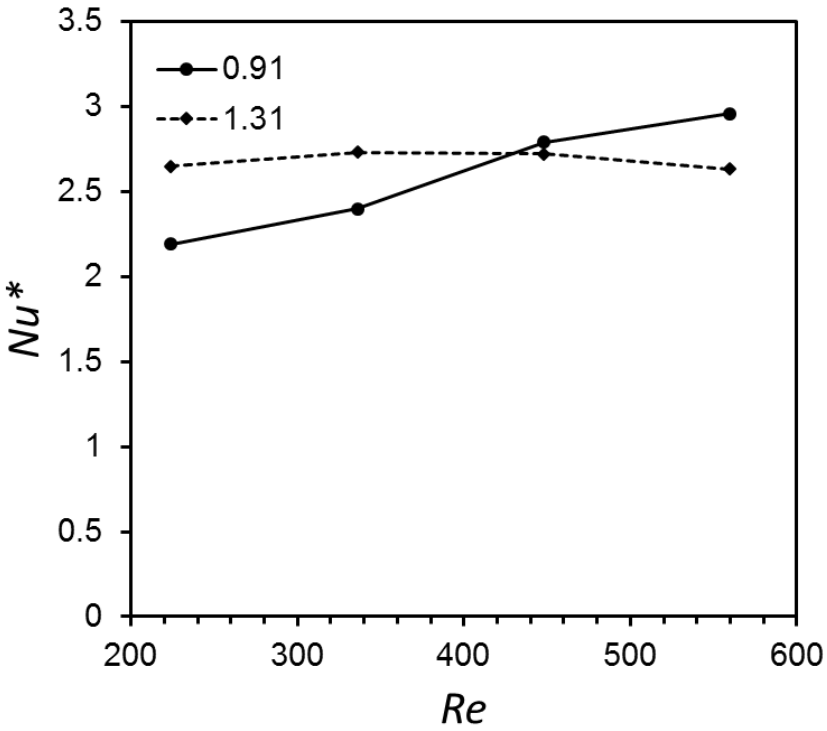

Figure 5.3: Normalised Nusselt number as a function of Reynolds number for a near-spherical (R_{eqv} = 0.91) and a Taylor bubble (R_{eqv} = 1.31).

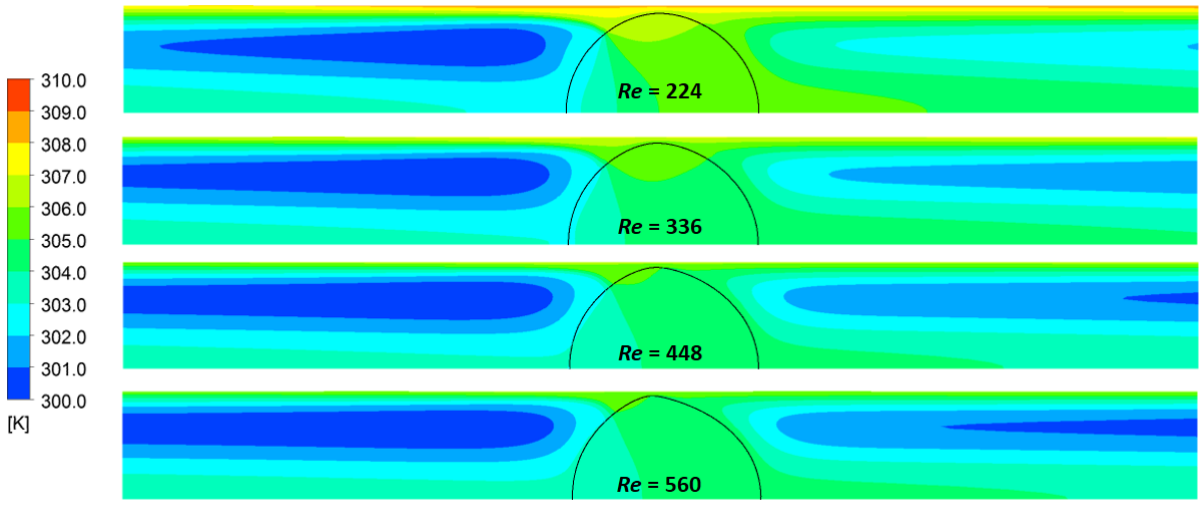

Figure 5.4: Bubble shape (interface shown by solid black line) and tempereture field for equivalent sphere radii (R_{eqv}) of 0.91 for a channel Reynolds number of 224, 336, 448, 560.

TH-2207_146107023

interesting to note here that the Nusselt number in the fully-developed single phase flow is independent of Reynolds number.

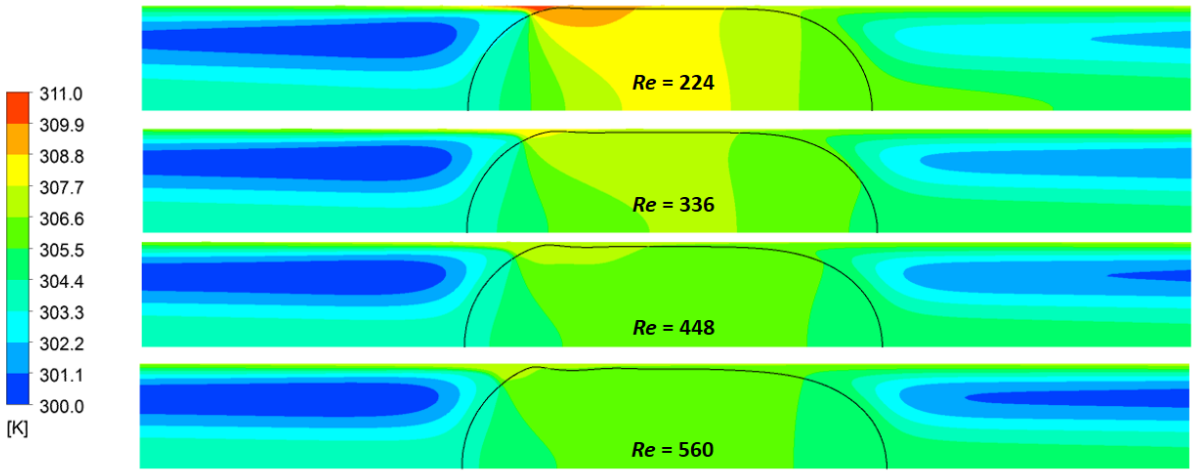

Figure 5.5: Bubble shape (interface shown by solid black line) and Tempereture field for equivalent sphere radii (R_{eqv}) of 1.31 for a channel Reynolds number of 224, 336, 448, 560.

5.3.3 Effect of slug length

Heat transfer in the gas-liquid slug flow depends strongly on the slug length. For shorter slug lengths, the flow and heat transfer in the liquid slug remains developing throughout whereas the flow and heat transfer approach to a fully-developed state in longer slugs. Variation in slug length is often associated with changes in other flow parameters. For example, as studied in Section 5.3.1, a change in gas volume fraction in a unit cell of constant length also causes change in the slug length.

In this section, first the slug lengths have been varied keeping the bubble volume unchanged. This allows studying the effect of slug length keeping the hydrodynamics and heat transfer in the bubble region unchanged. The increase in slug length also causes an increase in the unit cell length and a decrease in the bubble volume fraction. The effect of slug length on heat transfer has been

TH-2207_146107023

investigated keeping the bubble volume constant having equivalent sphere radius of 1.46*R* at a two-phase Reynolds number of 336 by varying the unit cell length from 5 to 10 mm. The slug length varies correspondingly from 2.36 - 7.3 mm.

Figure 5.6 (a) shows the velocity profile at a cross-section in the middle of the liquid slug i.e. at the domain exit. The non-dimensional centreline velocity varies from 1.90 to 1.97 as the slug length increases from 2.36 to 7.3. Figure 5.6(b) shows the variation of the centreline velocity along the axial direction for unit cell of length (L_{UC}) 10 mm. The location of the points at which the centreline velocity reach 90% and 95% of the maximum possible velocity ($2U_{TP}$). It can be seen that the 1.8 U_{TP} (90%) is attained at a distance of 1.5*d* and whereas 95% is attained 3.0*d*.

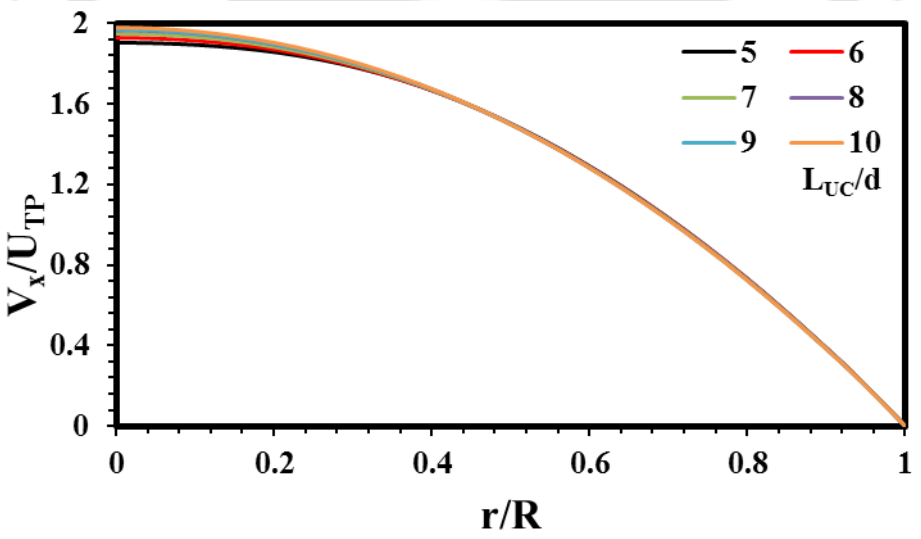

Figure 5.6(a): Velocity profile in the middle of the liquid slug for air-water flow in a channel of diameter 1 mm for a gas bubble having equivalent sphere diameter of 1.46R at a Reynolds number of 336 for unit cell length (L_{UC}) 5, 6, 7, 8, 9 and 10 mm. The slug lengths are 2.36, 3.36, 4.35, 5.3,6.38 and 7.3 mm.

TH-2207_146107023

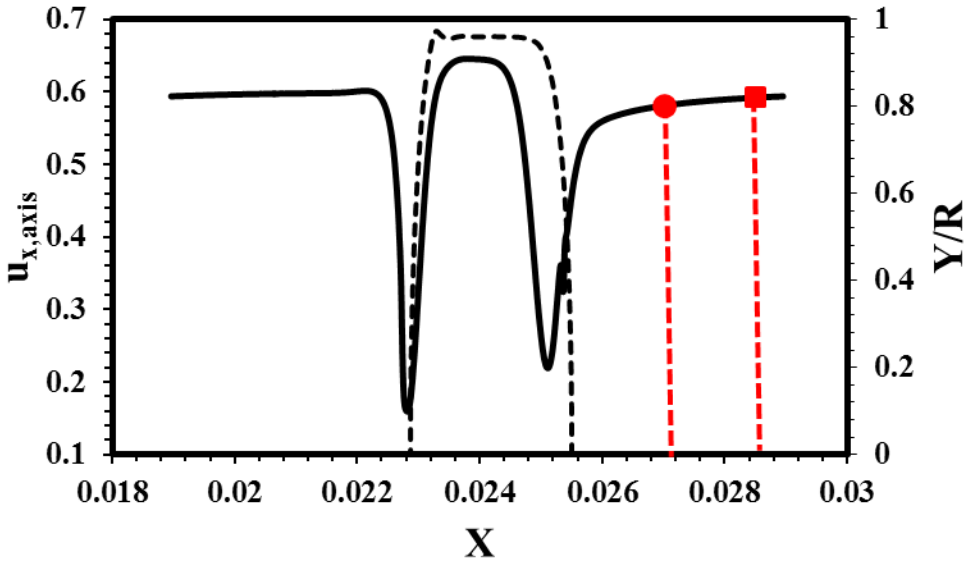

Figure 5.6(b): Variation of the centreline velocity along the axial direction at a Reynolds number of 336 for unit cell length (L_{UC}) 10 mm. The slug lengths are 7.3 mm. Distance from bubble nose 0.001494 for 90% (●) and 0.002994 mm for 95%(■).

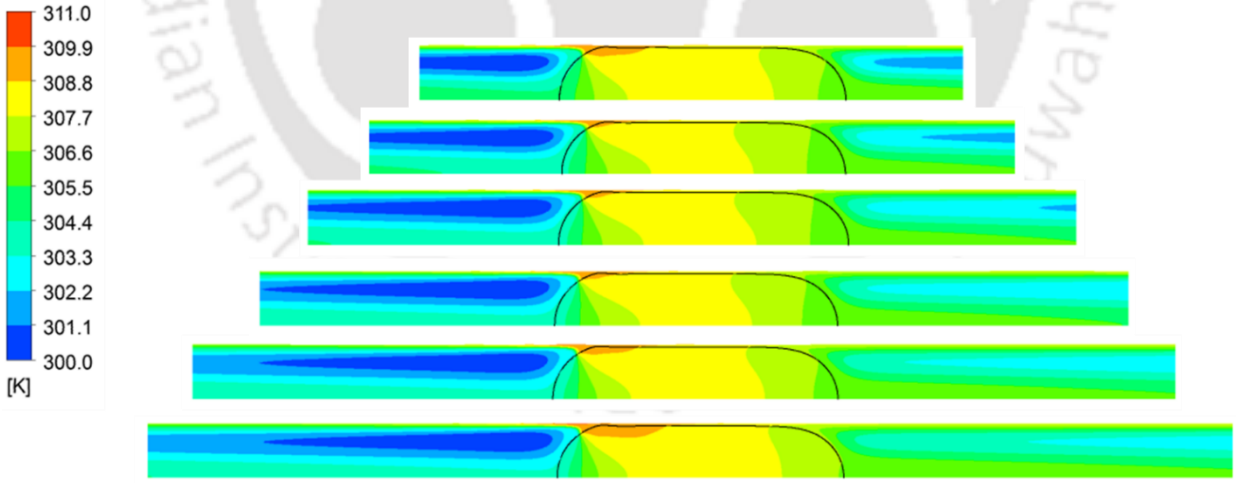

Figure 5.7: Temperature contour plots in a channel of diameter 1 mm for a gas bubble having equivalent sphere diameter of 1.46 R at a Reynolds number of 336 for unit cell length (L_{UC}) 5, 6, 7, 8, 9 and 10 mm. The slug lengths are 2.36, 3.36, 4.35, 5.3, 6.38 and 7.3 mm.

TH-2207_146107023

Figure 5.7 shows the temperature contour plot for all the cases. Temperature scale has been adjusted so as to have the same minimum temperature in all the cases. Temperature distribution is the gas bubble is observed to be almost similar for all the cases. The temperature is observed to be minimum in the liquid film near the tail of the bubble where the temperature is minimum in the liquid slug following the gas bubble. As the slug length increases, the recirculation time i.e. the time required for the liquid to complete one cycle in the liquid slug increases. This causes a reduction in the Nusselt number with increase in slug length.

In Fig. 5.8, the variation of normalized Nusselt number with non-dimensional slug length has been plotted. The Nusselt number is observed to increase with increase in slug length at low values of slug length. The change in Nusselt number becomes smaller with an increase in slug length and finally there is almost no change in Nusselt number with an increase in slug length. However, the increase in the slug length is accompanied by the decrease in gas volume fraction (and increase in liquid volume fraction) in these cases. Thus, the change in Nusselt number seen in Fig. 5.8 is a combination of two contrasting effects: a decrease in gas volume fraction which causes Nusselt number to increase whereas an increase in slug length which causes a decrease in Nusselt number. As the contribution of gas bubble is almost negligible in slug flow heat transfer, the slug Nusselt number can be defined as (Leung *et al.*, 2012.)

$$Nu^*_{Slug} = \frac{Nu^*}{1-\varepsilon_G} \tag{5.5}$$

In Fig. 5.9, the variation of normalized slug Nusselt number with the slug length is shown. The slug Nusselt number decreases with an increase in the slug length.

TH-2207_146107023

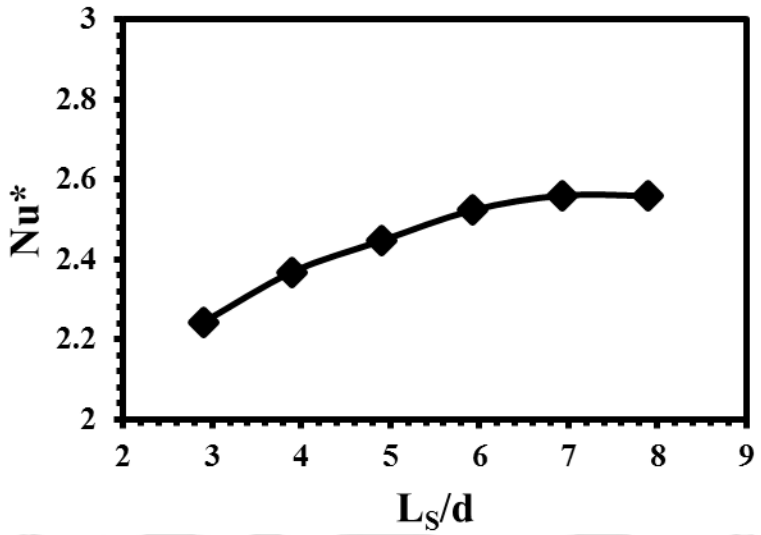

Figure 5.8: Variation of normalized Nusselt number (Nu) with slug length (L_s) in a channel of diameter 1 mm for a gas bubble having equivalent sphere diameter of 1.46 R at a Reynolds number of 336 for unit cell length (L_{UC}) 5, 6, 7, 8, 9 and 10 mm. The slug lengths are 2.36, 3.36, 4.35, 5.3, 6.38 and 7.3 mm.*

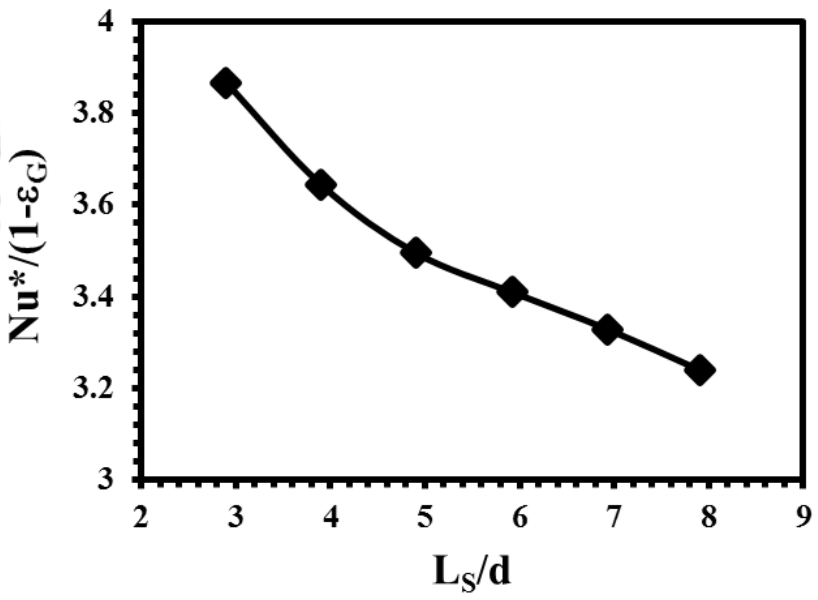

Figure 5.9: Variation of normalized slug Nusselt number ($Nu^*/(1-\varepsilon_G)$) with slug length (L_s) in a channel of diameter 1 mm for a gas bubble having equivalent sphere diameter of 1.46 R at a

TH-2207_146107023

Reynolds number of 336 for unit cell length (L_{UC}) 5, 6, 7, 8, 9 and 10 mm. The slug lengths are 2.36, 3.36, 4.35, 5.3,6.38 and 7.3 mm.

Further CFD simulations have been carried out to study the effect of slug length while keeping the gas volume fraction in a unit cell fixed. The unit cell length was varied from 2 to 10 mm for a gas volume fraction of 0.42. The increase in slug length for these cases also results in an increase in the unit cell length and bubble volume. Figure 5.11 shows the contour plot of temperature for all the cases. As earlier, the minimum temperature in all the cases have been shifted to 300 K.

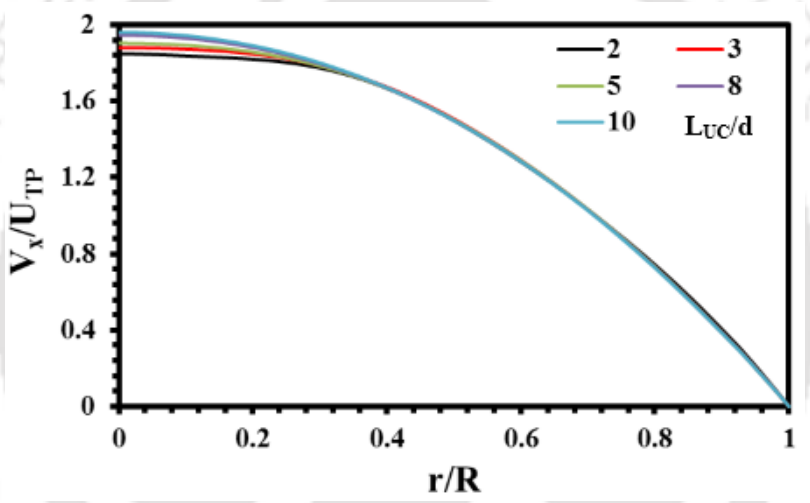

Figure 5.10: Velocity profile in the middle of the liquid slug for air-water flow in a channel of diameter 1 mm for a gas volume fraction of 0.42 at a Reynolds number of 336 for unit cell length (L_{UC}) 2, 3, 5, 8 and 10 mm. The slug lengths are 0.74, 1.30, 2.36, 4.02 and 5.10 mm.

Figure 5.10 shows the velocity profile at a cross-section in the middle of the liquid slug i.e. boundaries of the computational domain for air-water flow in a channel of diameter 1 mm for a gas volume fraction of 0.42 at a Reynolds number of 336 for unit cell lengths of 5, 6, 7, 8, 9 and 10 mm. The non-dimensional centreline velocity varies from 1.84 for slug length of 0.74 mm and 1.92 for slug length of 5.1 mm in the middle of the liquid slug.

TH-2207_146107023

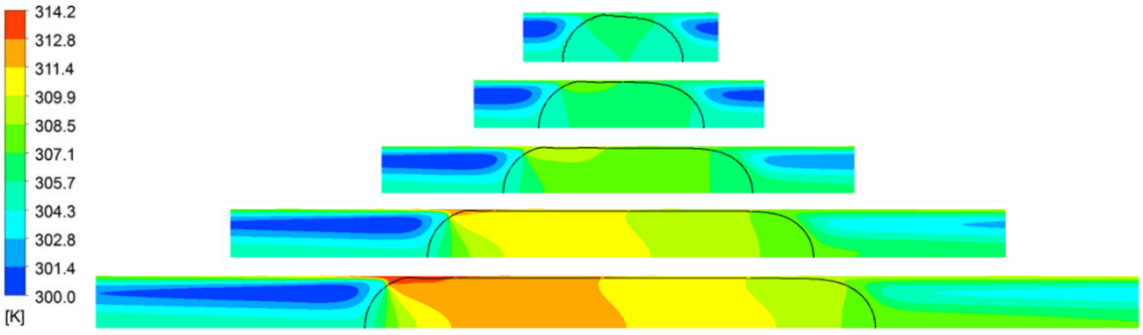

Figure 5.11: Temperature contour plots for air-water flow in a channel of diameter 1 mm for a gas volume fraction of 0.42 at a Reynolds number of 336 for unit cell length (L_{UC}) 2, 3, 5, 8 and 10 mm. The slug lengths are 0.74, 1.30, 2.36, 4.02 and 5.10 mm.

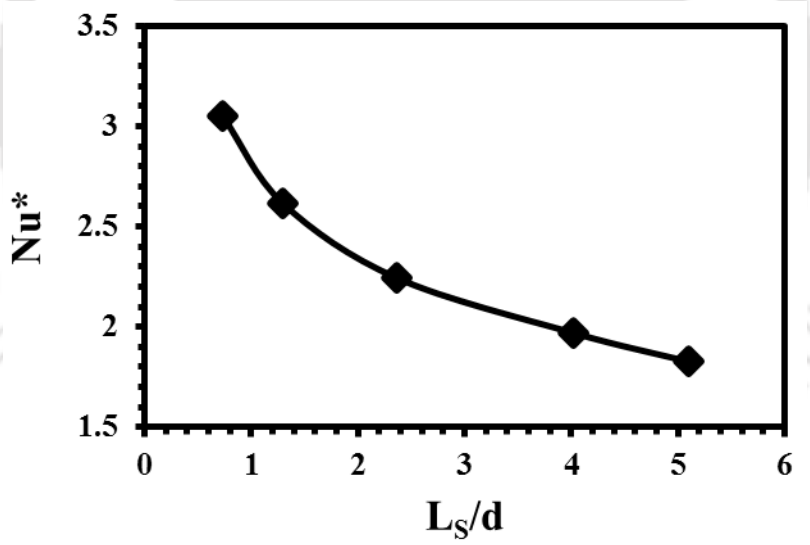

Figure 5.12: Variation of normalized Nusselt number with slug length for air-water flow in a channel of diameter 1 mm for a gas volume fraction of 0.42 at a Reynolds number of 336.

Figure 5.12 shows the variation of normalized Nusselt number with slug length. The Nusselt number decreases from 3.05 to 1.82 with an increase in slug length from 0.74 mm to 5.1 mm. The

TH-2207_146107023

normalized Nusselt number increases linearly with decrease in slug length for longer slugs ($L_S \geq$ 2.4 mm) but for the shorter slugs, the increase in Nu* is more with decrease in slug length.

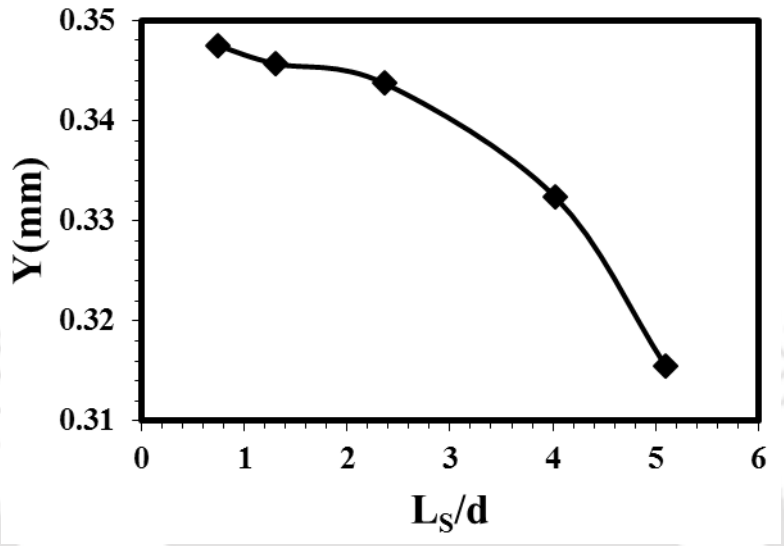

Figure 5.13: Distance from axis of centre of recirculation in the liquid slug a gas volume fraction of 0.42 at a Reynolds number of 336 for unit cell length (L_{UC}) 2, 3, 5, 8 and 10 mm. The slug lengths are 0.74, 1.30, 2.36, 4.02 and 5.10 mm.

The center of recirculation in the liquid is the point at which the fluid has same velocity in the axial direction as the bubble velocity and zero radial velocity. In a bubble frame of reference, the fluid between the center of recirculation and the wall moves in the backward direction whereas the fluid between the axis and the center of recirculation moves in the forward direction. Location of the center of recirculation can thus have an effect on the fluid mixing. In Fig. 5.13, the radial location of the center of recirculation has been plotted with the slug length. As the slug length decreases, the center of recirculation moves towards the wall.

TH-2207_146107023

5.3.4 Heat Transfer Model

Gupta (2010) developed a phenomenological model for heat transfer in Taylor flow regime. The model was based on the assumption of the flow of Taylor bubbles and liquid slugs alternately on a thin liquid film. However, the model did not have any closure for the heat transfer between the film and gas bubble/ liquid slug. Dai *et al.* (2016) simplified the model to calculate two-phase Nusselt number in gas-liquid and liquid-liquid Taylor flow. The model considered heat transfer from the wall to the continuous film region and from the film separately to the Taylor bubble/droplet and liquid slug. The model is based on the summation of apparent resistances to heat transfer. In non-dimensional terms, it can written as:

$$\frac{1}{Nu_{TP}} = \frac{1}{Nu_{Film}} + \frac{L_{UC}}{L_B}\left(\frac{m}{m+1}\right)^2 \frac{k_L}{k_G}\frac{1}{Nu_B} + \frac{L_{UC}}{L_S}\left(\frac{1}{m+1}\right)^2 \frac{1}{Nu_S} \tag{5.6}$$

where Nu_{Film}, Nu_{B} and Nu_{S} are the Nusselt numbers for heat transfer from the channel wall to the liquid film, film to the gas bubble and film to the liquid slug, respectively. The bubble length can be approximated as

$$L_B = \varepsilon_G L_{UC} \tag{5.7}$$

k_{L} and k_{G} are the thermal conductivies of the liquid and gas phases, respectively, and m is

$$m = \frac{\dot{Q}_G \rho_G c_{p,G}}{\dot{Q}_L \rho_L c_{p,L}} \tag{5.8}$$

For the air-water system, m approaches zero and the Eq. (5.6) reduces to

$$\frac{1}{Nu_{TP}} = \frac{1}{Nu_{Film}} + \frac{L_{UC}}{L_S}\frac{1}{Nu_S} \tag{5.9}$$

Heat transfer in the liquid film is obtained assuming the liquid film to be stagnant i.e.

$$Nu_{Film} = \frac{k_L}{\delta_F}\frac{d}{k_L} = \frac{d}{\delta_F} \tag{5.10}$$

Where the film thickness can be obtained using A&Q correlation given by

$$\frac{\delta_F}{R} = \frac{1.34Ca^{2/3}}{1 + 3.34Ca^{2/3}} \tag{5.11}$$

TH-2207_146107023

Heat transfer in the liquid slug can be obtained using (Leung *et al.*, 2010)

$$Nu_S = 4.364 + \frac{a_1}{L_S^* + a_2 {L_S^*}^{1/3}} \tag{5.12}$$

Dai et al. (2016) obtained the values of a_1 and a_2 to be 0.171 and 0.0663, respectively, by the least-square fit for the gas-liquid Taylor flow data of Leung et al. (2010). Figure 5.14 compares the values of normalised Nusselt numbers (shown by the filled circular symbols) obtained from the phenomenological model with that obtained from CFD simulations for all the cases of heat transfer discussed above. The Nusselt number values obtained from CFD and phenomenological models are within 15% for all the cases of Taylor flow ($R_{eqv} \geq 1.15$). The largest difference between the two is obtained for the cases of R_{eqv} = 0.72 at Re = 336. The other two points having difference larger than 15% are for R_{eqv} = 0.91 at Re = 224 and 336. The model considers the liquid film obtained from the correlation for Taylor flow which is not valid for short bubbles. The liquid film for all the three cases having larger difference between the two Nu values is significantly thicker than that obtained from Eq. (5.10). The Nusselt numbers using a liquid film thickness obtained from CFD simulations for these three cases improves the model prediction as shown the by the (×) symbol in Fig. 5.14. For the other case of spherical bubbles (R_{eqv} = 0.91 and Re = 448 and 560 and R_{eqv} = 0.97 and Re = 336), there is little difference between the film thickness obtained from CFD simulations and that obtained using Eq. (5.10) and therefore, there is good agreement between the Nusselt number values obtained from CFD and the model.

TH-2207_146107023

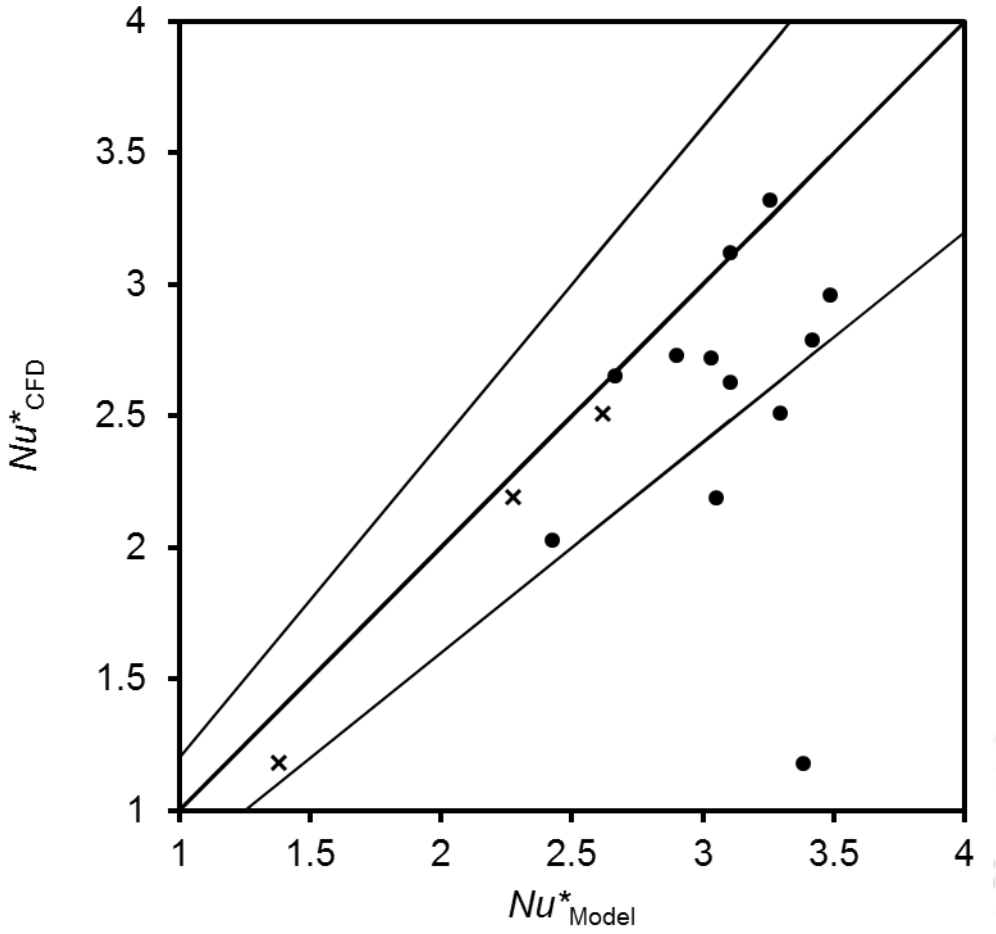

Figure 5.14: Comparison of the normalised Nusselt number obtained from CFD simulations and the phenomenological model of Dai et al. (2015) shown by solid circular symbols. The solid line in the middle represents when the values from CFD and phenomenological models are equal. Two lines around it represents ±15% boundary. The (×) represents the cases of short bubbles using film thickness as the actual distance between the bubble and the wall as obtained in CFD simulations.

5.4 Conclusion

CFD simulations have been performed for air-water slug flow in a channel of diameter 1 mm to understand the effect of bubble volume on the flow and heat transfer. The equivalent sphere

TH-2207_146107023

diameter (R_{eqv}) of the bubble has been varied from 0.72 to 1.55 and the channel Reynolds number has been varied between 112-560 by increasing the mixture velocity. It has been observed that the overall Nusselt number has been observed to be maximum $R_{eqv} \sim 1$. An increase or decrease in the volume fraction causes the Nusselt number to decrease. For $R_{eqv} < 1$, the heat transfer is determined by the radial size of the recirculation in the liquid slug. The closer the recirculation to the wall, the better is the heat transfer. With an increase in Reynolds number, the minimum distance between bubble and wall decreases, the size of the recirculation in the liquid increases and consequently, the Nusselt number also increases. For $R_{eqv} > 1$, the Nusselt number is observed to be independent of Reynolds number. The higher the value of L/d, the lower is the Nusselt number. The Nusselt numbers obtained from CFD simulations have been compared with the phenomenological model developed by Dai et al. (2015) for $R_{eqv} > 1$ and found to be within 15%. For $R_{eqv} < 1$, replacing the film thickness calculated from the model with that obtained from CFD simulation results in good agreement between the two.

TH-2207_146107023

Chapter 6

Hydrodynamics of Coalescence of Short and Long Bubbles

TH-2207_146107023

CHAPTER 6

Hydrodynamics of Coalescence of Short and Long Bubbles

In this chapter the hydrodynamics of short and long bubbles in two phase flow in microchannels is studied. The hydrodynamics during approach of short bubble to the long bubble, bubble velocity, velocity along the length of slugs has been investigated. Circulations patterns during the coalsecence and disruption and the re-establishment of equilibrium is also sudied.

6.1 Introduction

As shown in Chapter 4, the velocity of a small spherical bubble is greater than that of a Taylor bubble. Therefore, if a long bubble is followed by a shorter one, it can be expected that they would coalesce and form a longer capsular bubble. When the bubbles are sufficiently far away from each other, they do not affect the shape and velocity of the adjacent bubbles. However, when the distance between the bubbles is reduced, the hydrodynamic interactions between the two may cause changes in the shape and velocity of the bubbles. The process of bubble interaction and formation of a single bubble can be categorised in three steps: bubble approach, drainage of the thin film between bubbles and contact between bubbles and growth of the doublet formed after contact. The process of interaction between two bubbles has been modelled in a frame of reference moving with either of the bubbles. When the distance between the bubbles is 1-2 grid elements, the interface ruptures, not capturing the thin film drainage process accurately. However, the bubbles form a doublet after the coalescence which grows to a steady shape and this process has been modelled using CFD simulations.

TH-2207_146107023

6.2 CFD Methodology

The coalescence process has been assumed to be axisymmetric and the simulations have been performed in an axisymmetric computational domain. The simulations have been performed in a frame of reference moving with the longer Taylor bubble. To capture the gas-liquid interface, volume of fluid (VOF) method has been employed. Both the fluids are assumed to be incompressible and properties of the fluids such as viscosity, density and surface tension are assumed to be constant. As the pressure change during flow in microchannels is small, the effect of pressure on the density can be safely neglected. Both the fluids are assumed to be Newtonian. The solubility of the gas phase in the liquid and Ostwald ripening effects have not been considered.

6.2.1 Boundary Conditions

As the domain moves with the velocity of the Taylor bubble, only the liquid phase is present at the domain inlet and outlet boundaries. At the inlet a parabolic velocity profile is specified with an average velocity of 0.3 ms^{-1}. A pressure outlet boundary condition is applied at the outlet with a uniform gauge pressure of 0 Pa. A no-slip boundary condition is employed at the channel wall.

6.2.2 Initial Conditions

Initially, the same parabolic velocity profile that applied at the inlet is specified in the entire domain. The pressure in the domain has been specified to be zero initially. The initial shapes of the bubbles are spherical and capsular i.e. spherical ends and a cylindrical middle for the spherical and Taylor bubbles, respectively. Initially, the spherical bubble is placed at a distance of one channel diameter from the inlet and the distance between the spherical and Taylor bubble is at least 4 channel diameters.

TH-2207_146107023

6.2.3 Modelling Approach

While the problem of motion of two bubbles moving with different velocities and coalescing is not steady in a bubble frame of reference also, modelling it in the frame of reference moving with one of the bubbles is advantageous as the required computational domain is significantly shorter than what would be required for solving the problem in a laboratory frame of reference.

For the work described in Chapters 4 and 5, the moving domain method has been to simulate periodic Taylor flow in a unit cell consisting of a bubble and two adjacent halves of liquid slug in the bubble frame of reference. The bubble was placed in the middle of the computational domain and its velocity was calculated dynamically using Eq. (6.1).

$$U_{Domain} = \frac{\int_{x}^{x+L}\int_{0}^{R} \alpha_G u_x (2\pi r)\, dr dx'}{\int_{x}^{x+L}\int_{0}^{R} \alpha_G (2\pi r)\, dr dx'} \tag{6.1}$$

where L is the length of complete domain and α_G is the volume fraction of the gas phase. Using Eq. (6.1) for the present case i.e. two gas bubbles moving with different velocities would result in the computational domain moving with the mass-weighted average velocity of the two bubbles. However, the velocity of only one bubble can be calculated by changing the integration limits such that only the bubble under consideration is between them. Preliminary simulations suggested that the bubble at the front moves with a constant velocity until the two bubbles merge together. Therefore, the computational domain is moved with the velocity of the Taylor bubble.

The challenge in calculating the velocity of an individual bubble is finding the x-coordinates surrounding a bubble dynamically i.e. at every time step. In this work, k-means clustering or Llyod's algorithm (Macqueen 1967), an unsupervised learning algorithm, has been implemented to keep track of the ends of the bubbles. After identifying the location of the bubble ends on the

TH-2207_146107023

axis, the axial location of the midpoint between the bubbles is calculated. The velocity of both the bubbles are calculated individually by choosing the integration limits in Eq. (6.1) from start of the domain to the midpoint between the bubbles and from midpoint between the bubbles to the end of the domain for the spherical and Taylor bubbles, respectively.

k-means clustering algorithm is employed for clustering analysis in data mining. The algorithm partitions the data into k different clusters such that each data point belongs to the cluster having the nearest mean value. The problem is initialised by assuming k centroids which serve as initial guesses for the location of the clusters. In the next step, each data point is associated with its nearest cluster. This is known as the assignment step. When all the points have been associated with a centroid, new centroids are calculated as the mean of the value of the data points associated with the new clusters. This is called the update step. The algorithm alternates between the two steps until the new centroids are identical to the previous ones.

In order to find the location of the ends of the bubbles, the interface cells of both the bubbles (having $0 < \alpha_G < 1$) are extracted at every iteration. From these interface cells, all the cells whose distance from the axis is below a pre-defined cut-off value are selected. Here, this threshold is selected as ten times the mesh size in the radial direction. The axial coordinates ($\boldsymbol{X} = x_1, x_2, \ldots, x_N$) of these cells are used as data points for clustering. The goal now is to divide the data points into four clusters each associated with an end of a bubble. To start with the four cluster centroids are obtained from the axial coordinates of the bubble ends obtained after initializing the domain. These serve as the initial guesses for the clusters before the iterations start. k-means clustering is guaranteed to converge, however the configuration of clusters to which it converges is, in general, not unique and depends on the initial guesses of the centroids. Therefore, it is important to initialize centroids near the bubble ends at $t = 0$. A fixed number of iterations (10) are performed at every

TH-2207_146107023

time-step. The centroids at the end of 10 iterations are taken as the coordinates of the ends of the bubbles. The cluster centroids after each time step would be located as shown in Fig. 6.1.

At every time-step the centre of the liquid slug between the two bubbles is used to define a boundary between two regions containing one bubble each. The axial coordinate of this line is defined as the arithmetic mean of x_{C2} and x_{C3}.

$$x_C = \frac{(x_{C2} + x_{C3})}{2} \tag{6.2}$$

Now, the velocity of the larger bubble can be calculated as

$$U_L = \frac{\int_{x_C}^{x+L} \int_0^R \alpha_G u_x (2\pi r)\, dr dx'}{\int_{x_C}^{x+L} \int_0^R \alpha_G (2\pi r)\, dr dx'} \tag{6.3}$$

and the velocity of the smaller bubble

$$U_S = \frac{\int_{x}^{x_C} \int_0^R \alpha_G u_x (2\pi r)\, dr dx'}{\int_{x}^{x_C} \int_0^R \alpha_G (2\pi r)\, dr dx'} \tag{6.4}$$

As the shape of the computational domain remains unchanged, a `rigid body' treatment was used to move the mesh in the direction of the flow with a velocity equal to that of the larger bubble. A dynamic layering method was used to update the mesh at each time step.

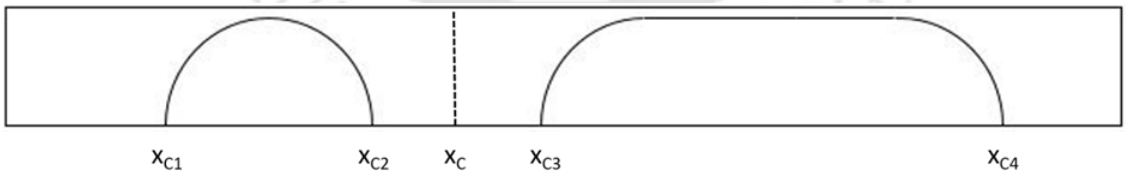

Figure 6.1: The domain with gas-liquid interface and location of the bubble ends. The centreline of the liquid slug is shown with a dashed line.

TH-2207_146107023

6.2.4 Numerical Settings

The simulations are run in transient mode using a first order explicit time marching scheme. A variable time step (Δt) based on a fixed Courant number of 0.25 is used for the momentum and pressure equations. This results in a typical time step of the order 10^{-6} s. The volume fraction equation is solved in an explicit manner with a Courant number of 0.25 and a piecewise linear interface construction (PLIC) algorithm is used to keep the interface sharp. The gradients of the variables are calculated using Green-Gauss node based gradient. QUICK scheme is used to discretize the momentum equations. The fractional step co-located scheme, in which the velocity and pressure are stored at the center of the cell, is used for pressure velocity coupling. A body force weighted interpolation scheme, which assumes the normal gradient of the difference between the body forces and pressure to be constant, has been used to compute the face pressures.

6.3 Results and Discussion

CFD simulations have been carried out in a channel of diameter d = 1 mm and channel length 10d. The bulk properties of air and water, the two working fluids are given in Table 6.1. The simulations have been run for a two-phase velocity of 0.3 m s^{-1}. This corresponds to a channel Reynolds number of 336. The simulations have been performed for two different sizes of spherical bubble – equivalent sphere radii of 0.92R (Case 1) and 0.96R (Case 2). The size of the Taylor bubble is ~1.25R for both the cases. The initial separation between the bubbles is 0.00650 m for Case 1 and 0.0040 m for Case 2.

TH-2207_146107023

Table 6.1: The gas and liquid properties used for bubble coalescence simulations (Leung *et al.*, 2014).

Properties	**Water**	**Air**
Density, $\boldsymbol{\rho}$ ($\mathbf{kg\ m^{-3}}$)	997.0	1.185
Dynamic viscosity, μ (**Pa s**)	89×10^{-5}	1.83×10^{-5}
Interfacial tension, $\boldsymbol{\sigma}$ ($\mathbf{N\ m^{-1}}$)	0.072	

Table 6.2: Details of simulations run

$(L_{slug}/D)_{t=0}$	L_{domain}	$R_{eqv,large}$	$R_{eqv.small}$
5.1	10d	1.25	0.92
3.6	10d	1.24	0.96

Following the guidelines laid out the Chapter 4, a computational mesh having 120000 cells with 1000 divisions in the axial direction has been used for the simulations.

6.3.1 Bubble approach

Initially the bubble shapes are specified to be spherical and capsular. After some time ($0.28s$ for Case 1, $0.31s$ for Case 2), the bubbles attain a steady shape and velocity. As the domain moves with the velocity of the Taylor bubble, the location of Taylor bubble in the domain remains unchanged whereas the spherical bubble approaches towards the Taylor bubble. Figure 6.2 (a) and 6.2(b) show the progression of bubble approach starting from the time when bubbles have attained

TH-2207_146107023

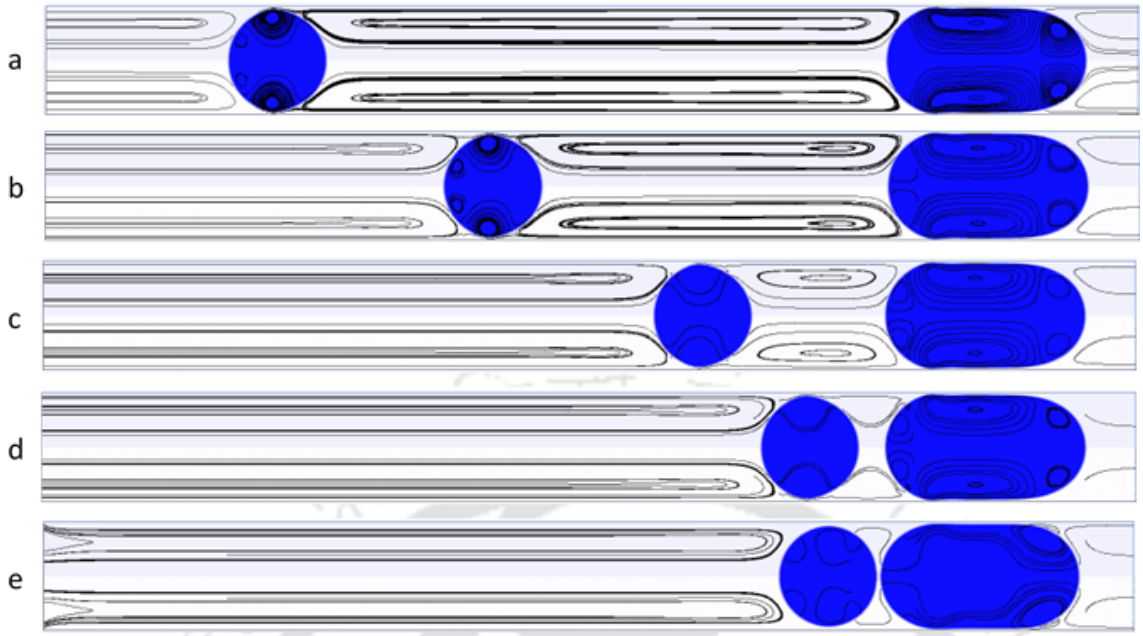

Figure 6.2(a): Bubble approach for $R_{eqv,s}$ = 0.92 for (a) t = 0s (5.1), (b) t = 0.08s (3.1), (c) t = 0.16s (1.2), (d) t = 0.2s (0.2), (e) t = 0.21s (0). L/d ratio shown in brackets.

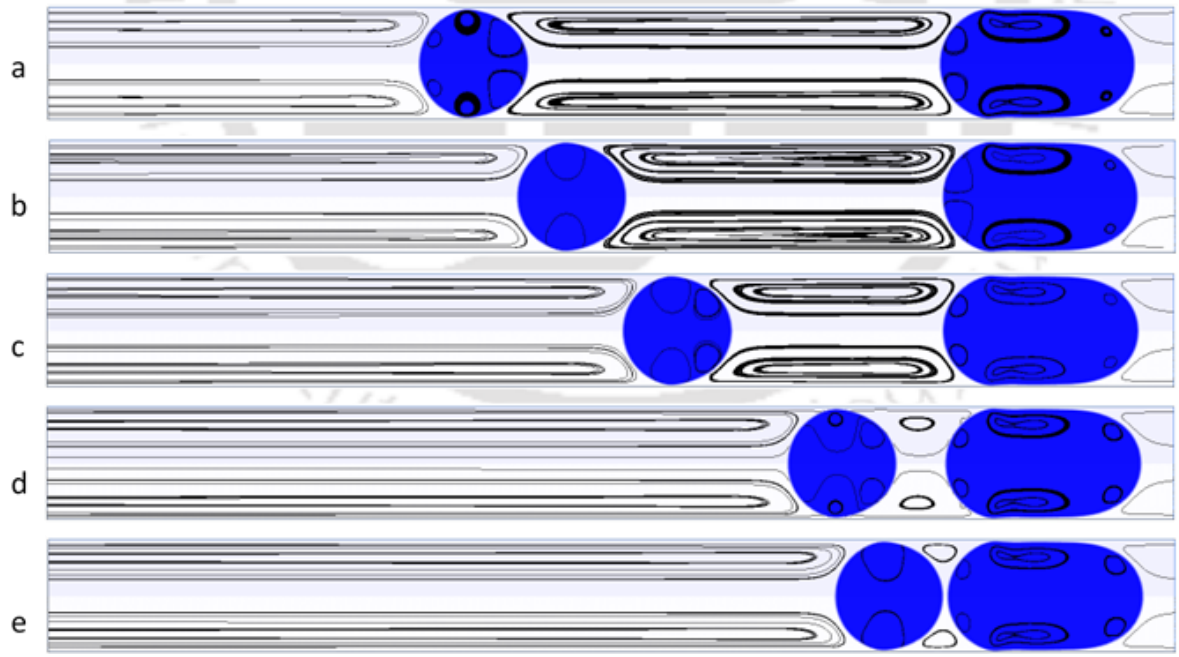

Figure 6.2(b): Bubble approach for $R_{eqv,s}$ = 0.96 for (a) t = 0s (3.6), (b) t = 0.15s (2.8), (c) t = 0.32s (1.9), (d) t = 0.56s (0.42), (e) t = 0.63s (0). L/d ratio shown in brackets.

TH-2207_146107023

a steady shape ($t' = 0$) to the time instants at which they reach the point of apparent contact for $R_{eqv,s} = 0.92$ (Case 1) and $R_{eqv,s} = 0.96$ (Case 2), respectively. At $t' = 0$, the two bubbles are separated by a distance of 5.1d for Case 1 and 3.6d for Case 2. The streamlines in a frame of reference moving with the Taylor bubble are also shown. During this period, the shape of the Taylor bubble remains unchanged. However, the front of the spherical bubble is flattened i.e. its radius of curvature increases as it approaches the Taylor bubble.

Figures 6.3 (a) and (b) show the variation of bubble velocities with time for case 1 and case 2, respectively. In both cases, as the smaller bubble approaches the larger one, there is a small but continuous increase in its velocity with time until the distance between the bubbles is more than 0.4d. Pinto and Campos (1998) observed this behaviour during the coalescence of gas bubbles rising in a flowing liquid inside a tube. In the laminar regime, it was seen that the velocity of the trailing bubble increased nearly by a factor of 1.8. Yuan and Prosperetti (1994) argued that during the in-line interaction of two bubbles, the drag experienced by the trailing bubble is lower than that experienced by the leading bubble, giving rise to a higher velocity for the trailing bubble compared to the leading one.

When the distance between the bubbles becomes small ($L/d \sim 0.4$), the velocity of the smaller bubble starts decreasing as it nears the Taylor bubble. Watanabe and Sanada (2006) arrived at a similar result while examining the existence of an equilibrium distance during the rise of a pair of bubbles. Such a behaviour was attributed to the "potential repelling force", previously predicted by Yuan and Prosperetti (1994).

TH-2207_146107023

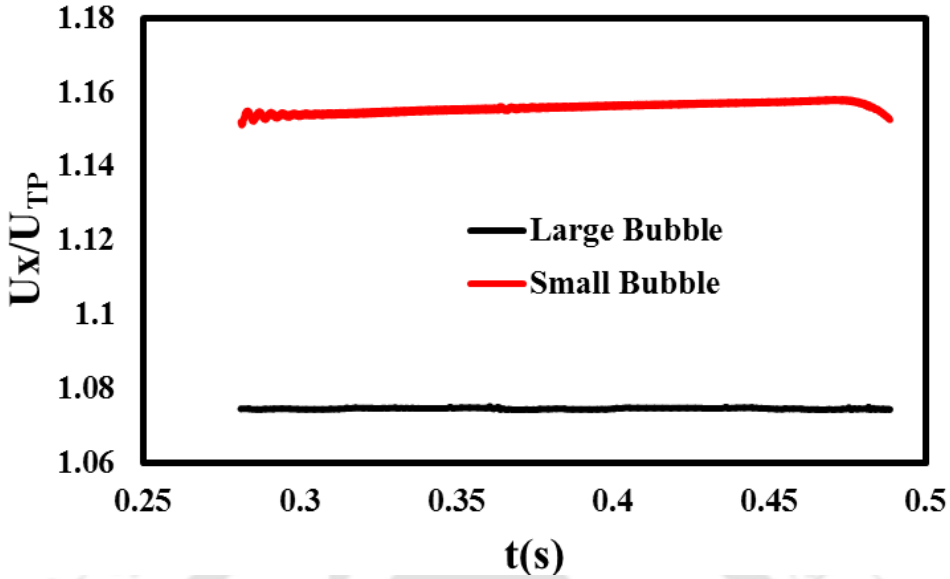

(a)

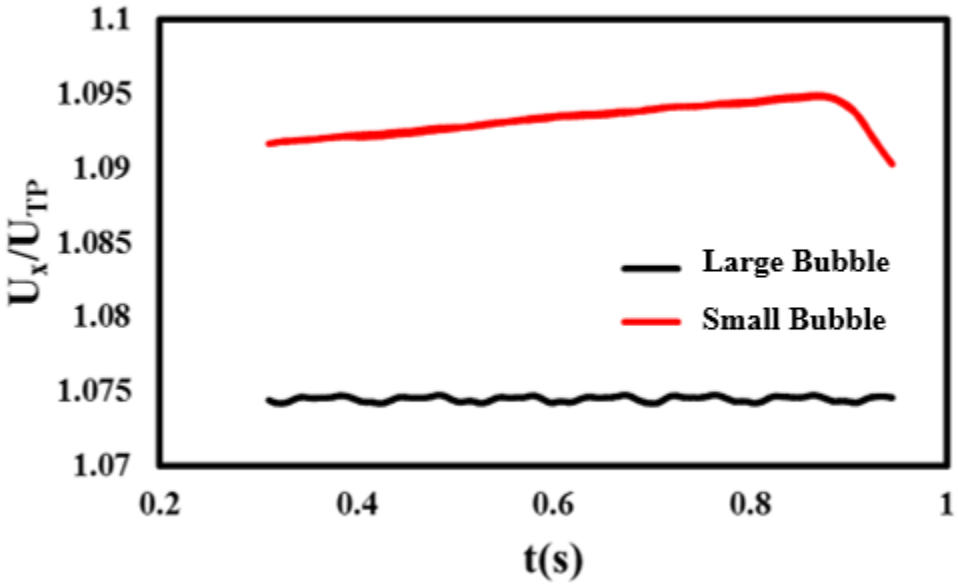

(b)

Figure 6.3: Velocity of bubbles during approach for (a) $R_{eqv,s}$ = 0.92 and (b) $R_{eqv,s}$ = 0.96.

The flow field inside the liquid slug plays a decisive role in determining the performance of a slug flow microreactor. The transverse flow near the interfaces contributes to the enhancement in mixing efficiency inside the liquid slug (Che *et al.* 2012). It can be seen from Fig. 6.2, that the

TH-2207_146107023

transverse or radial velocity in the liquid slug is negligible everywhere except near the nose and tail of adjacent bubbles. As the spherical bubble approaches the Taylor bubble, the length of the liquid slug between them becomes smaller and smaller. Consequently, the magnitude of the transverse velocity in the liquid slug increases. This can be clearly seen in Fig. 6.4 which shows the transverse velocity along the axial length in the liquid slug at a distance of $0.75R$ from the channel axis for both values of R_{eqv}. The minimum distance between the slugs (i.e. at the axis) has been assumed to be the slug length (L) and is different for each case.

For long liquid slugs ($L/d \geq 1.5$), the transverse component of velocity is close to zero across most of the axial distance of the slug ($0.2 \leq X/L \leq 0.8$), except at regions near the two bubbles. When the bubbles move closer ($L/d \leq 1$), significant amount of transverse velocities are observed across the length of the slug. Therefore, the flow inside the shorter slugs can lead to more efficient mixing of fresh fluid from the wall of the microchannel. The curvature at the rear of the Taylor bubble is smaller than the curvature of the front interface of the smaller bubble. This gives rise to a larger transverse velocity near the Taylor bubble compared to the smaller bubble.

It can be seen from the streamlines plotted in Fig.6.2 that the centre of recirculation zone in the liquid slug shifts away from the axis as the slug becomes smaller. Figures 6.5 (a) and (b) show the distance of the centre of recirculation zone from the axis for (a) $R_{eqv,s} = 0.92$ and (b) $R_{eqv,s} = 0.96$. The same pattern is observed in both in both cases. While $L/d \geq 1$, its distance from the axis remains nearly constant as the bubbles approach. A sharp change is observed for short slug lengths ($L/d < 1$), as the distance increases rapidly with the bubbles coming closer.

TH-2207_146107023

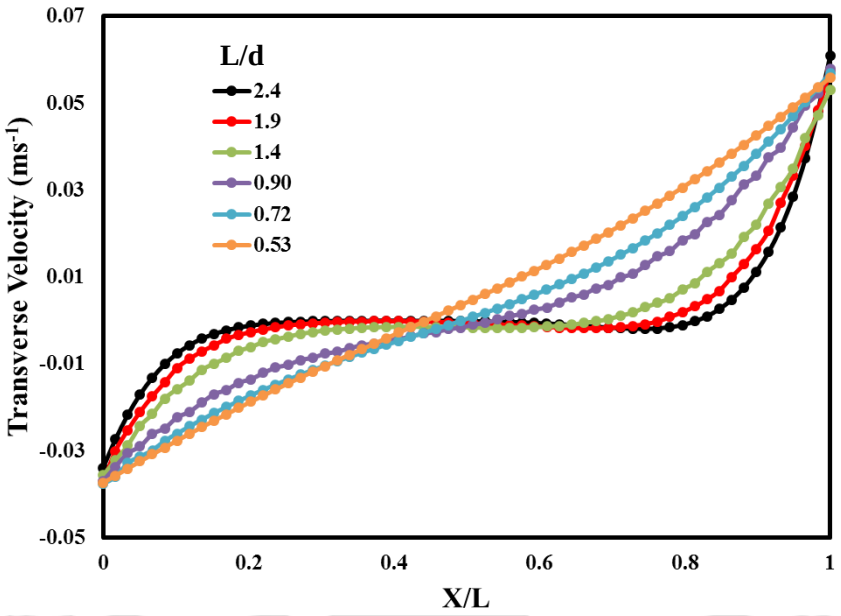

(a)

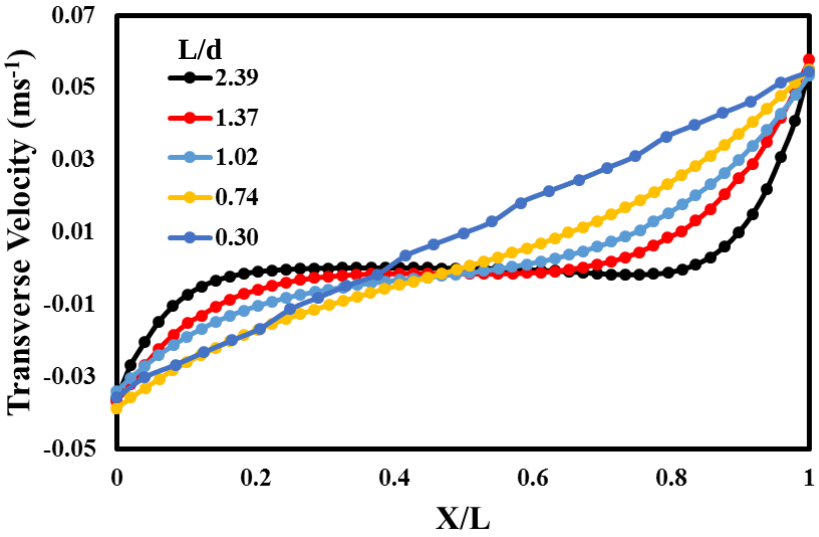

(b)

Figure 6.4: Transverse Velocity in the liquid slug at y = 0.75R for (a) $R_{eqv,s}$ = 0.92 and (b) $R_{eqv,s}$ = 0.96.

TH-2207_146107023

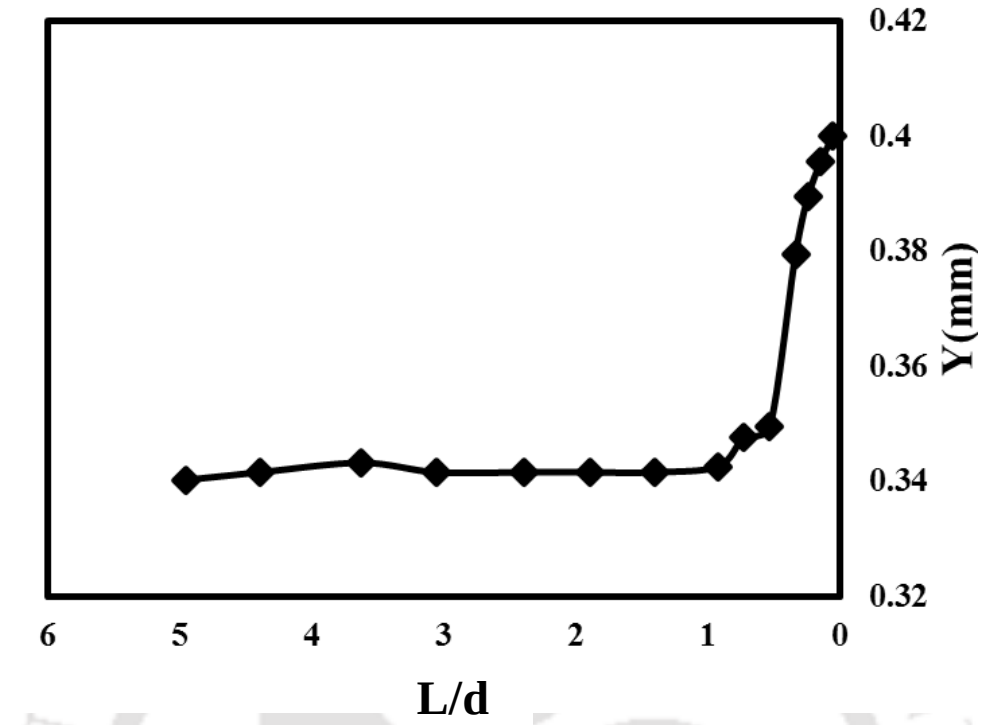

(a)

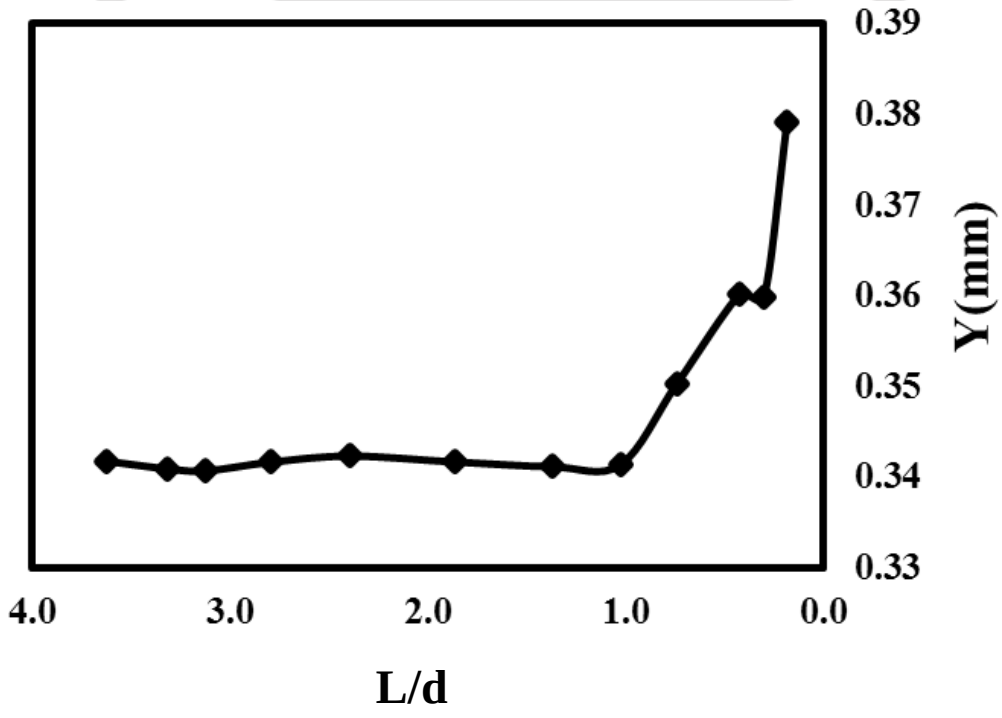

(b)

Figure 6.5: Distance from axis of centre of recirculation in the liquid slug for (a) $R_{eqv,s}$ = 0.92 and (b) $R_{eqv,s}$ = 0.96.

TH-2207_146107023

6.3.2 Coalescence

The contact between the two bubbles proceeds by the thinning of the liquid film between them under the effect of capillary force. When the film thickness gets reduced to the order of 10 nm, it undergoes spontaneous rupturing if the forces acting around the film do not equilibrate. However, the coalescence between the bubbles in the CFD simulation is dictated by the size of the grid elements in the coalescence region rather than the physics of the problem. Moreover, the present model does not consider the short range effects such as van der Waals forces, which may become important during coalescence. Therefore, the process of contact between the two bubbles has not been presented here. However, once this film is ruptured, the physics of the growth of newly formed bubble can be modelled accurately by the simulations.

6.3.3 Growth of Neck Radius

In the CFD simulations, as the two bubbles come into contact, a small amount of liquid sometimes appears within the gas bubbles. Which is not physically correct and is only a numerical artefact. Therefore, this small region of water is patched with air to accurately model the process of growth of the doublet, the unsteady shape of the newly formed bubble after the coalescence of the two bubbles, to a longer Taylor bubble.

Figure 6.6 shows the growth of the neck of air formed between the two bubbles ($R_{eqv,s} = 0.96$) after collision. The bubble interfaces come into contact at time $\tau = 0$. As shown in Figs 6.6 (a)-(d), the growth of the neck proceeds without affecting the shape of the rear of the doublet. Once, however, the radius of the neck (r) approaches $0.7R$, the rear starts to exhibit changes in its shape as can be observed in Figs. 6.6 (e)-(f). As the liquid near the neck drains further, the radius of the

TH-2207_146107023

neck grows at a much slower rate and the length of the doublet oscillates. Finally, the doublet assumes the shape of a Taylor bubble as shown in Fig. 6(h).

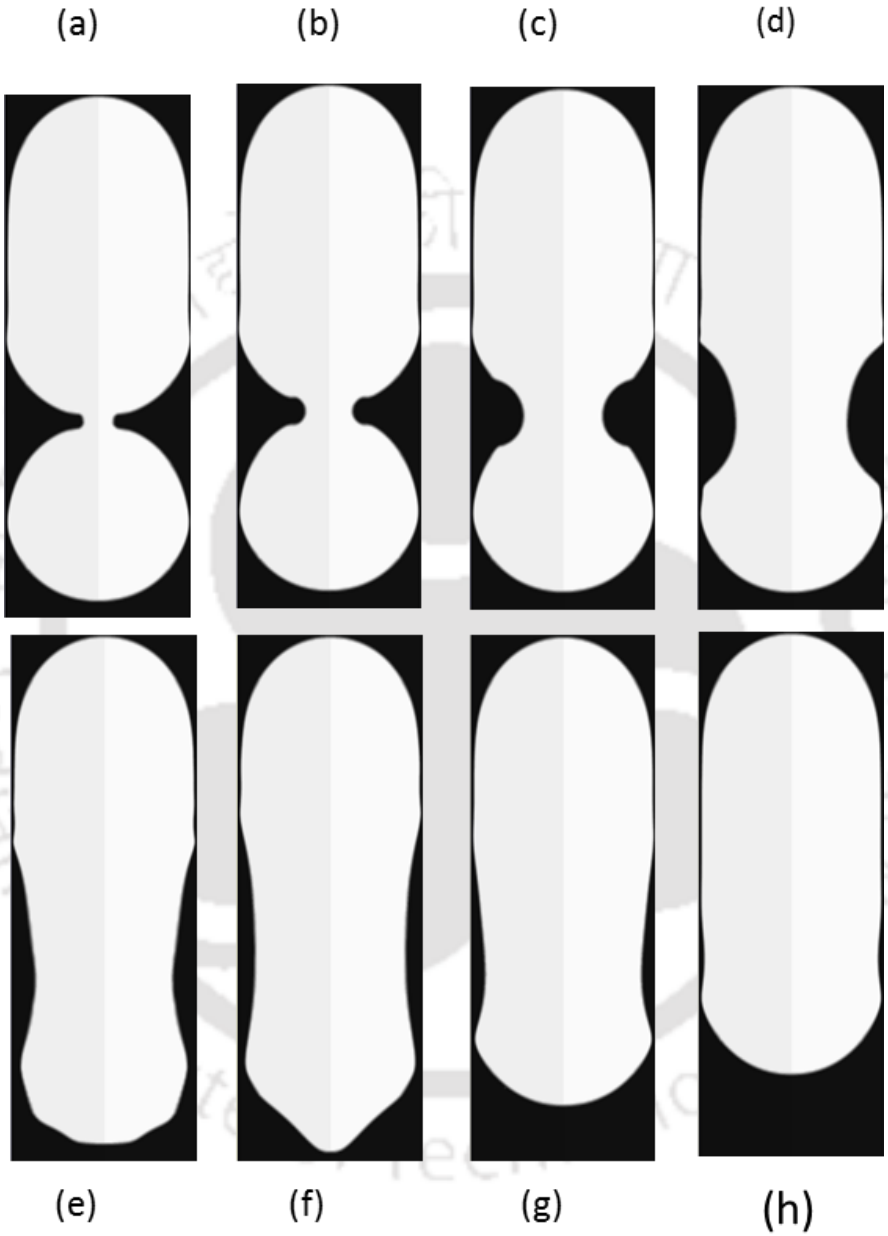

Figure 6.6: Progression of growth of neck formed between the air bubbles for $R_{eqv,s}$ *= 0.96. (a)* τ *= 0.00 ms (b)* τ *= 0.04 ms (c)* τ *= 0.14 ms (d)* τ *= 0.30 ms (e)* τ *= 0.70 ms (f)* τ *= 1.18 ms (g)* τ *= 4.30 ms (h)* τ *= 8.20 ms.*

TH-2207_146107023

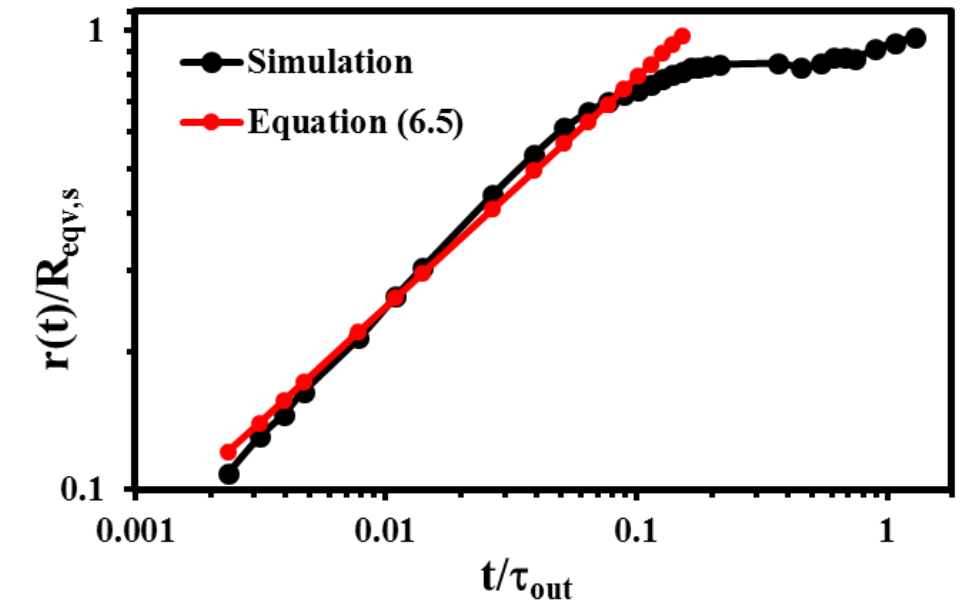

(a)

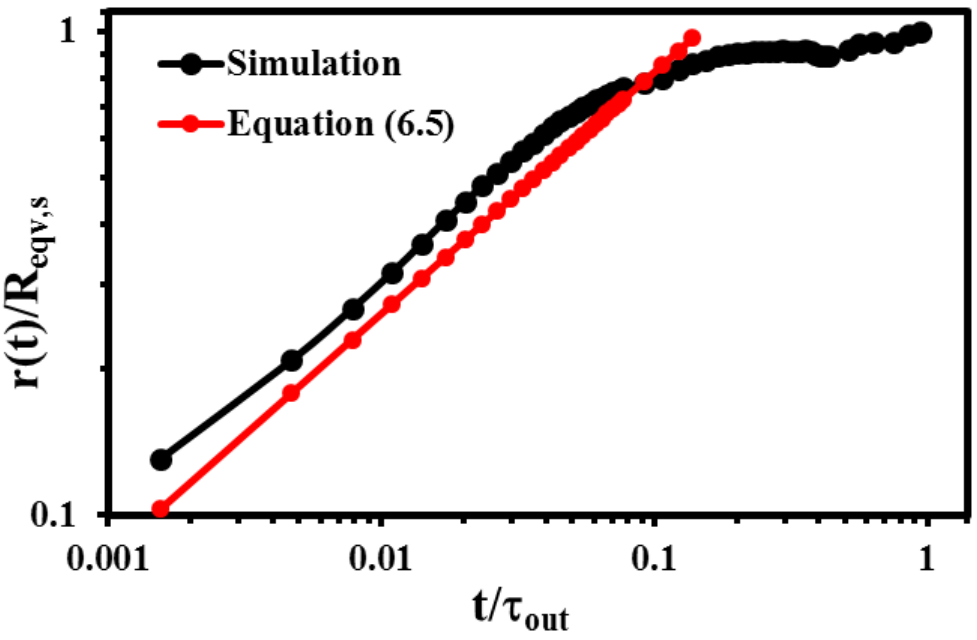

(b)

Figure 6.7: Growth of neck radius with time. Comparison of simulation results and values given by Eq (6.1) for (a) $R_{eqv,s}$ = 0.92 and (b) $R_{eqv,s}$ = 0.96.

TH-2207_146107023

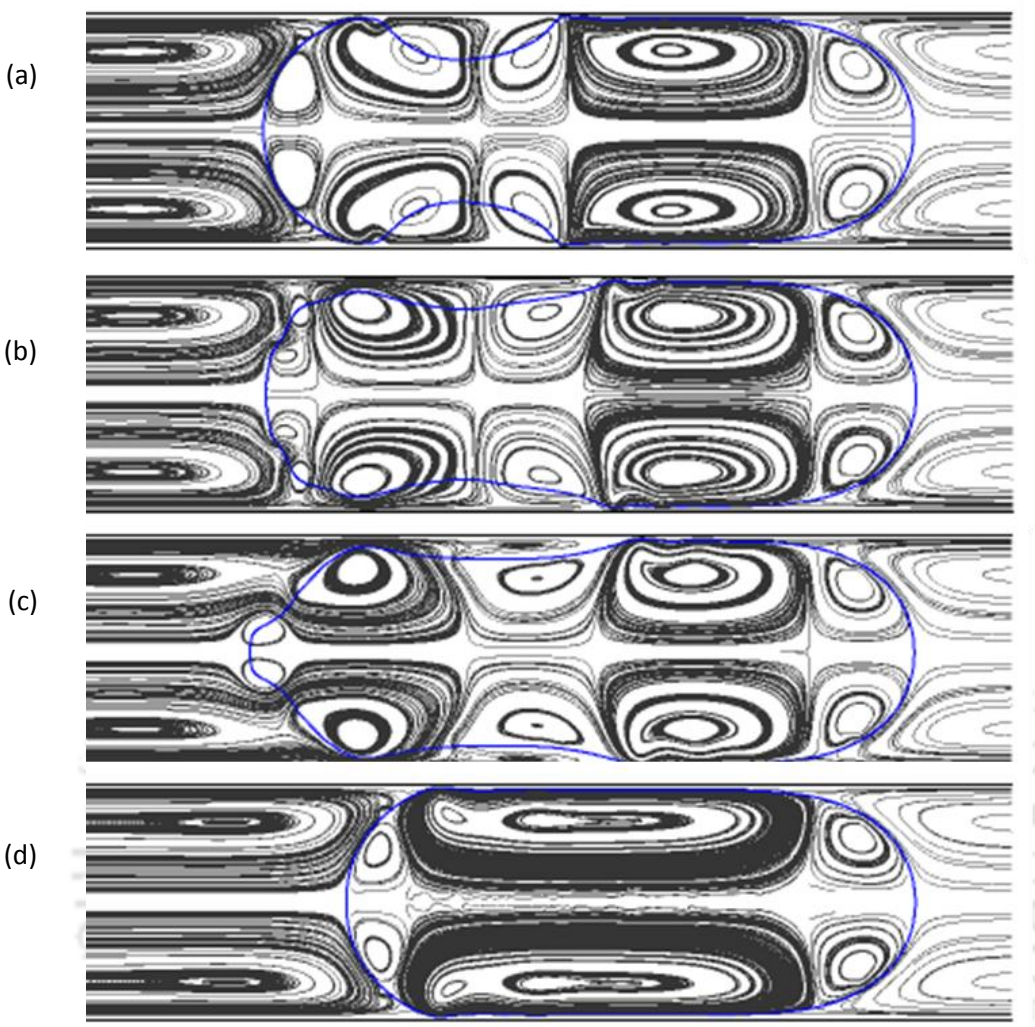

Figure 6.8: Streamlines inside the doublet during re-equilibration after collision for $R_{eqv,s}$ = 0.96. (a) τ = 0.30 ms (b) τ = 0.70 ms (c) τ = 1.18 ms (d) τ = 8.20 ms.

To study the speed with which the neck radius, $r(t)$, expands with time, the radius of the neck vs time is plotted in Figure 6.7. Paulsen *et al.* (2014) developed an expression for the growth of the neck radius by equating the viscous stresses and the Laplace pressure given by Eq. (2.7) for air-water system.

$$r(t)/A = 1.2\left(\frac{\sigma}{\mu_L A}\right)^{1/2} t^{1/2} \tag{6.5}$$

TH-2207_146107023

The neck radius growth as estimated from Eq. (6.5) has also been plotted in Fig 6.7 for comparison purpose. There is good agreement between the values obtained from the simulations and those obtained from Eq. (6.5) for the neck radii up to $r(t) = 0.8R_{eqv,s}$ and $r(t) = 0.7R_{eqv,s}$ for case 1 and case 2, respectively. Beyond this, the growth slows down, possibly due to the presence of the wall.

Figure 6.8 shows the streamlines in the bubble frame of reference inside the doublet during re-equilibration after collision. The flow behaviour in the liquid slug at the front of the bubble remains unchanged while the bubble takes a steady shape. However, changes in the flow field in the liquid slug at the back of the bubble are observed. Initially, ten vortices are observed in the bubble. With the change in bubble shape, the number of vortices are reduced to eight and finally, six vortices are observed inside the bubble when it attains a steady shape.

6.4 Conclusion

The coalescence of a short spherical and a long Taylor bubble flowing a continuous stream of liquid has been studied. A methodology to track the ends of the bubbles has been developed using the k-means clustering algorithm. This enables the study of the hydrodynamics in a frame of reference moving with the longer bubble. The results show that while the distance between the bubbles is greater than 0.4d, a slight increase in the velocity of the trailing bubble is observed as it approaches the leading bubble. However, no other change in the flow characteristic is observed. When the distance between the bubbles reduces to below one diameter, significant changes in the flow are observed.

TH-2207_146107023

The dynamics of the re-equilibration process after bubble collision was also studied. It was observed that during the initial stages of neck growth, the results agree with those of bubble coalescence in an outer fluid inside a sufficiently large container. However, once the radius grows to about three quarters the channel radius, the growth slows down due to the presence of the channel wall. Ten vortices are observed inside the doublet during the initial stages of re-equilibration process. Gradually these died out to give rise to a flow field similar to that observed during the "shear opposed penetration merging" of droplets. Finally the doublet acquired the shape of a Taylor bubble.

TH-2207_146107023

Chapter 7

Flow of Bubble in Channels with Sudden Area Change

TH-2207_146107023

CHAPTER 7

Flow of Bubble in Channels with Sudden Area Change

This chapter investigates the bubble dynamics caused by the sudden change in channel cross-sectional area. The cases of sudden increase in channel cross-sectional area i.e. sudden expansion, sudden decrease in cross-sectional area i.e. sudden contraction are considered. The bubble shape, bubble velocity, liquid flow field at the zone of area change and pressure drop in the channel are discussed.

7.1 Introduction

In recent decades, significant advances have been made in the development of micro-structured devices for applications in biomedical engineering, analytical chemistry, electronics cooling, chemical processing amongst others. Many such applications involve gas-liquid flow through the channel. Apart from flowing in the straight constant diameter channel, the flow also needs to pass through reducers and expanders in most of these devices as shown in Fig. 7.1 for a microreactor. The expansion and contraction in the reducer and expander can be sudden or gradual. It is therefore important to understand the flow behavior through reducer and expanders as they cause irreversible pressure loss, change in bubble shape and may also cause change in the flow regime.

In this work, the hydrodynamics of the channel-size bubbles in a millimeter-size circular channel has been studied computationally during sudden expansion and contraction using volume of fluid (VOF) method.

TH-2207_146107023

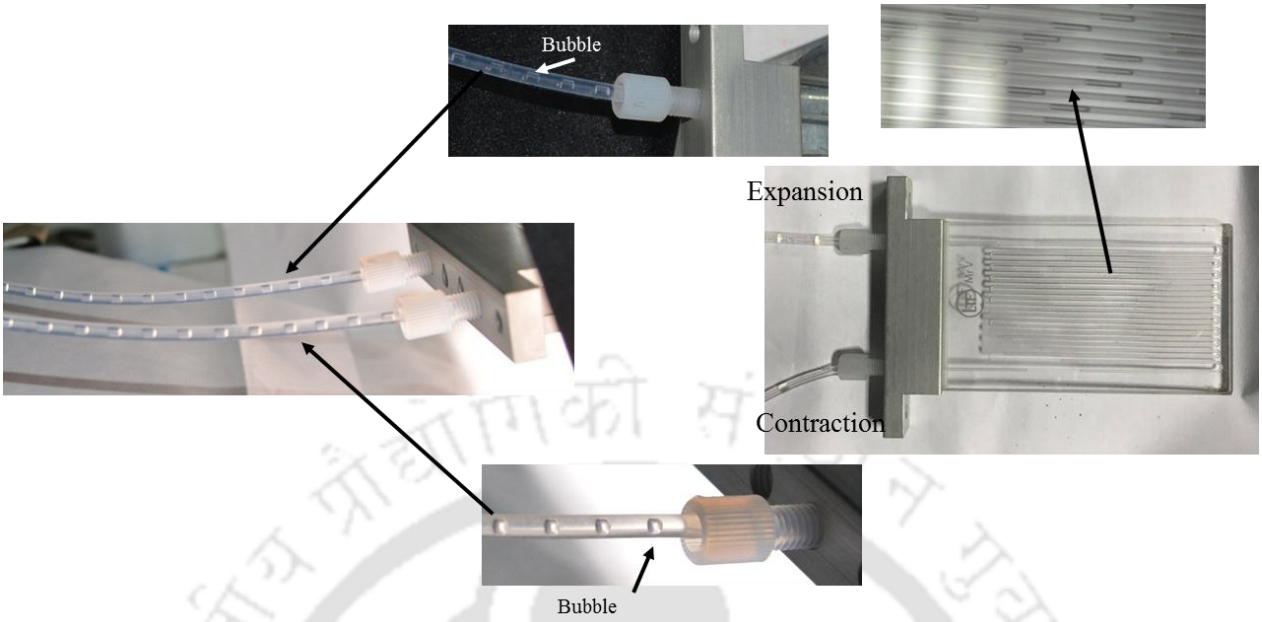

Figure 7.1 Example of expansion and contraction in a micro-reactor.

7.2 CFD Methodology

Transient CFD simulations have been performed in an axisymmetric computational domain for incompressible, Newtonian fluids. The volume of fluid (VOF) method has been used to capture the interface between the two phases.

As shown in Fig. 7.2, the computational domain consists of two channels having radii R_1 and R_2 ($R_1 < R_2$ for the case of expansion and $R_1 > R_2$ for the case of contraction) and lengths l_1 and l_2. A parabolic velocity profile having mean velocity equal to the mixture or two-phase velocity has been specified at the inlet boundary. A no-slip boundary condition has been specified at the channel wall. At the outlet, a constant pressure (gauge pressure of 0 Pa) has been specified.

First, the steady state solution is obtained for liquid-only flow. To initialise the gas-liquid flow, a capsular bubble of known volume having cylindrical middle and hemispherical ends is placed few

TH-2207_146107023

diameters away from the inlet boundary for the expansion case. For the case of contraction, the initial bubble shape is spherical.

The numerical schemes as described in Section 4.2.3 have been used to solve the governing equations.

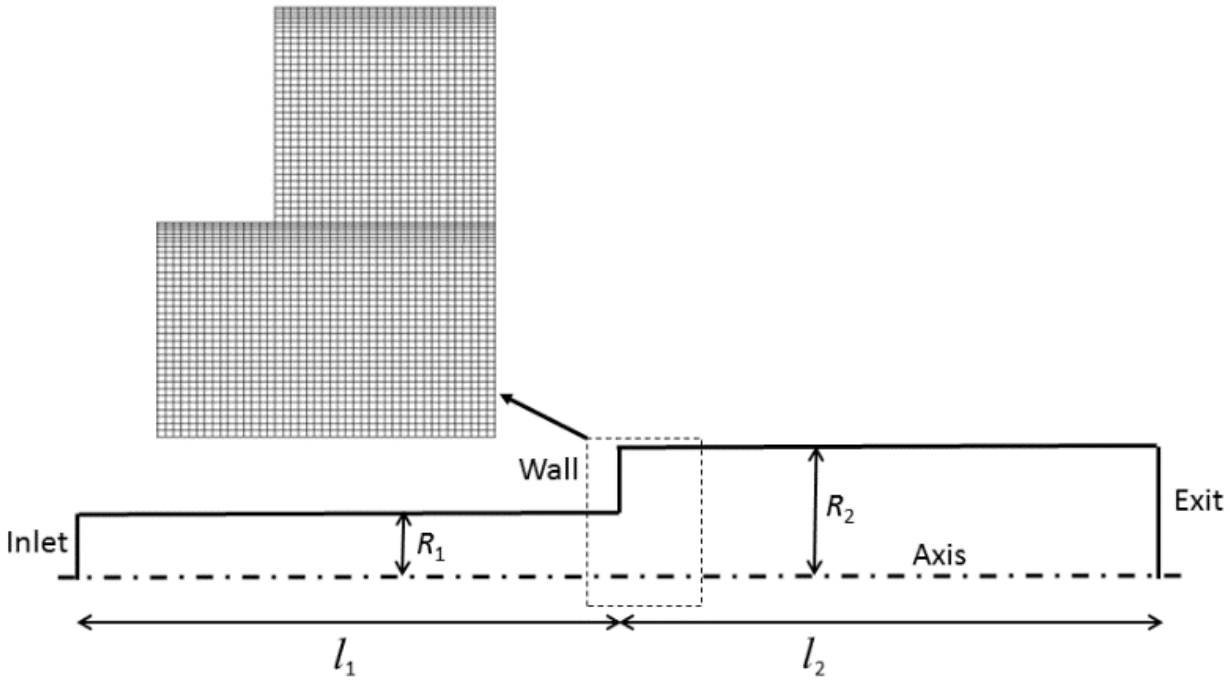

Figure 7.2: A schematic of the computational domain for sudden expansion ($R_1 < R_2$). The mesh distribution in the zone of area change is also shown.

A structured mesh is used for the simulations and the mesh distribution at the expansion/contraction zone is shown in Fig. 7.2. The mesh has been sufficiently refined near the wall of small diameter channel so as to capture the thin liquid film surrounding the bubble following the guidelines laid out by Gupta *et al.* (2009) and described in Chapter 4. Preliminary simulations showed that extra care is required to capture the liquid film between the wall and

TH-2207_146107023

bubble at the sharp corner. In fact, a liquid of high viscosity has been chosen so as to capture the liquid film. After a grid refinement study, the total number of elements in the domain are 58,800.

7.3 Results and Discussion

Air and ethylene glycol have been used as the gas and liquid phases in the CFD simulations. The properties of the two fluids are given in Table 7.1. The flow conditions and relevant non-dimensional numbers for all the cases are given in Table 7.2.

Table 7.1: Properties of the fluids used in the simulations (Leung *et al.*, 2014)

Properties	**Ethylene Glycol**	**Air**
Density ($kg\ m^{-3}$)	1111.4	1.185
Dynamic Viscosity ($kg\ m^{-1}\ s^{-1}$)	0.0157	1.83×10^{-5}
Surface Tension ($N\ m^{-1}$)	0.048	

Table 7.2: Input parameters and relevant non-dimensional numbers for different cases simulated

	Expansion		**Contraction**	
	Case 1	Case 2	Case 1	Case 2
U_{TP1} ($m\ s^{-1}$)	0.6	0.6	0.075	0.15
U_{TP2} ($m\ s^{-1}$)	0.15	0.066	0.3	0.6
Re_1	424	424	108	212
Re_2	212	140	212	424

TH-2207_146107023

ε_G	0.026	0.013	0.026	0.026
R_{eqv}	0.73	0.579	0.73	0.73
Ca	0.196	0.196	0.024	0.049
d_1 (mm)	1	1	2	2
d_2 (mm)	2	3	1	1
l_1 (mm)	10	10	10	10
l_2(mm)	10	10	10	10

7.3.1 Sudden Expansion

The case of sudden expansion is considered for the expansion ratios (d_2/d_1) of 2 and 3. The diameter of the smaller channel (d_1) is 1 mm and the mixture velocity at the inlet is 0.6 m s^{-1} for each case. Reynolds number in the small diameter channel in both the cases is 424.

Figure 7.3 shows the pressure contour and streamlines for the expansion ratio 2 for liquid-only flow. The pressure decreases linearly in the smaller channel and increases as the flow expands and decelerates in the larger channel. Once the flow becomes fully-developed in the larger channel downstream of the area change zone, it again decreases linearly but the slope is very small when compared with that in the smaller channel. A small recirculation is observed at the corner in the larger channel. The overall pressure drop in the channel is 3026 Pa. The pressure drop in the smaller channel is 3004 Pa and in the larger channel is 20 Pa only.

At time t = 0, a capsular bubble having non-dimensional equivalent spherical radius 0.73 (based on the smaller channel diameter) is patched near the inlet. The bubble starts moving along the flow

TH-2207_146107023

direction from left to right and achieves a steady shape. The change in bubble shape with time has been shown in Fig. 7.4.

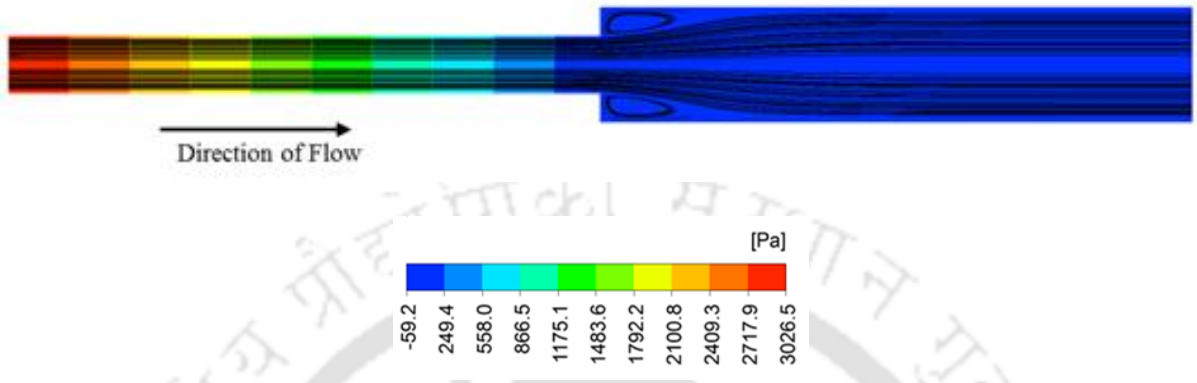

Figure 7.3: Pressure distribution and streamlines for the liquid-only flow in a channel having sudden expansion from 1 mm diameter to 2 mm diameter for a mean velocity of 0.6 m s^{-1} in the 1 mm diameter channel.

The bubble achieves a steady velocity after about 0.0051 s as can be seen from Fig. 7.5. At this time, the bubble nose is 2.55 mm away from the expansion zone. When the bubble approaches the expansion zone, it starts expanding radially and does not remain capsular any longer. Figure 7.6 shows the fraction of the channel cross-section occupied by the gas bubble at a distance of 0.5 mm in the 2 mm section from the location of area change. Initially, the bubble expands linearly with time and the rate of bubble growth decreases with time. The maximum is observed when the section of the bubble having largest radius pass through it and then the remaining bubble at the rear pass quickly resulting in the gas volume fraction at the cross-section to become zero again.

Once the entire bubble comes out of the channel, its radius further grows and the bubble shortens in the axial direction (0.0102 s- 0.013 s).

TH-2207_146107023

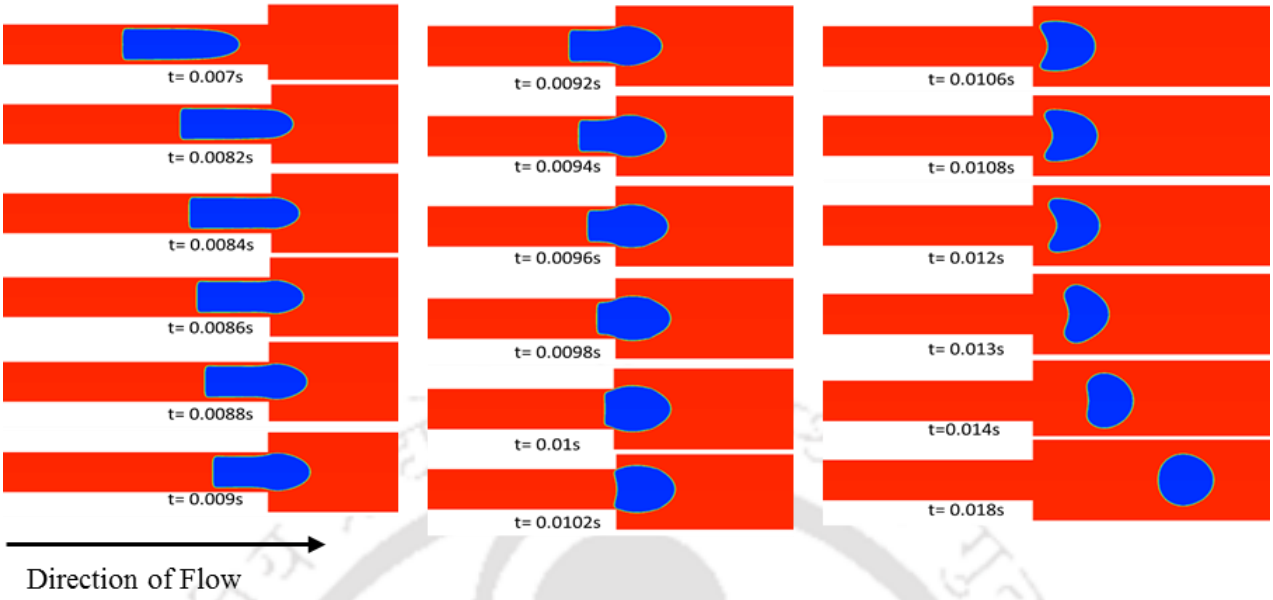

Figure 7.4: Evolution of the bubble shape in channel having sudden expansion zone from 1 mm diameter to 2 mm diameter for a mixture velocity of 0.6 m s^{-1} in the 1 mm diameter channel.

As can be seen in Fig. 7.5, the bubble velocity reaches a minimum value when the bubble comes out of the small diameter channel. The dip in bubble velocity corresponds to the maxima in the pressure drop, shown in Fig. 7.7.

The bubble shape remains transient in the expansion zone before it takes a steady shape in the bigger channel. As the bubble leaves the smaller channel, the bubble tail takes a concave shape. This is caused by the high liquid-side pressure at the back of the bubble when it comes out of the small diameter channel. In the expanded channel, the bubble takes a steady shape (as shown at 0.018 s in Fig. 7.4). The steady bubble shape is nearly spherical.

TH-2207_146107023

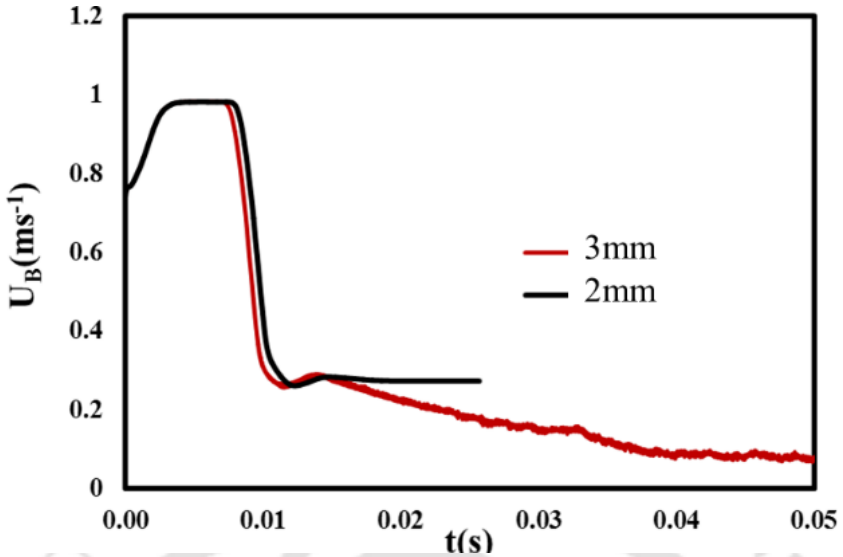

Figure 7.5: Bubble velocity as a function of time during flow of a bubble in a suddenly expanding channel from a channel of 1 mm diameter to 2 and 3 mm diameter channels for a mixture velocity of 0.6 m s^{-1} in the 1 mm diameter channel. The legend shows the diameter of the larger section.

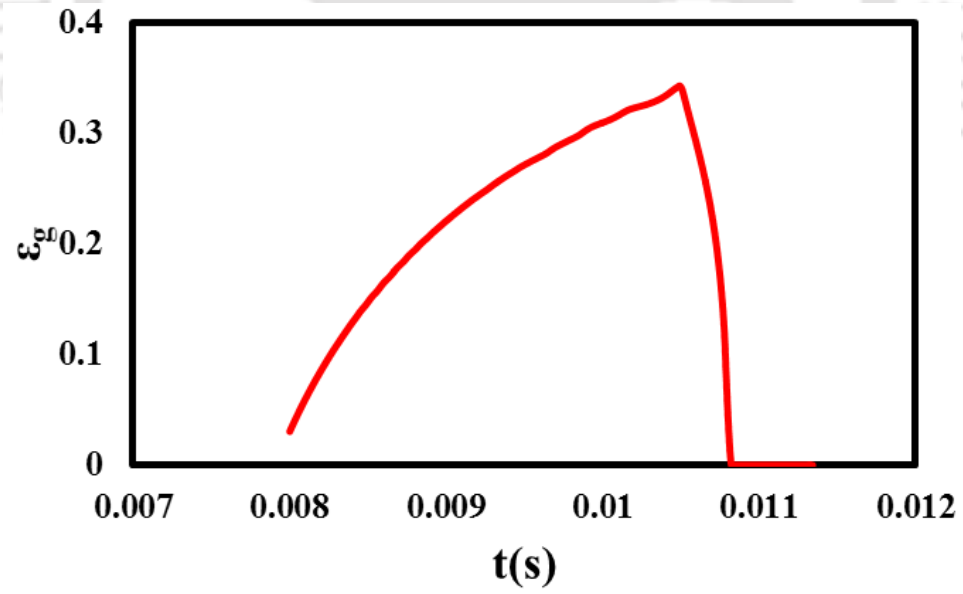

Figure 7.6: Area-averaged gas volume fraction over a cross section as a function of time in 2 mm diameter section at a distance of 0.5 mm from the location at which the channel cross-sectional area changes for the flow conditions shown in Fig. 7.4.

TH-2207_146107023

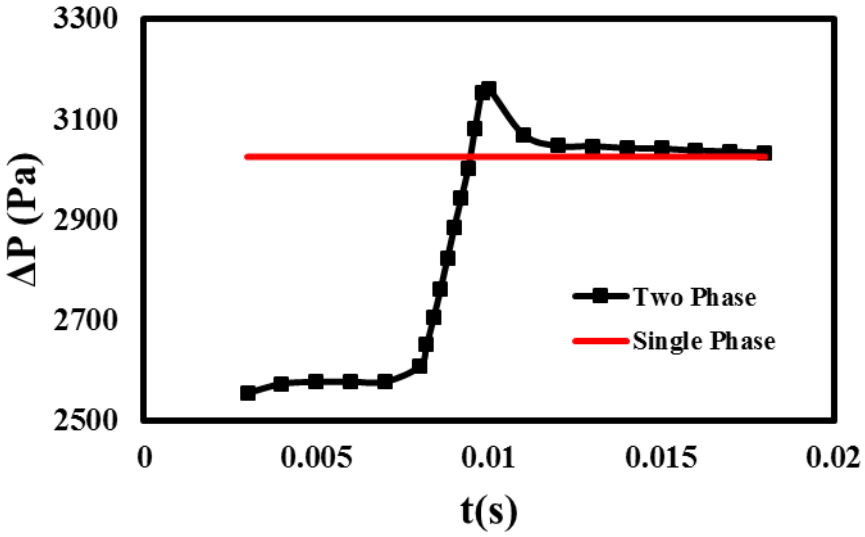

Figure 7.7(a): Variation of the pressure drop across the channel with time during the flow of bubble in channel of 1 mm expanding to a 2 mm diameter channel for a mixture velocity of 0.6 m s^{-1} in the 1 mm diameter channel. The solid horizontal line indicates the pressure drop for a liquid-only flow at the same flow conditions.

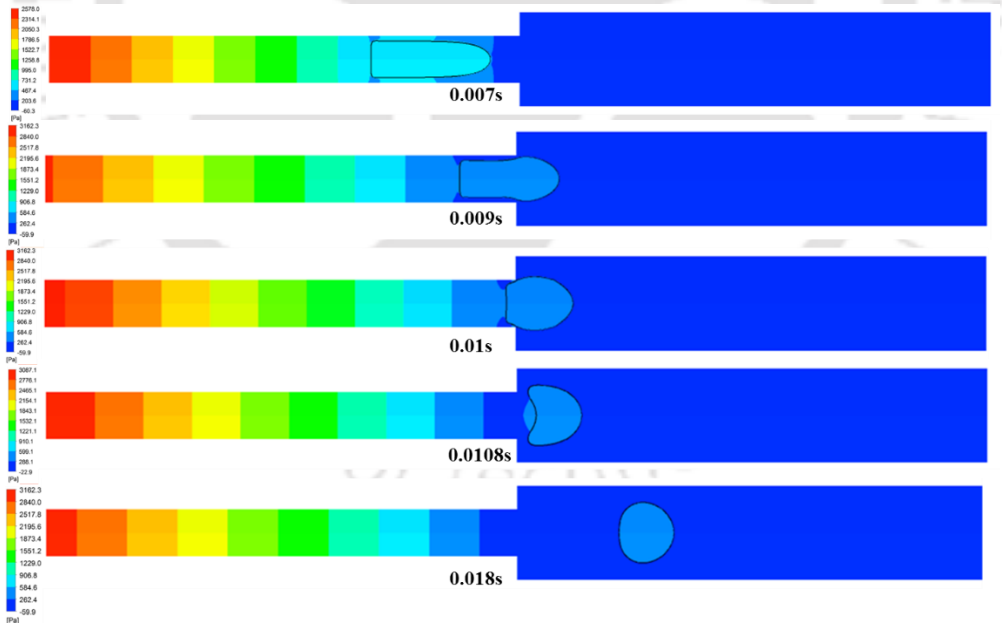

Figure 7.7(b): Contours of pressure in a channel having sudden expansion from 1 mm diameter to 2 mm diameter for a mixture velocity of 0.6 m s^{-1} in the 1 mm diameter section.

TH-2207_146107023

Figure 7.7 shows the pressure drop across the channel with time. When the bubble is in the small diameter channel, the pressure drop is ~ 2550 Pa, significantly lower than that for liquid-only flow. At about 0.01 s, when the bubble ejects from the small diameter channel, the pressure drop increases and reaches to a maximum value. As the bubble moves downstream in the larger diameter section, the pressure drop decreases and approach the same value as for the liquid-only flow.

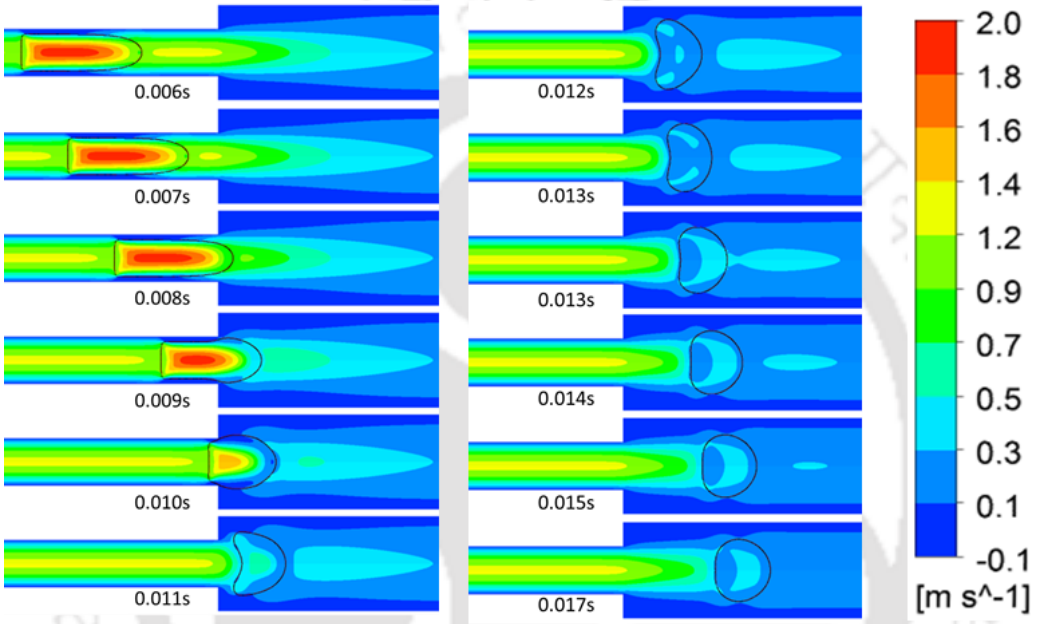

Figure 7.8: Contours of velocity magnitude in a channel having sudden expansion from 1 mm diameter to 2 mm diameter for a mixture velocity of 0.6 m s^{-1} in the 1 mm diameter section.

Figure 7.8 shows the contours of velocity magnitude at different time instants. It is apparent that the Taylor-shaped bubble in the smaller channel causes significant pressure drop whereas there is little effect of the spherical bubble on the pressure drop.

When the expansion ratio is increased to 3, the bubble shape and velocity in the smaller diameter channel remains almost same. Fig. 7.9 shows a comparison of the steady bubble shapes obtained in the bigger sections for the section diameter of 2 mm and 3 mm. As shown in Fig. 7.5, it takes longer for the bubble to achieve a steady velocity in the large diameter channel. The ratio of bubble

TH-2207_146107023

velocity for 2 mm diameter with 3 mm diameter is 3.25 whereas the ratio of two-phase velocities in the two channels is 2.25 only.

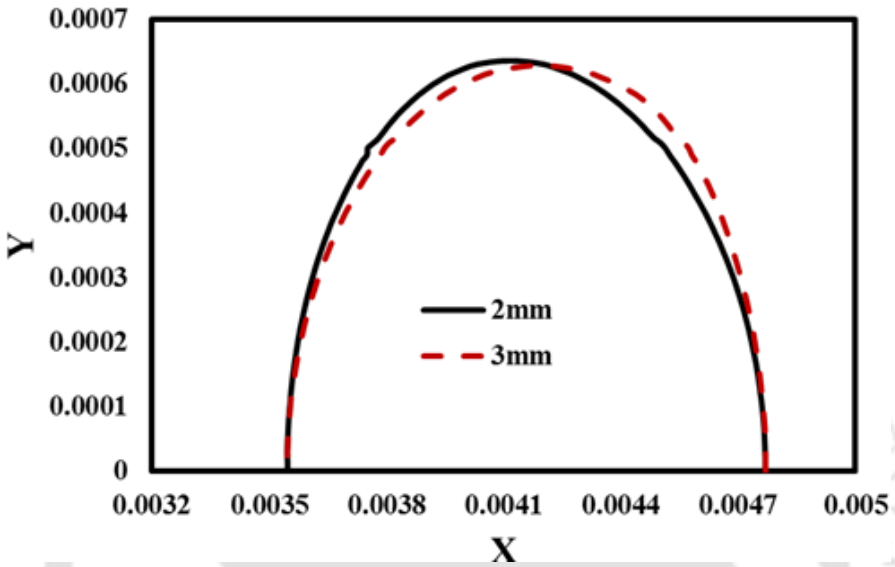

Figure 7.9: Comparison of the steady bubble shapes obtained in the larger sections of diameter 2 and 3 mm in the channels having sudden expansion. Smaller channel diameter is 1 mm in each case.

For the CFD simulations performed in this chapter, effect of gravity has not been taken into account. The Bond number for a 1 mm diameter channel for nitrogen-ethylene glycol system, gas-liquid combination used in this work, is 0.22, whereas for 2 mm diameter channel the value of Bond number is 0.88. A case was simulated considering the effect of gravity for vertically upward flow (gravity acting in a direction opposite to the flow) in the channel having sudden expansion from 1 mm to 2 mm channel diameter. Figure 7.10 shows the comparison of bubble velocity obtained from CFD simulations for the two cases when effect of gravity is taken into account and not taken into account, all other conditions being same. While there is no difference in the bubble velocity in the small diameter section, a small difference between the bubble velocities for the

TH-2207_146107023

cases considering and neglecting gravity can be clearly seen in the large diameter section. The buoyancy effect caused by considering the effect of gravity, causes a small increase (0.021 m s^{-1} and 7% increase) in the bubble velocity.

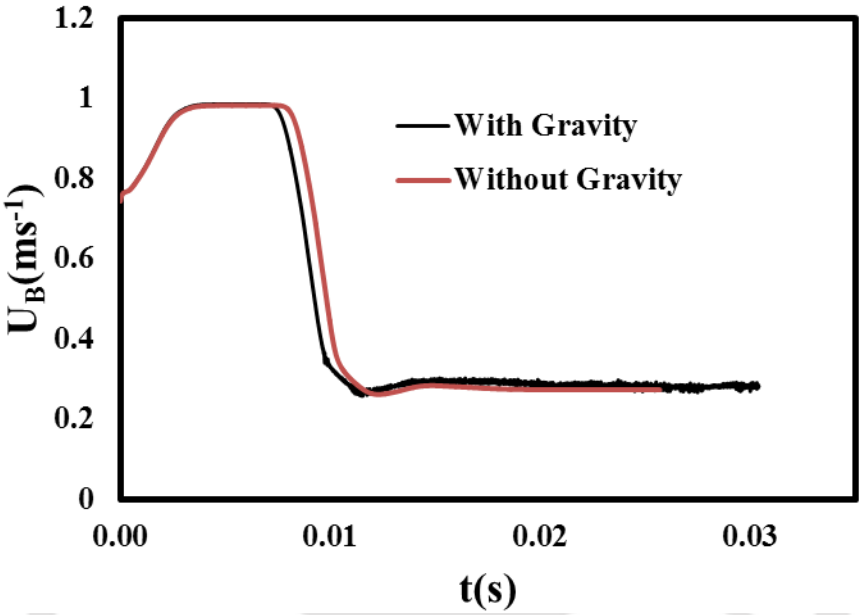

Figure 7.10: Bubble velocity with gravity and without gravity as a function of time magnitude in a channel having sudden expansion from 1 mm diameter to 2 mm diameter for a mixture velocity of 0.6 m s^{-1} in the 1 mm diameter section.

7.3.2 Sudden Contraction

The case of sudden contraction has been considered for the diameter ratio (d_1/d_2) of 0.5. The diameter of the smaller channel is 1 mm. The simulations have been performed for two cases having the mean velocities of 0.075 and 0.15 m s^{-1} at the inlet. These corresponds to a mean velocities of 0.3 and 0.6 m s^{-1}, respectively, in the smaller diameter section.

As for the case of expansion, first the simulations have been performed for the liquid-only flow. Figure 7.11 shows the pressure contours and streamlines for liquid-only flow in the contracting

TH-2207_146107023

channel. The total pressure drop in the channel is 3893 Pa, about 29% more than that in the expanding channel having same diameter ratio and section lengths. The pressure drop in the larger diameter section is 316 Pa and in the smaller diameter section is 3577 Pa. Whereas, for Hagen-Poiseuille flow, the pressure drop in large channel is 188 Pa, and small channel is 3014 Pa, giving an overall pressure drop of 3202 Pa.

For gas-liquid flow, the simulation is run in the transient mode and initialised with the velocity for liquid-only flow and patching a spherical bubble having non-dimensional equivalent spherical radius of 0.73 (non-dimensionalised by the larger channel diameter) near the inlet.

Figures 7.12 and 7.13 show the evolution of bubble shape and velocity with time, respectively. The steady bubble shape in the large diameter section is almost spherical (t = 0.0057 s) and attains a steady velocity of 0.273 m s^{-1}. As the bubble approaches the contraction zone, its nose becomes pointed. The part of the bubble that has entered the small diameter section starts elongating and evolves to take the shape of the front of a Taylor bubble. When the bubble enters the channel completely in the small diameter section, it takes the shape of a Taylor bubble. The bubble velocity when the bubble shape becomes steady is 0.981 m s^{-1}. The ratios of bubble and two-phase velocity in the larger and smaller diameter sections are 1.83 and 1.63, respectively. The values are the same as in the suddenly expanding channel in the smaller and larger diameter sections.

Sudhakar and Das (2018) investigated the change in the shape of a liquid droplet in a vertical channel having sudden contraction using lattice Boltzmann method (LBM) for the cases when the droplet shape is symmetric and asymmetric. Changes in the bubble shape observed in this work are similar to those observed for the symmetric droplet. Similarly, Kawahara *et al.* (2015) observed the elongation of the bubble on entering the smaller channel experimentally as well as numerically. They also found the bubble velocity to be larger in the smaller channel as observed in this work.

TH-2207_146107023

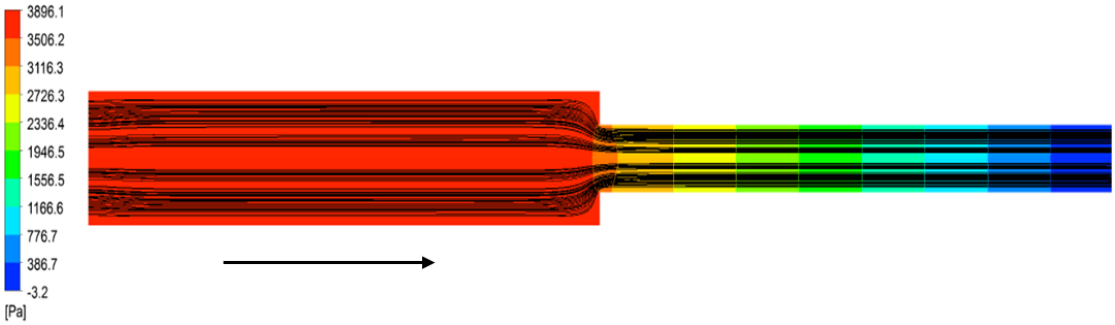

Figure 7.11 Streamlines and pressure contour plot for the contraction ratios (0.5) for liquid-only flow. The diameter of the larger section is 2 mm and smaller section is 1 mm.

Figure 7.12: Evolution of the bubble shape in a channel of 2 mm diameter having sudden contraction to a channel of 1 mm diameter for a mixture velocity of 0.6 m s^{-1} in the 1 mm diameter channel.

Figure 7.14 shows the variation of pressure drop in the channel with time. When the bubble is in the large diameter channel, the pressure drop is ~3650 Pa whereas the pressure drop is reduced to ~3250 Pa.

TH-2207_146107023

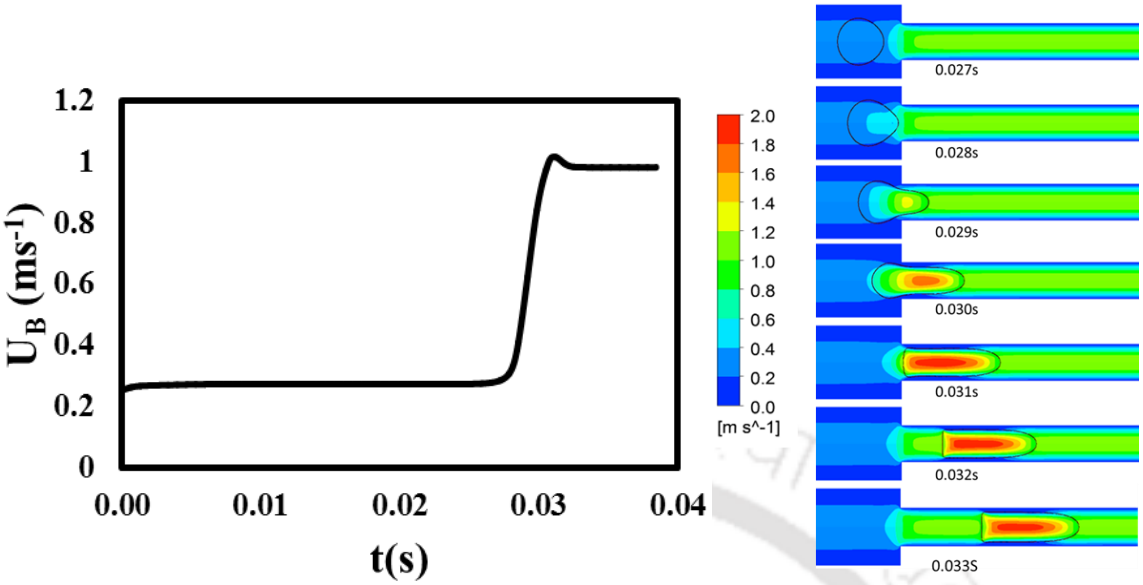

(a) (b)

Figure 7.13: (a) Bubble velocity as a function of time during flow of a bubble in a suddenly contracting channel from a channel of 2 mm diameter to 1 mm diameter channel for a mixture velocity of 0.6 m s^{-1} in the 1 mm diameter channel. (b) Contour plot of velocity magnitude with different time instant throughout the channel.

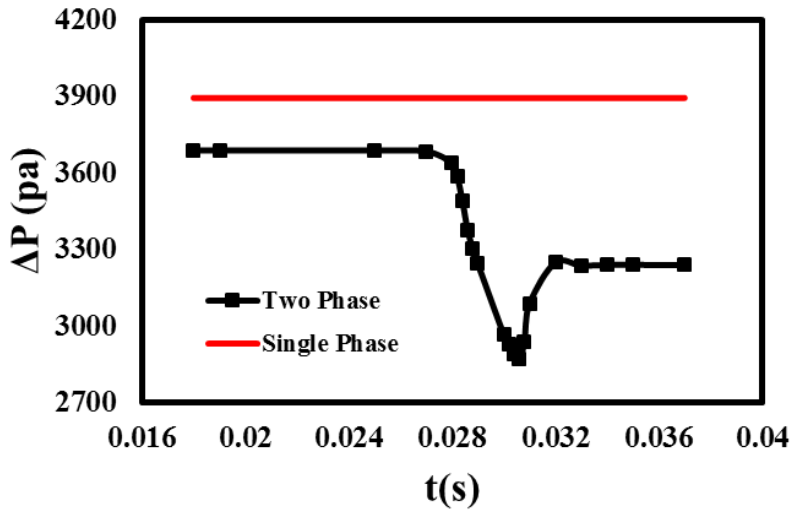

Figure 7.14: Variation of the pressure drop across the channel with time during the flow of bubble in channel of 2 mm contracting to a 1 mm diameter channel for a mixture velocity of 0.15 m s^{-1} in

TH-2207_146107023

the 2 mm diameter channel. The red solid line indicates the pressure drop for a liquid-only flow at the same flow conditions.

At about 0.026 s, when the bubble near the contraction to smaller diameter channel, the pressure drop decrease and reaches to a minima value. As the bubble moves upstream in the small diameter channel, the pressure drop increases and having value 3577 Pa.

7.4 Conclusion

CFD simulations have been performed to understand the bubble dynamics in a channel having sudden change in diameter for the case of increase in channel diameter as well as decrease in the channel diameter. For both the cases, the bubble volume is chosen such that the bubble is spherical in the larger channel and bullet-shaped in the smaller channel. The evolution of the bubble shape and pressure drop during the period when the bubble passes through the contraction/expansion zone has been studied. The pressure drop is observed to decrease significantly when the bubble has a cpasular shape whereas the pressure drop is close to that for single phase flow when the bubble is spherical.

TH-2207_146107023

Chapter 8
Pulsatile Taylor Flow

TH-2207_146107023

CHAPTER 8

Pulsatile Taylor Flow

In this chapter, the hydrodynamics and heat transfer for gas-liquid pulsatile Taylor flow in a microchannel is studied numerically. The effect of frequency on bubble velocity, wall shear stress, pressure drop and Nusselt number are reported.

8.1 Introduction

In several instances of gas-liquid slug flow in microchannels, the flow may not be steady. Two such examples are pulsatile heat pipes (Das *et al.*, 2013) and instability during flow boiling in microchannels (Bogojevic *et al.*, 2013). It is therefore important to understand the effect of the pulsatile behaviour on the hydrodynamics and heat transfer in slug flow regime in microchannels.

A steady slug flow has a characteristic frequency i.e. bubble frequency $f_B = L_{UC}/U_B$. However, as the bubble frequency is not known a priori, two-phase velocity can be used to estimate an approximate value of bubble frequency i.e. $f_B \approx L_{UC}/U_{TP}$. For the pulsatile flow, the flow rate of at least one of the phases oscillates which may cause the generation of bubbles of different lengths periodically. Therefore, there are two characteristic frequencies in the pulsatile slug flow. In this work, flow and heat transfer in a unit cell consisting of a single bubble subjected to time-dependent liquid flow has been investigated for a range of frequencies of the liquid flow.

8.2 Computational Methodology

In chapters 4 and 5, a computational methodology to model steady, periodic slug flow and heat transfer in the bubble frame of reference has been described. The same methodology has been

TH-2207_146107023

adapted to model pulsatile slug flow. The changes made in the methodology are described in this section.

The boundary condition at the inlet is specified such that the flow rate varies sinusoidally and the axial velocity profile is parabolic as given by Eq. (8.1).

$$v_{x,in} = 2\left(U_{Mean} + U_{Amp}\, cos\left(\omega(t - t_{ini})\right)\right)\left(1 - \frac{r^2}{R^2}\right) \tag{8.1}$$

Where U_{Mean} is the mean two-phase velocity over a cycle, U_{Amp} is the velocity amplitude, ω is the angular frequency and t_{ini} is the time at which the pulsatile flow is initialised.

As the velocity field is unsteady, momentum and energy equations are solved simultaneously. To obtain a periodic temperature field, a modified temperature profile is wrapped from the computational faces having flow out of the domain to the corresponding faces where flow enters the domain.

The solution obtained for flow, volume fraction and temperature fields for the steady flow is used as the initial guess for the pulsatile flow simulations.

8.3 Result and Discussion

The simulations have been performed in a channel of radius 0.5 mm and unit cell length 5 mm for air-water flow in the channel. The same mesh as used for steady simulations presented in Chapters 4 and 5, has been used for the pulsatile flow. The properties of the air and water used in the simulations are given in Table 8.1. The non-dimensional equivalent sphere radius is 1.31 and the gas volume fraction in the unit cell is 0.3. The mean two-phase velocity (U_{Mean}) and the velocity amplitude (U_{Amp}) are 0.2 m s^{-1} and 0.1 m s^{-1}, respectively. The bubble frequency based on the average two-phase velocity is 0.025 s^{-1} and the angular frequency is 0.157 rad s^{-1} .The simulations have been performed for four different angular frequencies 1, 10, 50 and 100 rad s^{-1}.

TH-2207_146107023

Table 8.1: Properties of the working fluids (Leung *et al.*, 2014)

Properties	**Air**	**Water**
Density (kg m^{-3})	1.185	997.0
Dynamic Viscosity (kg m^{-1} s^{-1})	1.83×10^{-5}	89.0×10^{-5}
Thermal Conductivity (W m^{-1} K^{-1})	0.02	0.60
Specific Heat Capacity (J kg^{-1} K^{-1})	1006.4	4182.0
Surface Tension (N m^{-1})	0.072	

8.3.1 Hydrodynamics

Figure 8.1 shows the variation of the mean two-phase velocity specified at the inlet and the bubble velocity obtained from CFD simulations with time for the four different frequencies. During a cycle, the two-phase velocity changes continuously with time and the rate of change of two-phase velocity also varies. The bubble velocity is also observed to vary sinusoidally in phase with the two-phase velocity having the same frequency as that of the mean two-phase velocity for all the four cases. The magnitude of bubble velocity is higher than the two-phase velocity at all times. However, the ratio between the bubble and two-phase velocity is not same and varies with time. In Fig. 8.2, the variation of the ratio of the bubble and two-phase velocity has been plotted for the case having angular frequency of 10 rad s^{-1}. The ratio is not a constant and varies between 1.05 and 1.10. In a cycle, two maxima and two minima are observed. The two maxima correspond to the cases when the bubble and two-phase velocities are maximum and the two minima probably occur when the liquid velocity is equal to the average two-phase velocity.

TH-2207_146107023

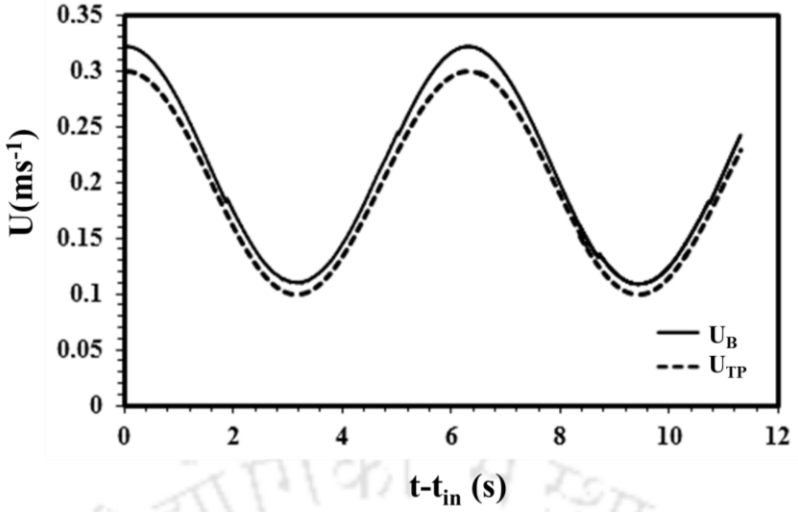

(a)

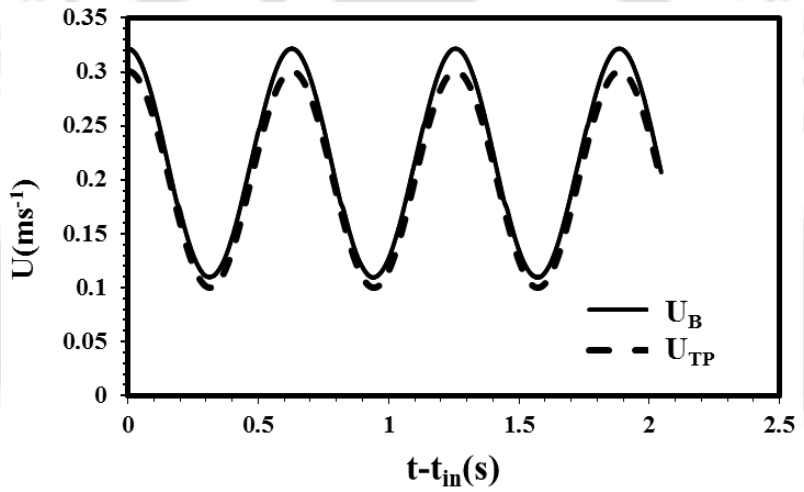

(b)

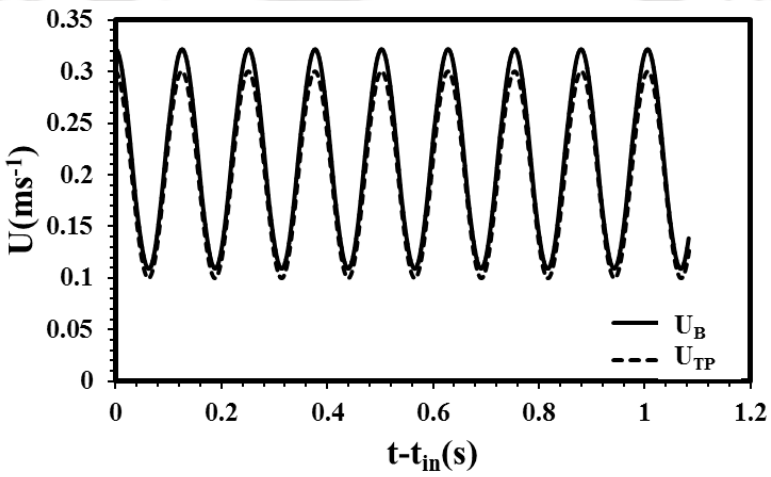

(c)

TH-2207_146107023

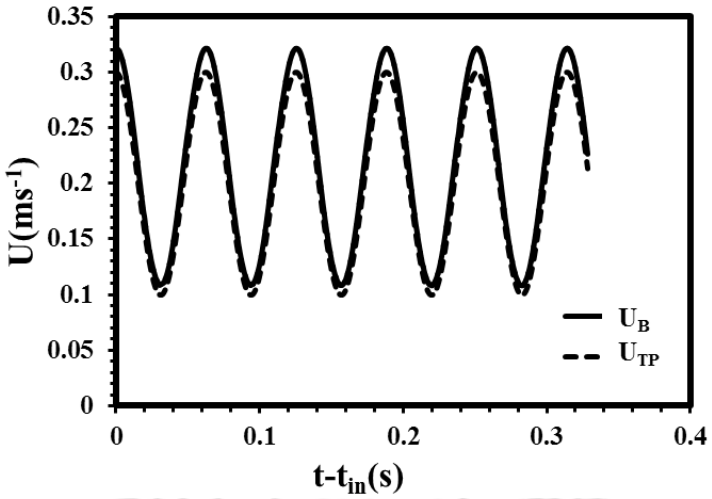

(d)

Figure 8.1: Variation of two-phase velocity (U_{TP}) and bubble velocity (U_B) with time for angular frequencies of (a) 1 rad s^{-1} (b) 10 rad s^{-1} (c) 50 rad s^{-1} and (d) 100 rad s^{-1}.

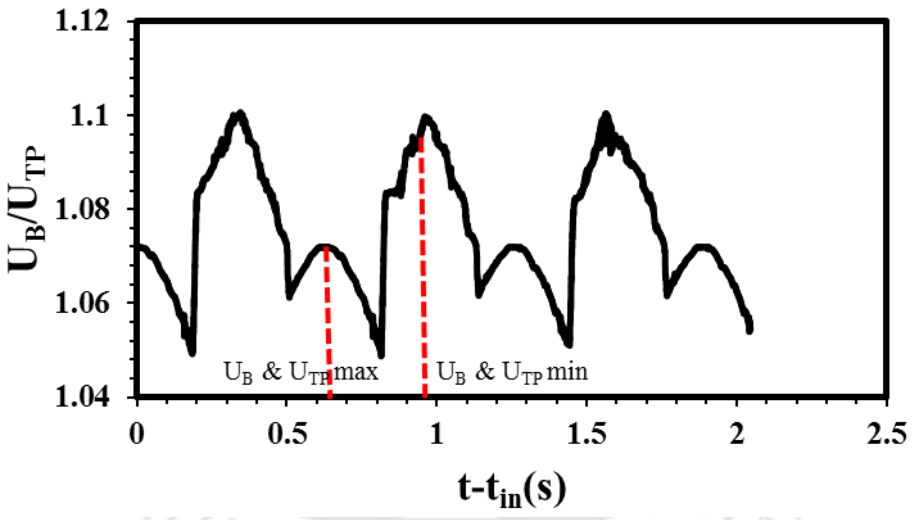

Figure 8.2: Variation of the ratio of bubble velocity (U_B) and two-phase velocity (U_{TP}) with time for angular frequencies of (a) 10 rad s^{-1}.

In Fig 8.3, the bubble shapes at different time instants in a cycle has been shown for the frequency of 10 rad s^{-1}. Figure 8.3(a) shows the time instants marked by solid symbols at which bubble shapes have been plotted. As shown in Fig. 8.3(b), almost no significant change in the bubble shape with time is observed. In Fig. 8(c), the interface shape in the film region has been

TH-2207_146107023

shown. Unlike the steady case, a constant film thickness region in the middle is not observed at all times during a cycle. The minimum film thickness near the back of the bubble is observed to vary between 0.022*R*-0.027*R*. The thickness of the film in the middle region varies between 0.028*R*-0.047*R* in a cycle.

Figure 8.4 shows the velocity profiles in the middle of the liquid slug i.e. at the domain exit at different time instants for the frequencies of 10 and 100 rad s^{-1}. While the velocity profile is close to parabolic for the frequency of 10 rad s^{-1}, large fluctuations in the velocity profile can be seen for the frequency of 100 rad s^{-1}. This observation is similar to that for laminar, liquid-only, fully-developed pulsatile flow in a channel. The velocity profile for the pulsatile flow for liquid-only, fully-developed flow can be derived analytically and is known as Womersley solution

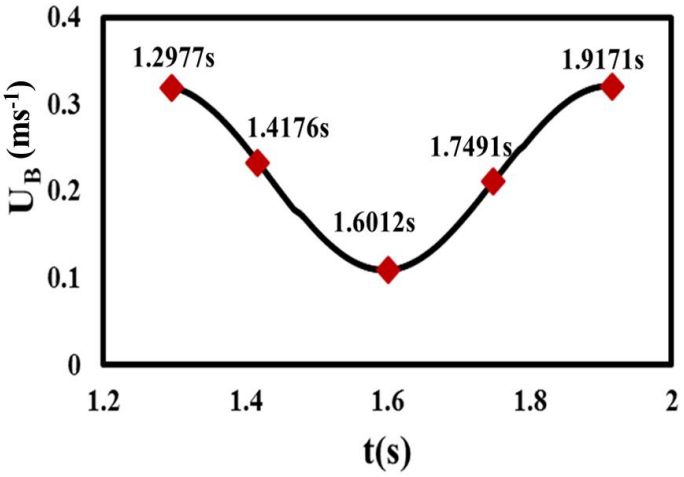

(a)

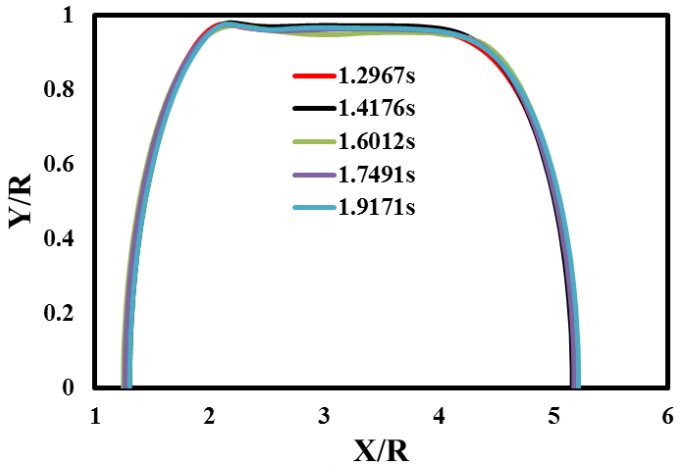

(b)

TH-2207_146107023

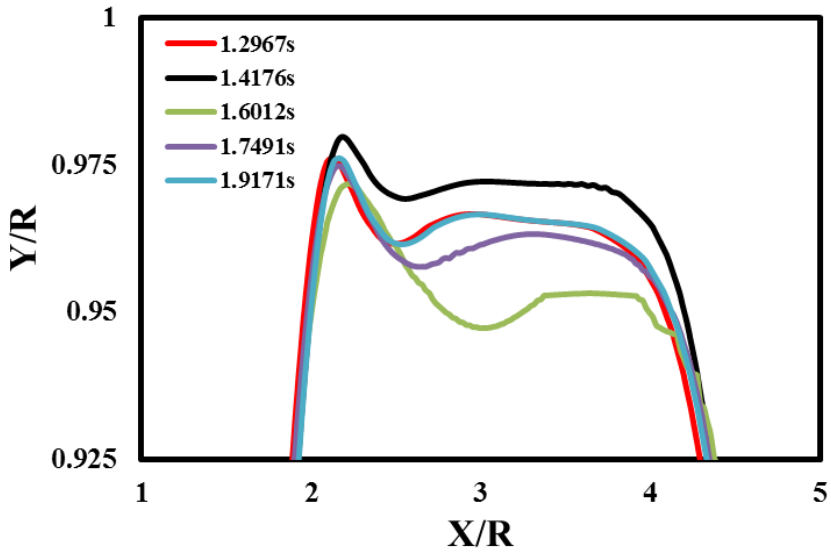

(c)

Figure 8.3: Bubble shape in a cycle at different time and different locations for the angular frequency 10 rad s^{-1} of a Taylor bubble (R_{eqv} = 1.31).

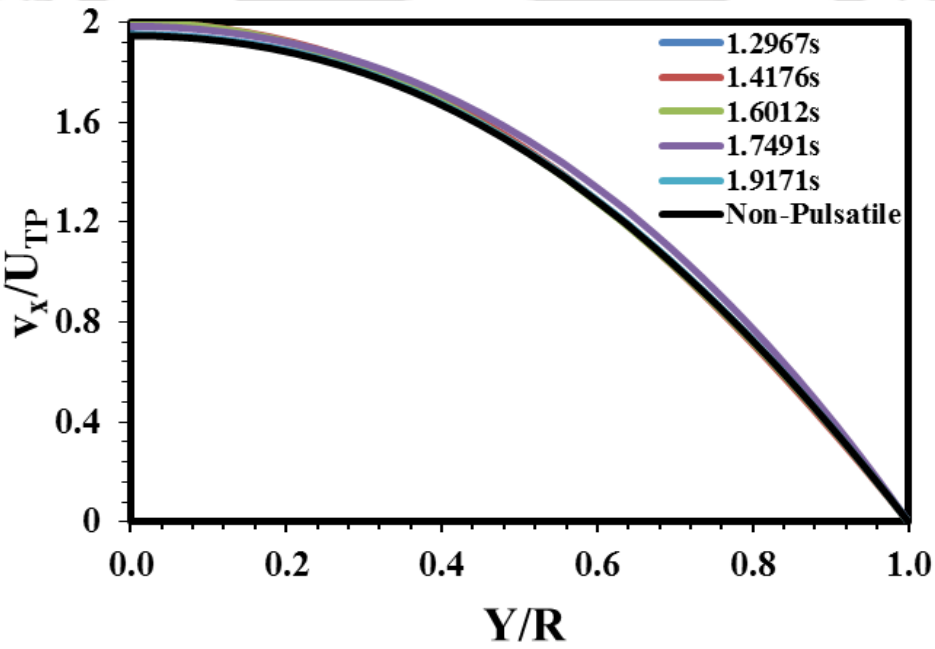

(a)

TH-2207_146107023

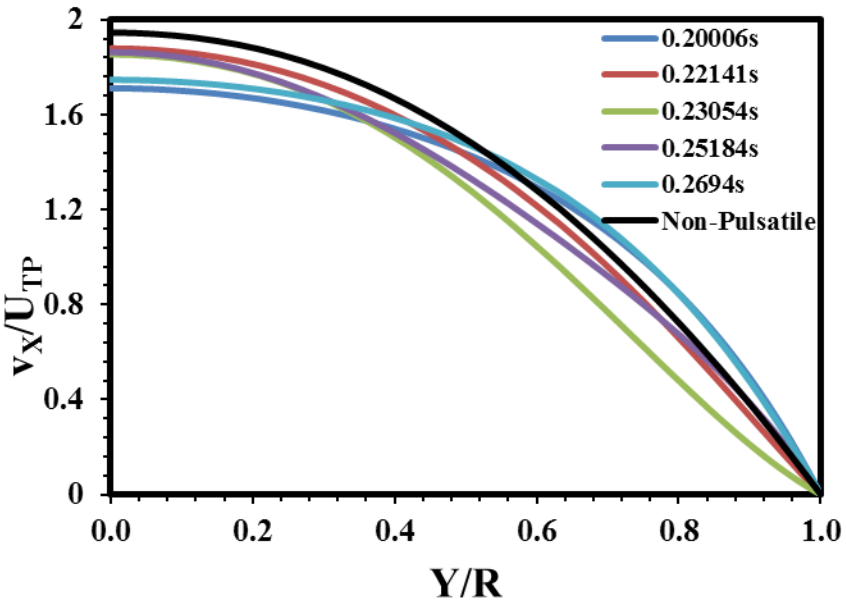

(b)

Figure 8.4: Velocity profile in the middle of liquid slug i.e. at the exit of the computational domain for the angular frequency of (a) 10 rad s^{-1} (b) 100 rad s^{-1}.

The solution suggests the velocity profile to be parabolic at low Womersley number (*Wo*), defined by Eq. (8.2), and a flatter profile at a higher value of Womersley number (Mazumdar, 1992).

$$Wo = \sqrt{\frac{\rho \omega R^2}{\mu}} \tag{8.2}$$

Womersley numbers for the 10 and 100 rad s^{-1} cases are 1.67 and 5.29, respectively.

Figure 8.5(a) shows the variation of the wall shear stress with time for the case having frequency 10 rad s^{-1}. The wall shear stress is observed to vary periodically with the same frequency as that of the flow. Wall shear stress varies from 1.5 Pa to 4.5 Pa. Average wall shear stress for a cycle for the frequency 10 rad s^{-1} is 2.88 Pa. The wall shear stress calculated from Hagen-Poiseuille relation for liquid-only flow having average velocity equal to the mean velocity over a cycle (0.2 m s^{-1}) is only 1.42 Pa and for the maximum velocity over the cycle (0.3 m s^{-1}) is 2.14 Pa. Thus, the wall shear stress is observed to increase significantly due to the

TH-2207_146107023

pulsatile flow. Figure 8.5(b) shows the variation of wall shear stress with the frequency and the average wall shear stress over a cycle is independent of the cycle frequency.

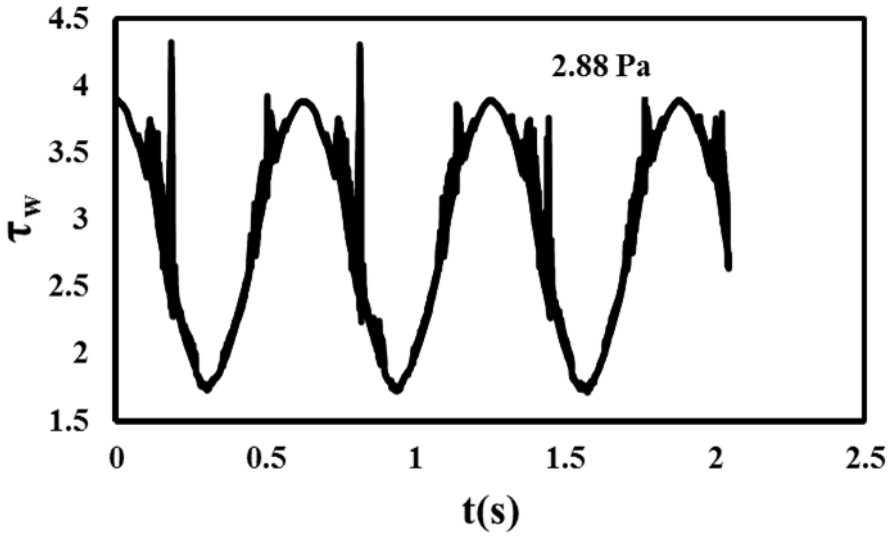

Figure 8.5(a): Wall shear stress variation with the time for the frequency 10 rad s^{-1} of a Taylor bubble (R_{eqv} = 1.31).

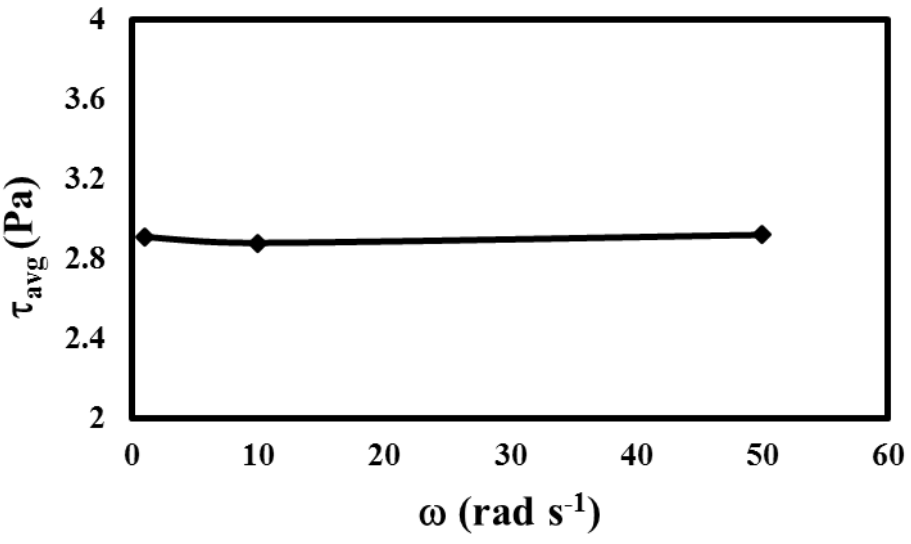

Figure 8.5(b): Average wall shear stress for a cycle with the angular frequency 1, 10, 50 rad s^{-1} of a Taylor bubble (R_{eqv} = 1.31).

TH-2207_146107023

Figure 8.6(a) shows the variation of pressure drop with time for the case having frequency 10 rad s^{-1}. The pressure drop also varies almost periodically with the same frequency as that of the flow between 20 and 60 Pa. Average pressure drop over a cycle for the frequency of 10 rad s^{-1} is 40.3 Pa. As with the wall shear stress, the average pressure drop over a cycle is also independent of the frequency as shown in Fig 8.6(a).

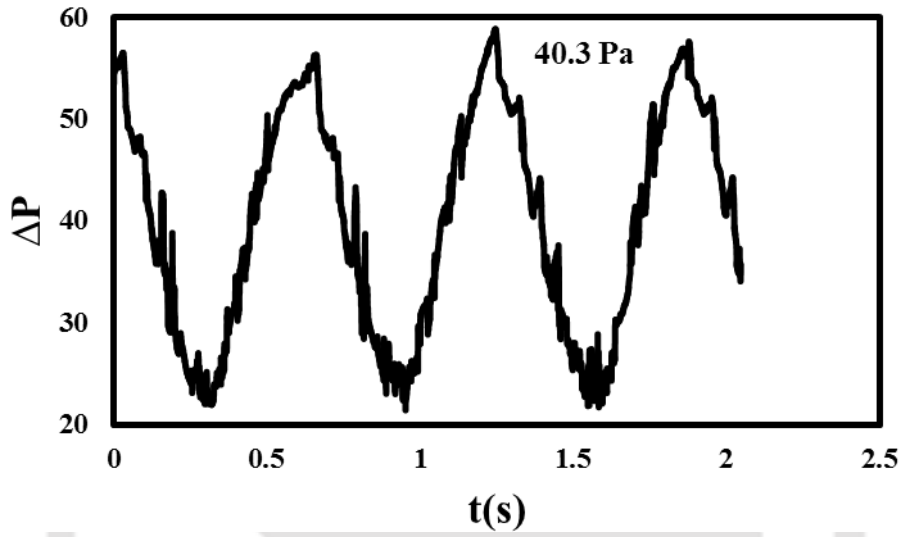

Figure 8.6(a): Pressure drop variation with the time for the frequency 10 rad s^{-1} of a Taylor bubble (R_{eqv} = 1.31).

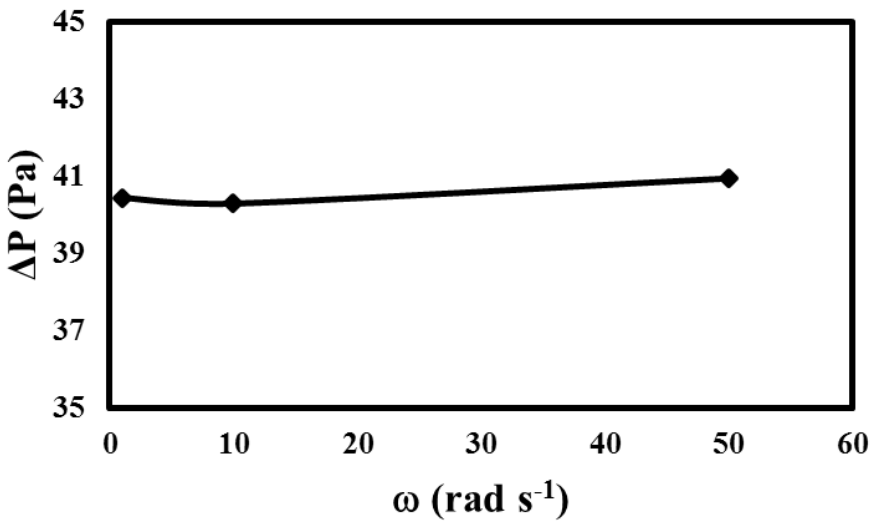

Figure 8.6(b): Average ressure drop for a cycle with the angular frequency 1, 10, 50 rad s^{-1} of a Taylor bubble (R_{eqv} = 1.31).

TH-2207_146107023

8.3.2 Heat transfer

In Fig. 8.7, the variation of Nusselt number with time has been plotted for the four frequencies. At the highest frequency of 100 rad s^{-1}, the Nusselt number varies sinusoidally in a cycle with the minimum and maximum values at the same instances at which the minimum and maximum values of the two-phase velocity occur. At a frequency of 50 rad s^{-1}, the Nusselt number varies periodically with the same frequency as that of the imposed flow but the variation is not sinusoidal. At the lower frequency of 10 rad s^{-1}, the Nusselt number is observed to have two peaks during a cycle. For comparison, a case was run for steady flow with the same velocity boundary condition as for the pulsatile flow i.e. parabolic velocity profile at the inlet.

The variation of Nusselt number with time has been plotted in Fig. 8.8. The Nusselt number for the steady case is 9.86 and increases to 10.8 when the flow is pulsatile and has a frequency of 1 rad s^{-1}. An increase in the flow frequency to 10 rad s^{-1} does not cause much change in the value of Nusselt number and its value is 10.23. When the frequency is increased to 50 rad s^{-1}, the average Nusselt number decreases to 9.23 and further increase in frequency to 100 rad s^{-1} causes the Nusselt number to decrease to 8.5. Pattamatta *et al.* (2015) investigated the heat transfer in oscillatory gas-liquid Taylor flow in a capillary tube of 1.2 mm diameter numerically in a laboratory frame of reference. However, they considered the near wall film temperature instead of bulk fluid temperature in their definition of Nusselt number. This makes the two definitions of Nusselt numbers very different as considering the near wall temperature in the film may not take into account of the fact if the gas bubble or the liquid slug passes under the film. It is therefore not possible to make a direct comparison of this work with theirs. However, interestingly they also observed non-monotonic behaviour in the variation of Nusselt number with frequency. The Nusselt number decreased with an increase in the frequency for frequencies below 5 rad s^{-1} and increased with frequency for higher values.

TH-2207_146107023

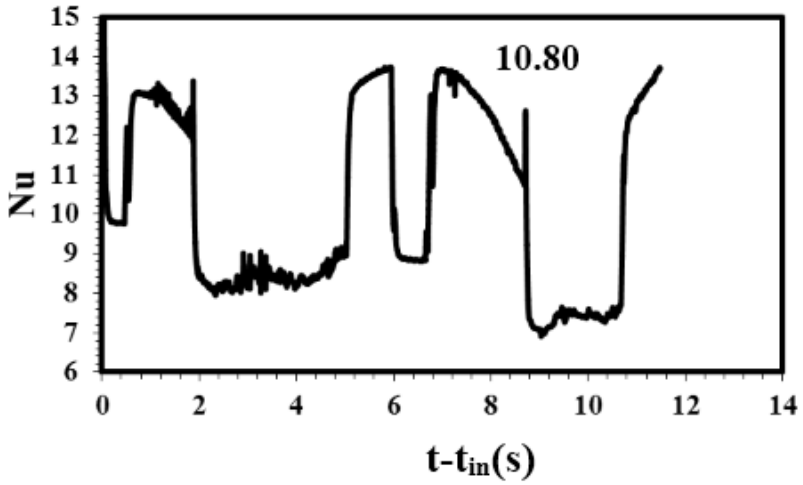

(a)

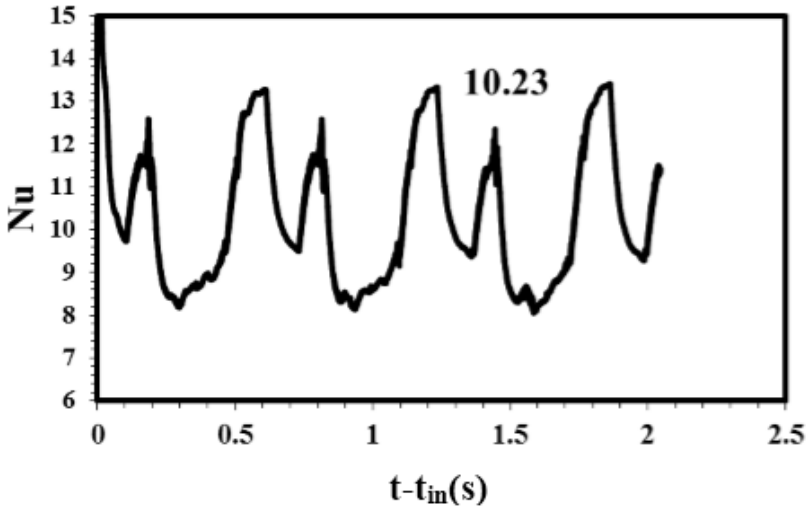

(b)

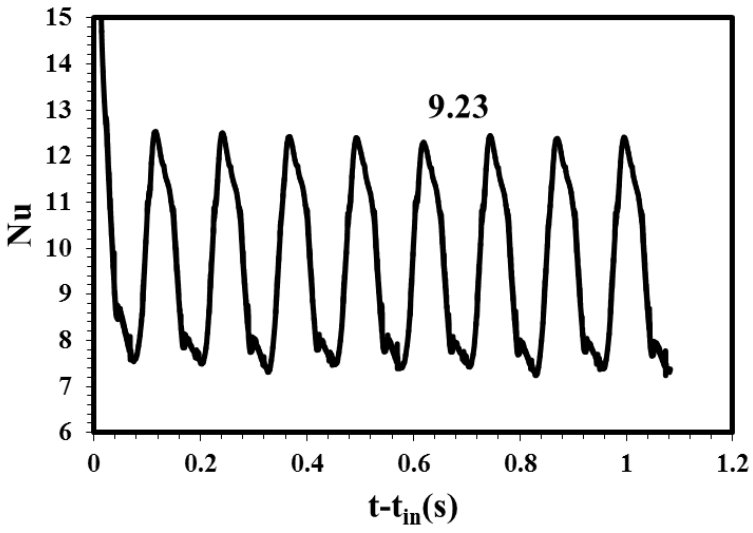

(c)

TH-2207_146107023

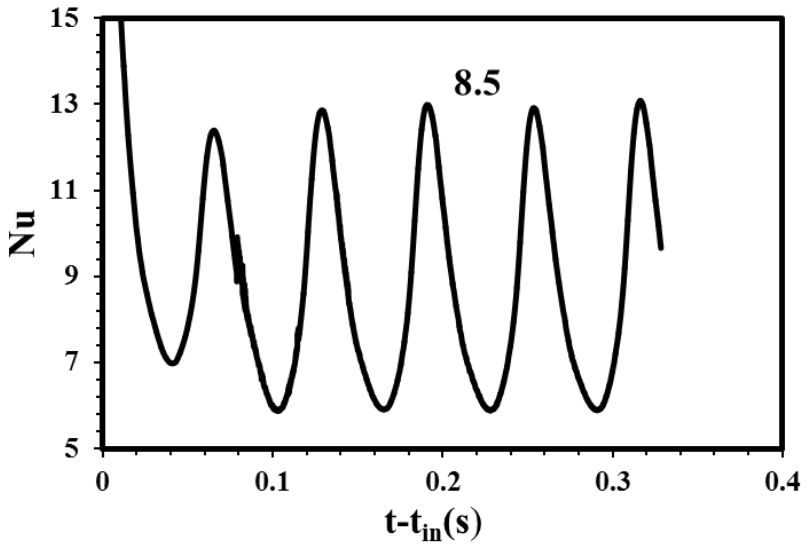

(d)

Figure 8.7: Nusselt number with the time for the angular frequency (a) 1 rad s^{-1} (b) 10 rad s^{-1} (c)50 rad s^{-1} (d) 100 rad s^{-1} of a Taylor bubble (R_{eqv} = 1.31).

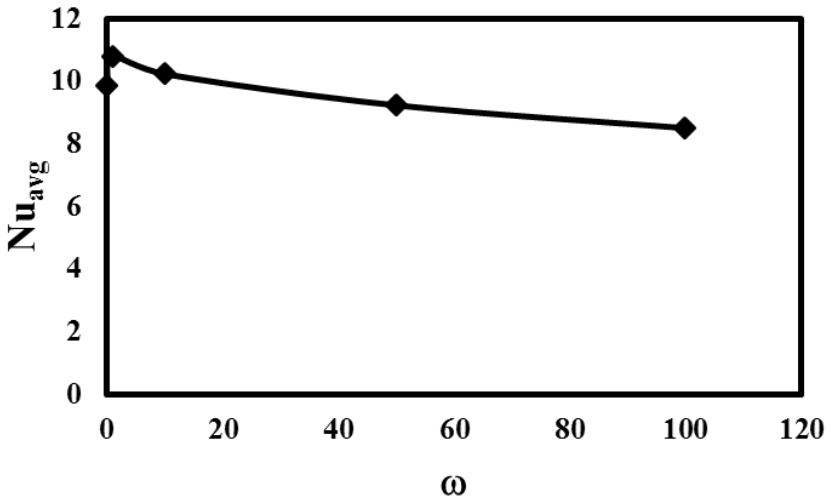

Figure 8.8: Variation of the Nusselt number averaged over a cycle with the angular frequency.

8.4 Conclusions

CFD simulations has been performed for flow and heat transfer in a unit cell with the two-phase velocity varying sinusoidally for four different frequencies 1, 10, 50 and 100 rad s^{-1}. The

TH-2207_146107023

bubble velocity has been observed to vary sinusoidally in phase with the two-phase velocity. However, the ratio between the bubble and two-phase velocity is not constant and varies periodically during a cycle. The wall shear stress as well as the pressure drop also vary with the same frequency as that of the flow and for a cycle the value of wall shear stress and pressure drop are same for all the frequencies. Different patterns of the variation in Nusselt number with time are observed depending on the cycle frequency. The average Nusselt number over a cycle increase with frequency at low frequency but decreases at higher frequencies.

TH-2207_146107023

Chapter 9

Conclusion and Scope of Future work

TH-2207_146107023

CHAPTER 9

Conclusions and Future Scope of Work

In this chapter, the main conclusions that can be drawn from this thesis are summarised. A list of future works that can be further taken up are also discussed.

9.1 Conclusion

CFD simulations have been performed for gas-liquid flow in a millimeter-size channel using the volume of fluid method to capture the interface between the two phases. The main conclusions of the work can be summarized as below:

- A computational methodology has been implemented to model the flow and heat transfer without phase change in a periodic unit cell consisting of a gas bubble and two halves of liquid slug in a frame of reference moving with the bubble. The bubble shape, velocity and shear stress on the wall are compared with the data available in the literature and found to be in good agreement. The Nusselt number obtained from CFD simulations was compared with an extensively validated phenomenological model available in the literature and found to be in good agreement.
- For low bubble volumes ($R_{eqv} \leq 1$), the bubbles are observed to have near spherical shape while bigger bubbles ($R_{eqv} \geq 1$) are observed to have the shape of a typical Taylor bubble- having ellipsoidal front, a cylindrical region in the middle and a ellipsoidal back with a small undulation. The bubble velocity decreased with an increase in the bubble volume before it became volume-independent when bubble assumed the shape of a Taylor bubble. The velocity field and pressure distribution for the spherical and Taylor bubbles are observed to have significant differences. The

TH-2207_146107023

introduction of the bubbles caused an increase in the maximum as well as average shear stress on the wall. The average wall shear stress is maximum when the equivalent sphere radius (R_{eqv}) of the bubble is same as that of the channel.

- The Nusselt number over a unit cell has been observed to be maximum for $R_{eqv} \sim 1$ and an increase or decrease in the bubble volume causes the Nusselt number to decrease. For $R_{eqv} < 1$, Nusselt number increases with an increase in Reynolds number whereas for $R_{eqv} > 1$, the Nusselt number is observed to be independent of Reynolds number. The effect of slug length on the heat transfer in Taylor flow has been studied and the Nusselt number is observed to increase with a decrease in the slug length.

- The bubble approach and evolution of the shape of the merged bubble with time during the coalescence of a Taylor and a spherical bubble have been modelled in a computational domain moving with the Taylor bubble. A methodology to track the ends of the bubbles was developed using k-means clustering algorithm to calculate the velocities of the individual bubbles. When the distance between the bubbles reduces to less than one diameter, significant changes in the flow are observed. During the initial stages of neck growth of the merged bubble is in good agreement with the literature for the bubble coalescence in an outer fluid inside a sufficiently large container.
- The bubble dynamics in suddenly expanding and contracting channel has been studied in a laboratory frame of reference. When a Taylor bubble moves from a small diameter channel to the large diameter channel, its velocity decreases. Whereas when a bubble moves from a large diameter channel to smaller diameter channel, its velocity increases. The ratio of the bubble and two-phase velocity remains same in the two cases, except when the bubble is in the zone of the area change. The evolution in the bubble shape has been presented for both the cases.

- The effect of oscillatory flow on the hydrodynamics and heat transfer in Taylor flow has been studied in a domain moving with the bubble. The velocity of the bubble is observed to oscillate with the same frequency as that of the imposed flow. While no appreciable change is observed in the bubble shape, there is significant change in the thickness of the liquid film surrounding the bubble. The average wall shear stress and pressure drop are observed to be independent of the frequency. The Nusselt number is observed to increase at an angular frequency of 1 rad s^{-1} but decreases at higher frequencies.

9.3 Scope for Future Work

While this thesis makes a humble contribution to the knowledge of gas-liquid slug flow in millimeter-size channels, there are several problems that need to be solved to develop a comprehensive understanding of the subject. Some of the relevant problems can be:

Flow and Heat Transfer in Taylor Flow: In many circumstances, the bubble shape and associated flow field is not axisymmetric and full three-dimensional flow need to be solved. Some examples are slug flow at high Reynolds numbers and slug flow in curved channels. The computational methodology to model periodic Taylor flow developed in this work should be extended to three-dimensions and the user-subroutines should be modified so that the simulations can be run in parallel.

Coalescence of Bubbles: Since the coalescence of bubbles is often associated with heat transfer for example evaporation or gas-liquid exothermic reactions, the heat transfer in the coalescence process need to be modelled. Further, a multiscale model coupling the simple analytical model representing the film drainage process with CFD need to be developed.

Channel Cross-section: In this thesis, the flow of low volume bubbles, which are spherical in the larger section of the channel has been studied. The shape changes of a larger volume bubble having shape of a Taylor bubble should be investigated. Further, the hydrodynamics as the bubble moves in a gradually expanding/contracting channel should also be studied. An interesting and useful problem can be Taylor flow in a channel having periodic expansion and contraction.

Pulsatile Flow: In this work, the effect of oscillatory flow has been studied only in a unit cell. However, the pulsatile flow of liquid (or gas) can also cause the change in the volumes of the bubbles generated and all the bubbles may not be of the same volume. Therefore, the effect of pulsatile flow on the bubble generation and subsequent flow behavior need to be investigated.

References

- Abdelall, F.F., Hahn, G., Ghiaasiaan, S.M., Abdel-Khalik, S.I., Jeter, S.S., Yoda, M., Sadowski, D.L., "Pressure drop caused by abrupt flow area changes in small channels." Experimental Thermal and Fluid Science 29, 2005. 425–434.
- Abiev, R. S., "Analysis of local pressure gradient inversion and form of bubbles in Taylor flow in microchannels." Chemical Engineering Science, 174, 2017. 403-412.
- Abiev, R. S., "Bubbles velocity, Taylor circulation rate and mass transfer model for slug flow in milli- and microchannels." Chemical Engineering Journal, 227, 2013. 66-79.
- Abiev, R. S., "Effect of contact-angle hysteresis on the pressure drop under slug flow conditions in minichannels and microchannels." Theoretical Foundations of Chemical Engineering, 49, 2015. 414-421.
- Abiev, R. S., "Method for calculating the void fraction and relative length of bubbles under slug flow conditions in capillaries." Theoretical Foundations of Chemical Engineering, 44, 2010. 86-101.
- Abiev, R. S., "Modeling of pressure losses for the slug flow of a gas–liquid mixture in mini and microchannels." Theoretical Foundations of Chemical Engineering, 45, 2011. 156-163.
- Almatroushi, E., & Borhan, A., "Coalescence of bubbles translating through a tube." Annals of the New York Academy of Sciences, 1077, 2006. 508–526.
- Ali, R., Palm, B., Martin-Callizo, C. and Maqbool, M. H., "Study of flow boiling characteristics of a microchannel using high speed visualization." Journal of Heat Transfer, 2013. 135, 081501.

TH-2207_146107023

- ANSYS® Academic Research Fluent, Release 15.0, Help System, Theory Guide, ANSYS Inc. 2015.
- Angeli, P, Gavriilidis, A., "Hydrodynamics of Taylor flow in small channels: a review." Proceedings of the Institution of Mechanical Engineers, Part C: Journal of Mechanical Engineering Science. 2008. 222, 737-751.
- Asadolahi, A. N., Gupta, R., Leung, S.S., Fletcher, D.F., Haynes, B.S., "Validation of a CFD model of Taylor flow hydrodynamics and heat transfer." Chemical Engineering Science, 2012. 69:541-552.
- Asadolahi, A. N., Gupta, R., Fletcher, D.F., Haynes, B.S., "CFD approaches for the simulation of hydrodynamics and heat transfer in Taylor flow." Chemical Engineering Science. 66, 2011. 5575-5584.
- Aussillous, P., Quéré, D., "Quick Deposition of a Fluid on the Wall of a Tube." Physics of Fluids 12, 2000. 2367–2371.
- Babin, V., Shemer, L., Barnea, D., "Local instantaneous heat transfer around a rising single Taylor bubble." International Journal of Heat and Mass Transfer 89, 2015. 884–893.
- Balakrishna, T., Ghosh, S., Das, G., and Das, P.K., "Oil water flow through sudden expansion/contraction: Phase distribution and Pressure drop." International Journal of Multiphase Flow, 36, 2010. 13-24.
- Baldassari, C., Marengo, M., "Flow boiling in microchannels and microgravity", Progress in Energy and Combustion Science, 39, 2012. 1-36.
- Bandara, T., Nguyen, N.-T., Rosengarten, G., "Slug flow heat transfer without phase change in microchannels: A review." Chemical Engineering Science,126, 2015. 283-295.

TH-2207_146107023

- Bao, Z. Y., Fletcher, D. F., Haynes, B. S., "Flow boiling heat transfer of Freon R11 and HCFC123 in narrow passages." International Journal of Heat and Mass Transfer 43, 2000. 3347-3358.
- Bao, Z. Y., Bosnich, M.G., Haynes, B.S., "Estimation of void fraction and pressure drop for two-phase flow in fine passages." Trans IChemE, Part A, Chemical Engineering Research and Design 72, 1994. 625–632.
- Bejan, A., "Convective heat transfer." Fourth edition, John Wiley and Sons, New Jersey. 2013.
- Bird, R. B., Stewart, W. E., Lightfoot, E. N., "Transport Phenomena." Wiley India Pvt. Ltd., 2002.
- Bogojevic, D., Sefiane, K., Duursma, G., Walton, A. J., "Bubble dynamics and flow boiling instabilities in microchannels." International Journal of Heat and Mass Transfer 58, 2013. 663–675.
- Brackbill, J. U., Kothe, D. B., and Zemach, C., " A continuum method for modeling surface tension." Journal of computational physics. 100, 1992. 335-354.
- Bretherton, F. P., "The Motion of long bubbles in tubes." Journal of Fluid Mechanics. 10, 1961. 166–188.
- Cabassud, C., Laborie, S. and Lainé J.M., "How slug flow can enhance the ultrafiltration flux in organic hollow fibres." Journal of Membrane Science, 128, 1997. 93-101.
- Cherukumudi, A., Klaseboer, E., Khan, S.A., and R. Manica, "Prediction of the shape and pressure drop of Taylor bubbles in circular tubes." Microfluid Nanofluid, 19, 2015. 1221-1233.

TH-2207_146107023

- Chen, J. W., and J. E. Hilliard , "Free Energy of a Nonuniform System. I. Interfacial Free Energy." The Journal of Chemical Physics 28, 1958. 258–267.
- Chen, R., Yu, H., Zhu, L., Patil, L., Raveena M., Taehun, L., "Spatial and temporal scaling of unequal microbubble coalescence." AIChE Journal, 63(4), 2017.1441–1450.
- Chen, R. H., Tian, W., Su, G. H., Qiu, S. Z., Yuki, I., Oka, Yoshiaki, O., "Numerical investigation on coalescence of bubble pairs rising in a stagnant liquid.", Chemical Engineering Science, 66, 2011.5055–5063.
- Che, Z., Wong, T.N., Nguyen, N., "Heat transfer enhancement by recirculating flow within liquid plugs in microchannels." International Journal of Heat and Mass Transfer, 55, 2012. 1947–1956.
- Clift, R., Grace, J. R. and Weber, M. E., "Bubbles, Drops and Particles." Academic Press, New York. 1978.
- Dai, Z., Guo, Z., Fletcher, D., Haynes, B., "Taylor flow heat transfer in microchannels-Unification of liquid-liquid and gas-liquid results." Chemical Engineering Science, 138, 2016. 140-152.
- Das, S. P., Nikolayev, V. S., Lefevre, F., Pottier, B., Khandekar, S., Bonjour, J., "Thermally induced two-phase oscillating flow inside a capillary tube." International Journal of Heat and Mass Transfer, 65, 2013. 451-459.
- de Mas, N., Günther, A., Schmidt, M., Jensen, K. F., "Microfabricated multiphase reactors for the selective direct fluorination of aromatics", Industrial & Engineering Chemistry Research, 42, 2003. 698-710.

TH-2207_146107023

- Deng, N.N., Jain, S., Wei, W., Xiao, J. X., Chu, R., Yin, L., "Wetting-induced coalescence of nanoliter drops as microreactors in microfluidics." ACS Applied Materials and Interfaces, 6, 2014.3817–3821.
- de Ryck, A., "The Effect of Weak Inertia on the emptying of a tube." Physics of Fluids 14, 2002. 2102–2108.
- Dessimoz, A. L., Raspail, A. L., Berguerand, P., Kiwi-Minsker, C. L., "Quantitative criteria to define flow patterns in micro-capillaries." Chemical Engineering Journal 160, 2010. 882–890.
- Edvinsson, R. K., Irandoust, S.,"Finite element analysis of Taylor flow." AIChE Journal 42, 1996. 1815–1823.
- Feng, J.Q., "A long gas bubble moving in a tube with flowing liquid." International Journal of Multiphase Flow 35, 2009. 738–746.
- Feng, J.Q., "Steady axisymmetric motion of a small bubble in a tube with flowing liquid." Proceedings of the Royal Society A: Mathematical, Physical and Engineering Sciences, 466, 2010. 549–562.
- Fabre J. "Gas-Liquid Slug Flow. In: Bertola V. (eds) Modelling and Experimentation in Two-Phase Flow." International Centre for Mechanical Sciences (Courses and Lectures), vol 450. 2003. Springer, Vienna.
- Fabre, J. and Liné, A., "Slug flow modelling." International Encyclopaedia of Heat and Mass Transfer." Brooklyn, NY: Innodata Corp., 1996. 1015-1021.
- Fairbrother, F., Stubbs, A. E., "Studies in electro-endosmosis Part VI The "bubble tube" method of measurement." Journal of the Chemical Society. 1935. 527-529.

TH-2207_146107023

- Gaver, D. P., Halpern, D., Jensen, O. E., and Grotberg, J. B., "The steady motion of a semi-infinite bubble through a flexible-walled channel." Journal of Fluid Mechanics. 319(1), 1996. 25– 65.
- Giavedoni, M. D., and F. A. Saita, "The rear meniscus of a long bubble steadily displacing a Newtonian liquid in a capillary tube." Physics of Fluids, 11, 1999. 786-794.
- Günther. A., Jensen K.F., "Multiphase microfluidics: from flow characteristics to chemical and materials synthesis." Lab on a Chip. 2006. 6, 1487-1503.
- Gupta, R., Fletcher, D. F., and Haynes, B. S., "On the CFD modelling of Taylor flow in microchannels." Chemical Engineering Science. 64, 2009. 2941-2950.
- Gupta, R, Haynes, B. S., "CFD modelling of flow and heat transfer in the Taylor flow regime." Chemical Engineering Science. 2010. 65, 2094-2107.
- Gupta, R, Fletcher, D. F., Haynes, B. S., "Taylor Flow in Microchannels: A Review of Experimental and Computational Work." The Journal of Computational Multiphase Flows. 2, 2010. 1-33.
- Haase, S., Murzin, D. Y. and Salmi, T., "Review on hydrodynamics and mass transfer in minichannel wall reactors with gas–liquid Taylor flow." Chemical Engineering Research and Design. 113, 2016. 304-329.
- Hägnefelt, H., "Adiabatic two-phase flow in vertical microchannels: Investigation of gravitational effects in the Taylor flow regime." Department of Chemical Engineering, Lund University, Sweden. Master of Science Thesis 2009.
- Han, Y., Shikazono, N., "Measurement of the liquid film thickness in micro tube slug flow." International Journal of Heat and Fluid Flow 30, 2009. 842–853.

TH-2207_146107023

- Harirchian, T., and Garimella, V. S., "Effects of channel dimension, heat flux, and mass flux on flow boiling regimes in microchannels." International Journal of Multiphase Flow 35, 2009. 349–362.
- Hasan, N., and Zakaria, Z., "Computational approach for a pair of bubble coalescence process." International Journal of Heat and Fluid Flow, 32, 2011.755–761.
- Hassan, I., Vaillancourt, M., Pehlivan K., "Two-phase flow regime transitions in microchannels: a comparative experimental study." Microscale Thermophysical Engineering, 9, 2005. 165–182.
- Heil, M., "Finite Reynolds number effects in the Bretherton problem." Physics of Fluids 13, 2001. 2517–2521
- Hirt, C. W., and Nichols, B. D., "Volume of Fluid (VOF) method for the dynamics of free boundaries." Journal of Computational Physics 39, 1981. 201–225.
- Hung, L.-H., Choi, M. K., Tseng, W-Y., Tan, Y-C., Shea J., K., Lee, A., P., "Alternating droplet generation and controlled dynamic droplet fusion in microfluidic device for CdS nanoparticle synthesis." Lab on a chip, 6, 2006.174–178.
- Irandoust, S., Andersson, B., "Liquid film in Taylor flow through a capillary." Industrial & Engineering Chemistry Research. 28, 1989. 1684-1688.
- Kandlikar, S., Garimella, S., Li, D., Colin, S., King, M. R., "Evolution of microchannel flow passages – thermohydraulic performance and fabrication technology." Heat Transfer Engineering., 24, 2003. 3–17.
- Kandlikar, S., Garimella, D., Li, D., Colin, S., King, M. R., "Heat transfer and fluid flow in minichannels and microchannels." Elsevier, 2006.

TH-2207_146107023

- Karayiannis, T.G., and M.M. Mahmoud, "Flow boiling in microchannels: Fundamentals and applications." Applied Thermal Engineering 115, 2017. 1372–1397.
- Kawahara, A., Mansour, M. H., Sadatomi, M., Law, W.Z., Kurihara, H., Kusumaningsih, H., "Characteristics of gas–liquid two-phase flows through a sudden contraction in rectangular microchannels" Experimental Thermal and Fluid Science 66, 2015. 243–253.
- Khan, S. A., Gunther, A., Schmidt M. A., and Jensen, K.F., "Microfluidic synthesis of colloidal silica." Langmuir 20, 2004. 8604–8611.
- Klaseboer, E., Gupta, R., Manica, R., " An extended bretherton model for long taylor bubbles at moderate capillary numbers." Physics of Fluids 26, 2014. 032107.
- Kolb, W. B., and Cerro, R. L., "Coating the inside of a capillary of square cross-section." Chemical Engineering Science 46, 1991. 2181–2195.
- Kreutzer, M. T., Du, P, Heiszwolf, J. J., Kapteijn, F., Moulijn, J. A., "Mass transfer characteristics of three-phase monolith reactors." Chemical Engineering Science. 2001. 56(21-22):6015-6023.
- Kreutzer, M. T., Kapteijn,F., Moulijn, J. A. and Heiszwolf, J. J., "Multiphase monolith reactors: chemical reaction engineering of segmented flow in microchannels." Chemical Engineering Science 60, 2005. 5895–5916.
- Kumar, V., Vikash, V., Nigam, K. P. D., "Multiphase fluid flow and heat transfer characteristics in microchannels." Chemical Engineering Science, 169, 2017. 34-66.
- Kumar, V., Paraschivoiu, M., Nigam, K. D. P., "Single-phase fluid flow and mixing in microchannels." Chemical Engineering Science, 66, 2011. 1329-1373.
- Kumar, V., Vashisth, S., Hoarau, Y., Nigam, K.D.P., "Slug flow in curved microreactors: hydrodynamic study." Chemical Engineering Science, 62, 2007. 7494-7504.

TH-2207_146107023

- Kurimoto, R., Nakazawa, K., Minagawa, H., Yasuda, T., "Prediction models of void fraction and pressure drop for gas-liquid slug flow in microchannels." Experimental Thermal and Fluid Science, 88, 2017. 124-133.
- Laborie, S., Cabassud, C., "Modeling and measurement of shear stress for a slug flow inside a capillary." AIChE Journal. 51, 2005. 1104-1115.
- Lac, E., and Sherwood, J. D., "Motion of a drop along the centreline of a capillary in a pressure-driven flow." Journal of Fluid Mechanics. 2009. 640, 27-54.
- Leonard, B. P., and Mokhtari. S., "ULTRA-SHARP nonoscillatory convection schemes for high-speed steady multidimensional flow". NASATM1-2568 (ICOMP-90-12). NASA Lewis Research Center. 1990.
- Leung, S.S.Y., Fletcher, F.D., Hayne B.S., "Heat Transfer in Well-Characterised Taylor Flow", Chemical Engineering Science 65, 2010. 6379–6388.
- Leung, S.S.Y., Gupta, R., Fletcher, F.D., Hayne B.S., "Gravitational effect on Taylor flow in horizontal microchannels", Chemical Engineering Science 69, 2012. 553-564.
- Liu, H., Vandu, C. O., and Krishna, R., "Hydrodynamics of Taylor Flow in Vertical Capillaries: Flow Regimes, Bubble Rise Velocity, Liquid Slug Length, and Pressure Drop." Industrial & Engineering Chemistry Research 44, 2005. 4884–4897.
- Liu, Q., Palm, B., "Numerical study of bubbles rising and merging during convective boiling in micro-channels." Applied Thermal Engineering, 99, 2016. 1141–1151.
- Macqueen, J., "Some methods for classification and analysis of multivariate observations". Proceedings of the Fifth Berkeley Symposium on Mathematical Statistics and Probability, 1(233). 1967. 281–297.

TH-2207_146107023

- Magnini, M., Pulvirenti, B., Thome, J. R., "Numerical investigation of the influence of leading and sequential bubbles on slug flow boiling within a microchannel." International Journal of Thermal Sciences, 71, 2013.36–52.
- Marcinichen, J. B., Olivier, J. A., Lamaison, N., Thome, J. R., "Advances in electronics cooling." Heat Transfer Eng. 34, 2013. 434–446.
- Marchessault, R. N., and Mason, S. G., "Flow of entrapped bubbles through a capillary." Industial & Engineering Chemistry research. 1960. 52(1), 79.
- Mazumdar, J. N., "Biofluid Mechanics." World Scientific Inc., 1992.
- Mehendale, S. S., Jacobi, A. M., "Evaporative heat transfer in mesoscale heat exchangers." ASHRAE Trans A conference. 106 (1), 2000. 446-452.
- Mehta, B., Khandekar, S., "Taylor bubble-train flows and heat transfer in the context of Pulsating Heat Pipes." International Journal of Heat and Mass Transfer 79, 2014. 279–290.
- Millman, J.R., Bhatt, K.H., Prevo, B.G., Velev, O.D., "Anisotropic particle synthesis in dielectrophoretically controlled microdroplet reactors" Nat. Mater, 4, 2005. 98.
- Park, H. S., and Punch, J., "Friction factor and heat transfer in multiple microchannels with uniform flow distribution." International Journal of Heat and Mass Transfer 51, 2008. 4535-4543.
- Pattamatta, A., Sielaff, A., Stephan, P., "A numerical study on the hydrodynamic and heat transfer characteristics of oscillating Taylor bubble in a capillary tube." Applied Thermal Engineering 89, 2015. 628-63.
- Paulsen, J. D., Carmigniani, R., Kannan, A., Burton C. J., Nagel, R. S., "Coalescence of bubbles and drops in an outer fluid." Nature Communications, 5, 2014. 3182.

TH-2207_146107023

- Pinto, A .M. F. R., Campos, J. B. L. M. S., "Coalescence of two gas slugs rising in a co-current flowing liquid in vertical tubes". Experiments in Fluids, 53, 1998. 2973–2983.
- Prothero, J., and Burton, A. C., "The Physics of blood flow in capillaries: I. The nature of the motion." Biophysical Journal 1961. 565–579.
- Qu, W., Mudawar, I., "Flow boiling heat transfer in two-phase microchannel heat sinks – II. Annular two-phase flow model". Int. J. Heat Mass Transfer 46, 2003. 2773–2784.
- Raghu, S., "Microfluidics for Aerospace Applications." Chapter 18 in Microfluidics and Nanofluidics Handbook: Fabrication, Implementation and Applications, Edited by S. K. Mitra and S. Chakraborty, CRC Press, 2012.
- Rajesh, V. M., and Buwa, V. V., "Volume-of-Fluid Simulations of Gas-Liquid-Liquid Flows in Minichannels", Chemical Engineering Journal, 345, 2018. 688-705.
- Ratkovich, N., Chan, C.C.V., Berube, P.R. and Nopens, I., "Analysis of shear stress and energy consumption in a tubular airlift membrane system." Water Science & Technology, 64, 2011. 189-198.
- Ratkovich, N., Chan, C.C.V., Berube, P.R. and Nopens, I., "Experimental study and CFD modelling of a two-phase slug flow for an airlift tubular membrane." Chemical Engineering Science, 64, 2009. 3576-3584.
- Ratulowski, J. and Chang H.-C., "Transport of gas bubbles in capillaries." Physics of Fluids, 1989. 1, 1642-1655.
- Rauch, R. D., Batira, J. T., and Yang, N. T. Y., "Spatial adaption procedures on unstructured meshes for accurate unsteady aerodynamic flow computations". Technical Report AIAA-91-1106. AIAA. 1991.

TH-2207_146107023

- Revellin, R., Dupont, V., Ursenbacher, T., Thome, J. R., and Zun, T., "Charecterization of diabatic two-phase flows in microchannels: Flow parameter results for R-134a in a 0.5 mm channel." International Journal of Multiphase Flow 32, 2006. 755–774.
- Rosaguti, N. R., Fletcher, D. F., Haynes, B. S., "A general implementation of the H1 boundary condition in CFD simulations of heat transfer in swept passages", International Journal of Heat and Mass Transfer, 50, 2007. 1833-1842.
- Scammell, A., Kim, J., "Heat transfer and flow characteristics of rising Taylor bubbles." International Journal of Heat and Mass Transfer 89, 2015. 379–389.
- Shintaku, H., Kuwabara, T., Kawano, Takaaki,S., Kanno, I., Kotera, H., "Micro cell encapsulation and its hydrogel-beads production using microfluidic device." Microsystem Technologies, 13, 2007. 951–958.
- Sudhakar, T and Das, A. K., "Interface evolution of a liquid Taylor droplet during passage through a sudden contraction in a rectangular channel." Chemical Engineering Science 192, 2018. 993-1010.
- Suresh, V., and Grotberg, J. B., "The effect of gravity on liquid plug propagation in a two-dimensional channel." Physics of Fluids 17, 2005. 031507–1–031507–15.
- Suo, M., and Griffith, P., "Two-phase flow in capillary tubes." Journal of Basic Engineering. 86, 1964. 576-582.
- Sussman, M., Smereka, P., Osher, S., "A Level Set Approach for Computing Solutions to Incompressible Two-Phase Flow", Journal of Computational Physics, 114, 1994. 146-159.
- Taha, T., Cui, Z.F., "CFD Modelling of slug flow in vertical tubes." Chemical Engineering Science. 61, 2006. 676-687.

TH-2207_146107023

- Taha, T, Cui, Z.F., "Hydrodynamic study of upward slug flow in tubular membranes." Desalination. 145, 2002.179-182.
- Talimi, V., Muzychka, Y. S., Kocabiyik, S., "A review on numerical studies of slug flow hydrodynamics and heat transfer in microtubes and microchannels." International Journal of Multiphase Flow 39, 2012. 88–104.
- Thome, J. R., Bar-Cohen, A., Revellin, R., Zun, I., "Unified mechanistic multiscale mapping of two-phase flow patterns in microchannels", Experimental Thermal and Fluid Science, 44, 2013. 1-22.
- Thulasidas, T.C., Abraham, M.A., Cerro, R.L., "Bubble-Train Flow in Capillaries of Circular and Square Cross-Section", Chemical Engineering Science 50, 1995. 183–199.
- Thulasidas, T. C., Abraham, M. A., Cerro, R.L., "Flow Patterns in Liquid Slugs during Bubble-Train Flow Inside Capillaries", Chemical Engineering Science 52 (17), 1997. 2947-2962.
- Triplett, K. A., Ghiaasiaan, S. M., Abdel-Khalik, S. I., Sadowski, D. L., "Gas–liquid two-phase flow in microchannels Part 1: two-phase flow patterns". International Journal of Multiphase Flow. 25, 1999. 377–394.
- Unverdi, S. O., and G. Tryggvason, "A front-tracking method for viscous, incompressible, multi-fluid flows." Journal of Computational Physics 100, 1992. 25-37.
- vanBaten, J.M., Krishna, R., "CFD simulations of mass transfer from Taylor bubbles rising in circular capillaries." Chemical Engineering Science 59, 2004. 2535–2545.
- Vrij, A., "Possible mechanism for the spontaneous rupture of thin, free liquid films" Discussions Faraday Society, 42, 1966.23–33.

TH-2207_146107023

- Walsh, E. J., Muzychka, Y. S., Walsh, P. A., Egan, V., Punch, J., "Pressure Drop in Two Phase Slug/Bubble Flows in Mini Scale Capillaries." International Journal of Multiphase Flow 35, 2009. 879–884.
- Warnier, M. J. F., Rebrov, E, V., de Croon, M. H. J. M., Hessel, V., Schouten, J. C., "Gas hold-up and liquid film thickness in Taylor flow in rectangular microchannels." Chemical Engineering Journal 135(Supplement 1), 2008. S153–S158.
- Watanabe, M., Sanada, T., "In-Line Motion of a Pair of Bubbles in a Viscous Liquid." JSME International Journal Series B, 49(2), 2006.410–418.
- Wibisono Y, Cornelissen, E.R., Kemperman, A.J.B., Van der Meer W.G.J., Nijmeijer K., "Two-phase flow in membrane processes: A technology with a future", Journal of Membrane Science. 2014. 453:566-602.
- Yuan, H. & Prosperetti, A., "On the in-line motion of two spherical bubbles in a viscous fluid." Journal of Fluid Mechanics, 278, 1994.325–349.
- Zhang, J., D. F. Fletcher, W. Li, "Heat transfer and pressure drop characteristics of gas–liquid Taylor flow in mini ducts of square and rectangular cross-sections." International Journal of Heat and Mass Transfer 103, 2016. 45–56.
- Zhao, T. S., and Q. C. Bi, "Co-current air-water two-phase flow patterns in vertical triangular microchannels." International Journal of Multiphase Flow 27(5), 2001. 765.
- Zheng, Y., H. Fujioka and J. B. Grotberg, "Effects of gravity, inertia and surfactant on steady plug propagation in a two-dimensional channel." Physics of Fluids 19, 2007. 082107–1– 082107–16.

TH-2207_146107023